DEVELOPMENT OF LANTHANIDE-DOPED $CASO_4$ FOR TEMPERATURE SENSING APPLICATIONS & ^{64}CU-DOPED GOLD NANOPARTICLES FOR RADIOSENSITIZATION

By

SOLMAZ BASTANI

Bachelor of Science in Physics
Shahid Beheshti University
Tehran, Iran
2006

Master of Science in Atomic and Molecular Physics
Iran University of Science and Technology
Tehran, Iran
2009

Submitted to the Faculty of the
Graduate College of the
Oklahoma State University
in partial fulfillment of
the requirements for
the Degree of
DOCTOR OF PHILOSOPHY
July 2019

DEVELOPMENT OF LANTHANIDE-DOPED $CaSO_4$ FOR TEMPERATURE SENSING APPLICATIONS & ^{64}Cu-DOPED GOLD NANOPARTICLES FOR RADIOSENSITIZATION

Dissertation Approved:

Dr. David N. McIlroy

Dissertation Adviser

Dr. Stephen McKeever

Dr. Hariprasad Gali

Dr. Tyrrell Conway

Dedicated to
the Soul of My Beloved Brother…

For his unconditional love and unwavering support to my lifelong pursuit of dreams and happiness

Acknowledgements reflect the views of the author and are not endorsed by committee members or Oklahoma State University.

ACKNOWLEDGEMENTS

First and foremost, I would like to express heartfelt gratitude to my Ph.D. advisors, Dr. Yukihara, Dr. Cho and Dr. McIlroy, for the opportunity to carry on fascinating research in their labs and for helping me develop as a scientist. Working for Dr. Yukihara helped me develop critical thinking and problem-solving skills. Working with Dr. Cho helped me be an independent thinker who can see multiple dimensions of a project beyond just science. Dr. McIlroy taught me how to communicate my research clearly and meaningfully as well as pointing me in the right direction. In addition, I must thank Dr. Conway for kindly accepting to be a member of my graduate committee. During my time at Oklahoma State University (OSU), I have had the opportunity to work with an incredible scientist who has been instrumental in my growth as a physicist and a researcher. Tremendous thanks must go to Dr. McKeever who has been a great mentor and taught me how to work in an efficient, organized way and how to make sense of the unexpected experimental result. I am incredibly grateful for the privilege of being able to work with this group of intelligent and hardworking individuals at OSU and learn from them.

I would also like to thank my supervisors and colleagues at the University of Oklahoma Health Sciences Center (OUHSC). My interests have always focused on the junction of physics, chemistry, and biology. Working with them has provided incredible resources and a motivating environment that has allowed me to develop a diverse skill set that ranges from chemical synthesis to animal work. I am incredibly grateful for their instruction and support. I particularly would like to thank Dr. V. Awasthi and Dr. Gali for their support throughout the most difficult step of my Ph.D. This

program would have not been wrapped if I could not gain such a wonderful, unique experience at their lab and for that, I owe them more than I can ever appreciate. I would like to extend a sincere gratitude to Ms. Andria Hedrick and Mr. Hooman Yari who have patiently taught me almost everything I know about cell and animal work and has been invaluable in completing the animal studies done at OUHSC over the last year.

Furthermore, I would like to acknowledge all of the past and present OSU radiation dosimetry lab and medical physics lab members as well as OUHSC nuclear pharmacy lab members. In particular, I would like to thank Dr. Echeverria, Dr. Mdzinarishvili, Dr. Chen, Dr. Gustafson, Dr. Coleman, Dr. Pathuri, and Dr. Nkepang for being a great inspiration, resource, and support. I would like to give special thanks to amazing staff and technicians at OSU physics department, Susan, Alisha, Charles and Beth for being overly kind and providing the answer to many administrative questions at any time. I would especially like to thank the dean and the associate dean of graduate college at OSU; Dr. Tucker and the Dr. Van Delinder, as well as Ms. Regina Henry and Ms. Trisha Iyonsi from OSU international student and scholarship office for making me feel like a member of the cowboy family and standing by me throughout all the difficulties.

I am very grateful to my friends Karleyda, Aras, Nishan, Sara, Carolina, Yasaman, Ali, and Diana. Graduate school would have been a lonely place without this group of smart and amazing friends. Through the ups and downs, they have helped me grow and given me perspective. Their support, encouragement, care, and help have meant more than I can express.

Last but not least, I want to thank my parents for their support and encouragement as I have continued my education thousands of miles away from home. Their love, motivation, and interest

in my research, and their energizing spirit throughout the challenges of the Ph.D. program have been an incredible blessing.

I note that even though all my committee members have assisted me greatly in preparing this dissertation, it is likely errors remain in this work, for which I assume complete responsibility.

Name: SOLMAZ BASTANI

Date of Degree: JULY 2019

Title of Study: DEVELOPMENT OF LANTHANIDE-DOPED $CaSO_4$ FOR TEMPERATURE SENSING APPLICATIONS & ^{64}Cu-DOPED GOLD NANOPARTICLES FOR RADIOSENSITIZATION

Major Field: PHYSICS

Abstract: The objective of this work was to develop two different materials; lanthanide-doped $CaSO_4$ (CSO) and Cu@Au gold nanoparticles (GNPs) for particle temperature sensing and biomedical applications, respectively.

In the first part, we synthesized $CaSO_4$ with different lanthanides and characterized the resultant samples using x-ray diffraction (XRD), radioluminescence (RL), and thermoluminescence (TL). The TL emission was observed in most trivalent states of lanthanides including Ce^{3+}, Pr^{3+}, Sm^{3+}, Gd^{3+}, Tb^{3+}, Dy^{3+} and Tm^{3+}. In case of Eu-doped samples, both Eu^{2+} and Eu^{3+} emissions were observed. In addition, we observed a variety of TL peaks with emission from < 100 °C to ~ 600 °C with different intensities. For temperature sensing applications, we were particularly interested in samples doped with Ce and co-doped with either Pr, Gd or Tb, due to their TL emission in the UV region with higher intensity than the single-doped samples as well as the existence of TL peaks in the high temperature region. The results validates that the appropriate choice of dopants can produce TL peaks distributed over a wide range of temperature with high TL intensity. For temperature sensing applications, materials with TL peaks in specific temperature regions are required, therefore, $CaSO_4$ doped with different lanthanides are good candidates for such a purpose. Moreover, we investigated the feasibility of various methods such as initial rise method and various heating rate method to characterize the kinetics of the TL in CSO, including the determination of the order of kinetics, the activation energy (E) and the frequency factor (s).

In the second part, we developed and characterized Cu@Au GNPs using TEM, TEM/EDS, UV-vis, XPS and ICP. The binding properties of the GNPs were then evaluated in human lung cancer cells. Animal studies were implemented by doping radioactive hybrid GNPs with ^{64}Cu ($t_{1/2}$= 12.7 h). For that purpose, the ^{64}Cu@Au GNPs were injected into animals for studying their biodistribution and pharmacokinetics. Since our hybrid Cu@Au GNPs (in which the shells are gold) have identical outer structures to that of regular GNPs, the existing GNP targeting and nano-carrier methodologies can be employed. This allows an easy transition of the technology into basic science investigation and possible clinical practice.

TABLE OF CONTENTS

Chapter Page

Chapter Page

Chapter Page

LIST OF TABLES

Table Page

LIST OF FIGURES

Figure Page

Figure Page

Figure Page

Figure Page

CHAPTER I

OVERALL INTRODUCTION

This dissertation provides an overview of two major projects, describes the results obtained so far and gives the suggestions for future work. The first part of this dissertation (chapters 2-6) concerns the development of lanthanides-doped calcium sulfate ($CaSO_4$) for temperature sensing applications using the Thermoluminescence (TL) technique. The second part of the dissertation (chapters 7- 11) concerns the development of specific gold nanoparticles (GNPs) for targeting lung cancer cells along with some physical and biological studies on these particles.

Hypotheses

Since the rationale of my Ph.D. research is to improve two types of materials for two different applications, the hypotheses consist of two parts. The two hypotheses are as follows:

- The TL properties of potential materials for temperature sensing can be tuned to this application by modification of the dopants. This hypothesis is tested on CaSO4 doped and/or co-doped with lanthanide ions.
- Cu@Au nanoparticles doped with a positron emitting radionuclide exhibit same physical (light absorption, radiosensitization, etc.) and biological (biodistribution, clearance, toxicity, etc.) properties as that of similar sized traditional GNPs.

Specific Aims

The following aims were made to verify the hypotheses. Aims 1-4 focus on the first hypothesis and Aims 5-7 focus on the second hypothesis.

Aim 1

Vary the amount of sulfuric acid used as the sulfate precursor in calcium sulfate (CSO) structure to investigate what amount results in maximal TL intensity and desirable TL peak temperatures.

Aim 2

Dope CSO with different lanthanides of interest for luminescence. Singly-doped CSO will be synthesized with all lanthanides (except La, Pm, and Lu) and will be characterized using x-ray diffraction, radioluminescence (RL), TL emission spectra, and TL glow curves using both broad-band detection and wavelength-resolved detection. We will focus particularly on samples containing blue and UV emitting centers (e.g. Ce^{3+}, Gd^{3+}, Tm^{3+}) because of the better discrimination between TL emission and blackbody background emission.

Aim 3

Co-doping CSO with lanthanides to investigate the effect of co-dopants to introduce TL peaks at even higher temperatures. CSO will be co-doped with Ce because this leads to UV emission and a TL peak in the high-temperature range (~500 °C), combined other co-dopants (Pr, Gd, Tb, and Tm) to obtain as many TL peaks as possible over a broad range of temperatures.

Aim 4

Co-doping lanthanides with alkali metals to investigate if specific alkali metals could be used to introduce additional trapping centers in CSO and extend the temperature range of applicability of this material. Co-dopants (Li, Na, K) will be investigated.

Aim 5

Developing non-radioactive copper-gold nanoparticles (Cu-GNPs) following by doping their core with positron emitting radionuclide ^{64}Cu. The synthesized GNPs will be characterized using a UV/Vis spectrophotometer, ICP, TEM, etc.

Aim 6

Testing GNPs in vitro (human lung cancer cells) for targeting capability and cytotoxicity. For this Aim, we will target the ^{64}Cu-GNPs to a specific cell line and trace them using a gamma counter.

Aim 7

We will apply the radioactive the ^{64}Cu-GNPs in vivo and determine the pharmacokinetics of the ^{64}Cu-GNPs. As a logical extension of the pharmacokinetic study described above, we will study what organ/organ systems are responsible for clearance of GNPs from the blood.

The remainder of this thesis is divided into 11 chapters. Beginning with part one, chapter 3 presents the background information required to understand the TL mechanism. Chapter 4 presents the methodology used for specific Aims 1-4. Each section of chapter 5 and 6 focuses on one specific objective that is required to complete the improvement of CSO for temperature sensing and discusses the results. Chapter 7 concludes the research of each specific Aims 1-4, and suggests possible future studies. Continuing to part two, chapter 8 introduces some background on Gold Nanoparticles (GNP). Chapter 9 describes the basic methodology and characterization techniques used for GNP studies. Chapter 10 presents the research for Specific Aims 5-7 and discusses the results. Chapter 11 summarizes and concludes the research of each specific Aims 5-7, and suggests possible future studies.

PART ONE

Temperature Sensing

CHAPTER II

INTRODUCTION

The first part of this dissertation focuses on the Thermoluminescence (TL) technique and its application in temperature sensing. The TL technique is broadly used for personnel and environment radiation dosimetry, archaeological and geological dating, and defect investigations of solid samples [1]. This technique has also been recommended for temperature measurements of fire damage in concrete [2], to provide the thermal history of meteorites [3-5], and to investigate firing temperatures in ceramics [6].

Another application of TL is for temperature measurements in the environment of a detonation. When an explosion happens in any environment, we need to know the temperature of the core of explosion in order to assess the effects such temperatures may have on biological organisms. Measuring such high temperature in the event of explosion cannot be done by direct measurements (e.g. thermometer) and new techniques are needed. The lack of particle sensors that can track the temperatures encountered by flowing particles exposed to a detonation event has raised the motivation to investigate the development of particles for temperature measurements [7-12]. The basic idea for TL materials acting as passive temperature sensors is the fact that the temperatures to which the particles are exposed affect the trapped charges at different energy levels to different extents depending on the characteristic trapping parameters, namely the activation energy of the trapping center E and frequency factor s [1]. In principle, therefore, the subsequent TL curve of an irradiated material can be used to discover not just the irradiation dose, but also the thermal history of the sample since irradiation. Therefore, the temperature to which the particles are exposed can be extracted by comparing the TL curves of those particles the experienced a temperature profile

to the TL curve of control particles [13-16]. Required material properties for temperature-sensing applications include high TL intensity, low light sensitivity (bleaching), low dark-storage fading, and multiple TL peaks particularly in the high-temperature range of the TL curves. The research group at OSU has worked for several years on this problem and developed some materials suitable for temperature sensing, including lithium borate ($Li_2B_4O_7$), magnesium borate (MgB_4O_7) and calcium sulfate ($CaSO_4$) [13, 16, 17]. These materials have been tested for temperature measurements in the laboratory and in detonation chambers [16, 18]. Previous work on calcium sulfate (CSO) from our group has shown that this material has multiple stable TL peaks at temperatures between 100 ^oC- 430 ^oC [13]. The peaks show low dark fading and insignificant sensitivity to light. CSO:$Ce_{0.2\%}$,$Tb_{0.2\%}$ has been used for temperature measurements tests with the main TL peak at 325 ^oC which is due to Ce^{3+} emission. Since Ce emission is in the UV range and the blackbody radiation is in the red region, we can minimize the overlap of the blackbody radiation by monitoring the emission from Ce^{3+} hence the two are easily separated. The sensitivity (i.e. TL/dose) of CSO:$Ce_{0.2\%}$,$Tb_{0.2\%}$ has been shown to be twice that of LiF:Mg,Ti (a commercial TL material) and its signal intensity can be increased by increasing the irradiation dose as our dose response data confirmed. The step annealing data for CSO:Ce,Tb indicate that the kinetics order for most of the peaks is close to one [13].

Due to the properties identified above, CSO is a material of interest for further improvement. There exists the possibility of extending its TL peaks toward higher temperature by changing the choice of dopants and their concentrations. A systematic study is needed to be done on the role of co-dopants and the dopant concentration on the TL properties of this material. Furthermore, the lack of a detailed model for the trapping and recombination processes in CSO hinders further material development. By investigating a model that can describe the TL mechanism in CSO, the goal is to be able to engineer the TL properties of CSO.

CHAPTER III

BACKGROUND

Thermoluminescence

Basis description of the TL phenomenon

Thermoluminescence (TL), also known as Thermally Stimulated Luminescence (TSL), is a technique that measures the emission of light as a function of temperature while heating insulators and semiconductors that were previously exposed to ionizing radiation [1]. In a typical TL process, a sample is exposed to (irradiated by) ionizing radiation (e.g., beta rays); then it is gradually heated and the light emission is recorded. The emission is due to the thermally stimulated recombination of electrons and holes trapped in defects in the crystalline lattice, and it results in a so-called "TL glow curve", normally consisting of one or more peaks corresponding to the release of electrons and holes from different defects within the lattice. As an example, the TL glow curve of CSO:Tm and CSO:Dy is shown in Figure 1. What distinguishes blackbody radiation from TL is the fact that blackbody radiation is an emission from an object due to the temperature of that object but the light emission due to TL happens as a result of excitation of the material.

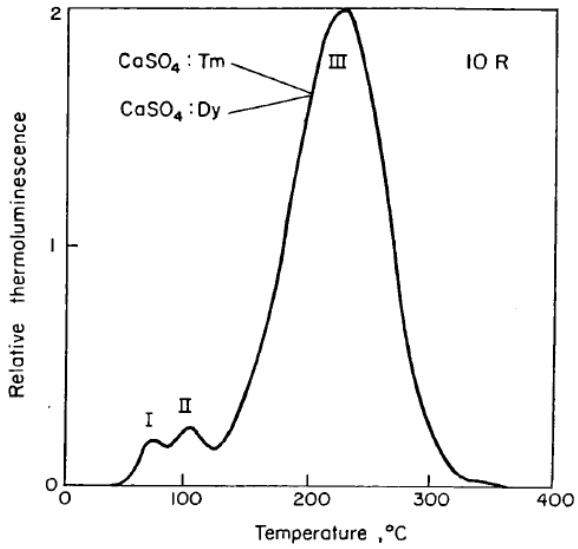

Figure 1. TL glow curve of $CaSO_4$:Tm and $CaSO_4$:Dy [19]

We can use band gap model to explain the TL mechanism. The outer electrons of an atom that are involved in the chemical bonding exist in valence band whereas the conduction band consist of free electrons. In semiconductors and insulators such as materials that we develop for temperature sensing, there exists a gap between these two bands that is empty of electrons. The band gap is the energy needed to exite an electron from the upper state of the valence band to the lowest state of the conduction band ($E_g = E_c - E_v$). The movement of electron from valence band to the conduction band leaves behind a hole in valence band. In a perfect semiconductor, there are no charge carriers in the bandgap and electrons and holes only exist in the delocalized bands (valence and conduction bands) but we can introduce defects into the crystalline lattice to create additional states within the bandgap. These states are called localized bands or levels and behave as either charge traps or recombination centers.

The simplest model for TL studied by Garlick and Wilkins, Garlick and Gibson, and Randall and Wilkins (1945 a, b; 1948) consists of only two localized levels (i.e. a trap and a recombination center) within the energy band as shown in figure 2. When the material is irradiated with the energy

greater than the band gap energy, free electrons and free holes will be produced in the conduction band and in valence bands, respectively (process 1). The charge carriers then have 3 options: (a) recombine with each other; for this to happen, holes need to get trapped in recombination centers (R) (process 5), and then recombine with electrons (process 4). This recombination will result in luminescence if the transition is radiative. (b) Free electrons at first get trapped at trapping centers (T) (process 2) and then gain enough energy (thermal energy in our case) to go back to conducting band (process 3) and from there recombines with holes at recombination centers. The type of luminescence observed depends on the time between the irradiation and recombination as well as the temperature to which the sample is exposed. Recombination with $< 10^{-8}$ - 10^{-3} s after excitations with the minimum effect of temperature is called fluorescence, while phosphorescence occurs by longer timing between excitation and recombination, and are highly affected by temperature. Thermoluminescence is listed under the phosphorescence process.

For the process explained in (b), the probability for an electron being released from the trap per unit time (p) is defined by the Arrhenius equation 3.1 [1].

$$\boldsymbol{p = \tau^{-1} = s * exp(-\frac{E}{kT})} \qquad \textbf{(0.1)}$$

Where τ is the mean time spent in a trap, s is a constant, E is the trap depth, k is Boltzmann's constant and T is the temperature.

According to Randall & Wilkins (1945a, b), if the probability of retrapping is negligible comparing to the probability of recombination, the TL model results in first-order kinetics. On the other hand, if the probability of retrapping is significantly greater than the probability of recombination, the TL peak is said to have second-order kinetics. If the probabilities are somewhere between these two limits, the TL will yield to general-order kinetics as suggested by May and Partridge [20] and discussed by McKeever [1].

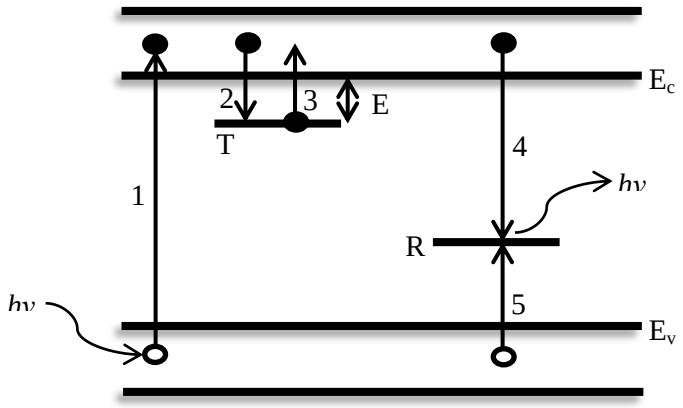

Figure 2. Simple model for Thermoluminescence (after McKeever, 1985) [1]

Order of Kinetics

As mentioned before, all luminescence processes happen due to the change in the population of the charge carriers in the localized bands. For the simple one trap one recombination model explained in the previous section (see Figure 2), a mathematical model can be shaped by knowing the rate equations governing the population of the electrons and holes in the electron trap/ the conduction band and recombination center/ valence band respectively. These rate equations are written as the following [1].

1) The rate of change in the concentration (number per unit volume) of trapped electrons:

$$-dn/dt = np - n_c(N-n)A_n \qquad \textbf{(0.2)}$$

where n is the concentration of trapped electrons, p is the probability for an electron being released from the trap per unit time (see eq. 3.1), n_c is the concentration of electrons in conduction band, N is the concentration of electron traps, and A_n is the probability of electrons trapping at electron traps.

2) The rate of change in the concentration of electrons in conduction band:

$$dn_c/dt = np - n_c(N-n)A_n - mn_cA_r \quad \textbf{(0.3)}$$

where m is the concentration of holes at the recombination center, and A_r is the probability of electrons and holes recombination at a recombination center.

3) The rate of change in the concentration of holes at the recombination center:

$$dm/dt = -m_v(M-m)A_m - mn_cA_r \quad \textbf{(0.4)}$$

where m_v is the concentration of holes in valence band, and M is the concentration of recombination centers and A_m is the probability of holes being trapped at a recombination center.

4) The rate of change in the concentration of holes in valence band:

$$dm_v/dt = m_v(M-m)A_m \quad \textbf{(0.5)}$$

For this simple model, the charge neutrality assumption dictates that the sum of electrons in conduction band and trapped electrons should equal the total concentration of holes in the valence band and trapped holes, i.e. $n_c + n = m_v + m$. An important assumption to simplify the rate equations is called the quasi-equilibrium (QE) condition that means the population of electrons in the conduction band and the rate of change in their population in conduction band is much smaller of that of the trapped ones, that is $n_c \ll n$ as well as $|dn_c/dt| \ll \left|\frac{dn}{dt}\right|$ [21].

With these assumptions, the TL intensity (I) is equal to the rate of reduction in the concentration of the trapped electrons or holes by time.

$$I(t) = -dn/dt \cong -dm/dt \quad \textbf{(0.6)}$$

Combing this equation with the rate equations (3.3, 3.4, 3.5), the TL intensity can be written as the following [22]:

$$I = \frac{nsmA_r * exp(-\frac{E}{kT})}{(N-n)A_n + mA_r} \quad \textbf{(0.7)}$$

Equation 3.6 is General On-Trap (GOT) equation for a TL curve that only consists of one single peak. However, in reality, a material can show multiple TL peaks. Therefore, we need an equation that can show the TL intensity as the function of temperature. By applying some simple assumptions, we can reach to the equations for first- and second- order kinetics.

If we assume that the probability of retrapping is less than the probability of recombination ($(N-n)A_n \ll mA_r$), equation 3.6 will be simplified to

$$\boldsymbol{I = ns * exp(-\frac{E}{kT})} \qquad \textbf{(0.8)}$$

Solving equation 3.7 for n, changing the variable from time to temperature and integrating over temperature (assuming $T(t) = T_0 + \beta t\ ;\ \beta = dT/dt$) generate the TL first-order equation (eq. 3.8) proposed initially by Randall and Wilkins (RW TL equation) [23, 24].

$$\boldsymbol{I(T) = n_0 s * exp\left(-\frac{E}{kT}\right) * exp(-\frac{s}{\beta}\int_{T_0}^{T} exp\ \left(-\frac{E}{kT}\right) dT\ )} \qquad \textbf{(0.9)}$$

On the other hand, if we assume that the probability of retrapping is more than the probability of recombination ($(N-n)A_n \gg mA_r$), equation 3.6 will be simplified to

$$\boldsymbol{I = \frac{nsmA_r * exp(-\frac{E}{kT})}{(N-n)A_n}} \qquad \textbf{(0.10)}$$

This equation was solved similarly by Garlick and Gibson to give an expression for TL second-order peak (GG TL equation).

$$\boldsymbol{I(T) = \frac{n_0^2}{N} s * exp\left(-\frac{E}{kT}\right) * \left[1 + \frac{n_0 s}{\beta N}\int_{T_0}^{T} exp\ \left(-\frac{E}{kT}\right) dT\ \right]^2} \qquad \textbf{(0.11)}$$

If we change the initial population (n_0), the TL first-order peak changes only the height and not the position whereas the TL second-order peak changes in both height and position, with the peak shifting to higher temperature peak as the initial population decreases. Figure 3 shows a computational TL glow peak for both first-order and second-order kinetics. As it can be clearly

seen, in the second-order peak, the peaks become broader and shift to higher temperature as n_0 decreases [1].

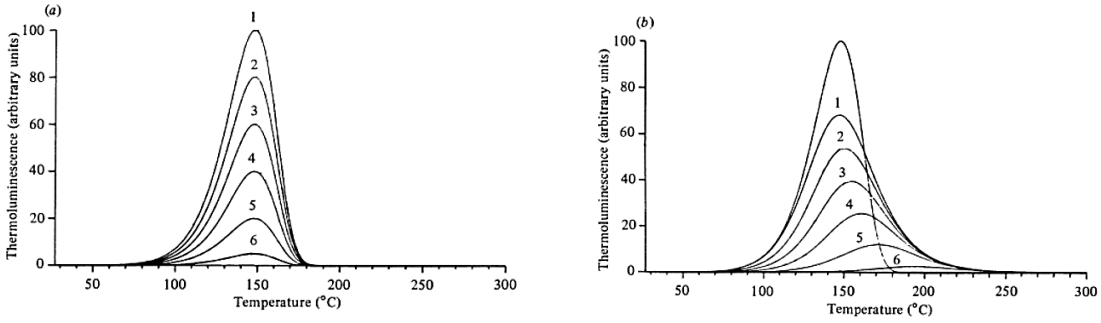

Figure 3. a) first-order TL peak and b) second-order TL peak computed with several initial population, E= 1.0 eV, $s=10^{10}$ s^{-1}, β=10 C/min (after McKeever, 1985)

TL in temperature sensing

Concept

The concept behind the use of TL for temperature sensing is the following [16]: Particles of a TL material are irradiated in the laboratory with a known dose and are then exposed to a thermal event, such as an explosion. Such an event causes a rapid change in temperature. The materials are then recovered and the residual TL is measured. We compare the TL glow curve of the control sample (the sample that is irradiated with the same dose as the TL material but has not been exposed to a thermal event) to that of the recovered experimental samples as shown in Figure 4. The changes in the TL glow curve are due to the temperature to which the sample was heated, and the time for which it was at that temperature. If the time is known or estimated, then the temperature to which the particles were exposed can be inferred.

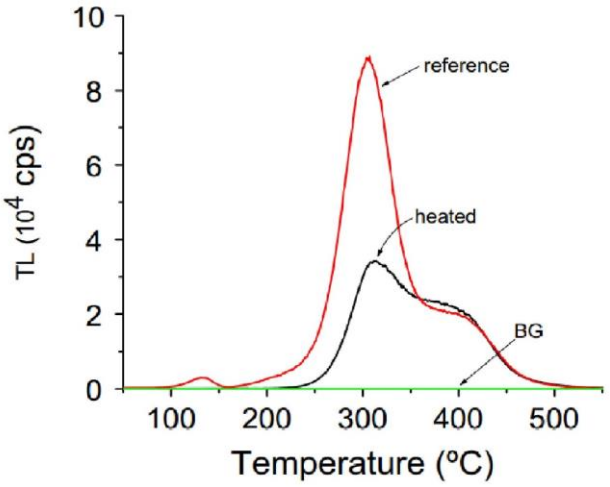

Figure 4. The TL curve for CSO:Ce,Tb heated in a temperature chamber to 380 ºC for 1 s, the sample was prepared with 10 Gy [16]

Material requirements

Based on the concept above, an ideal TL material for temperature sensing applications should have in practice:

a) multiple TL peaks, so that we can measure the information over the wide range of temperature;

b) high sensitivity to radiation, to guarantee that the TL signals are detectable even if only a few grains of material are recovered after the detonation (e.g., 10^6 counts/s for much less than 1 mg of material being irradiated with 500 Gy);

c) high melting point and chemically inert so that the material can survive a high-temperature event such as explosions and harsh environments;

d) low dark fading, to avoid changes in the TL signal until the readout stage in the laboratory; since the information of the temperature event is obtained from the TL curve, we desire a material for which the TL curve is stable to preserve the information;

e) insensitivity of the TL signal to light, because sometimes the materials may be exposed to light during the detonation, preparation and sample recovery;

f) small particle size to mimic the size of biological agents (1-20 microns) and to allow a fast response to temperature in a similar way to the bio-agent [13].

TL materials used for temperature sensing

Early studies and commercial materials

The TL materials that are used for temperature sensing application require different properties than those used for dosimetry applications [13]. For temperature sensing, we are more interested in materials with high sensitivity to ionizing radiation, insensitivity to light, low dark fading, simple TL kinetics and multiple TL peaks that cover the wide range of temperatures, especially toward higher temperatures. For dosimetry applications, tissue equivalency and simple TL curves with single dominant peaks are of more interest.

Overview of materials developed at OSU

Previously, the OSU group has developed several materials for temperature sensing applications, including lithium borate doped with copper and silver ($Li_2B_4O_7$:Cu,Ag), magnesium borate doped with lithium and dysprosium (MgB_4O_7:Li,Dy), and calcium sulfate doped with cerium and terbium ($CaSO_4$:Ce,Tb) [13]. These materials have been synthesized in the laboratory using the solution combustion method and identified to have important characteristics for temperature sensing, such as bright TL emission, low fading, and low bleaching at room temperature. The TL intensity of these materials is comparable to the TL intensity of the commercial TL material, LiF:Mg,Ti, at low doses but with the added advantage of saturating at higher doses (e.g. at 500 Gy, the signal for CSO is still increasing while it is already saturated for LiF:Mg,Ti) [13]. Moreover, the TL for these materials is close to first-order kinetics. These materials have undergone detonation tests at the Naval Surface Warfare Center, Indian Head Division, and the University of Illinois, Urbana-Champaign.

Calcium sulfate as a TL temperature sensors

Early studies and dosimetric properties

$CaSO_4$ (CSO) is a TL material of interest for this project because not only does it fulfill the material requirements but it can extend the temperature range of measurement towards higher temperatures due to the presence of bright, high-temperature TL peaks and UV emission [25].

CSO is used as a host material in different technology areas. Single-phased, undoped CSO is used as a wide-optical-bandgap host for white light phosphors because of its excellent chemical and environmental stability. CSO:Eu is a candidate for photoluminescent liquid crystal displays (PLLCD) and radio-photoluminescence dosimetry, and CSO:Eu,Sm serves as optical storage material [26-28]

The thermoluminescence of CSO, particularly doped with rare earth elements (RE) (e.g., $CaSO_4$:Dy, $CaSO_4$:Tm), has been of interest for dosimetry applications since as early as 1955 [29-32]. They can have sensitivities 30 or 60 times higher than LiF:Mg,Ti ($CaSO_4$:Dy and $CaSO_4$:Tm respectively) [25], are unaffected by heat treatments below 700 °C, and can be economically synthesized in the laboratory [33]. CSO:Dy, CSO:Tm and CSO:Sm are used in environmental radiation measurements and personnel monitoring [19, 32].

CSO has a high melting point (1460 °C) and can be synthesized by several methods, such as the recrystallization technique [19], solid state metathesis [32] and precipitation or acid distillation [28], usually followed by a heat treatment. The synthesis method for commercial CSO used in dosimetry is either single crystal growth or polycrystalline growth as described first by Yamashita et al [19].

Defects and TL properties

TL properties of CSO have been investigated over the years. Several emissions from lanthanide dopants such as Tm^{3+}, Dy^{3+}, Eu^{2+},Eu^{3+}, Ce^{3+} and from metals such as Mn^{2+}, Cd^{2+}, Zn^{2+}, and Pb^{2+}

were reported [29, 34-36]. Also, the main TL glow peaks and the effect of RE impurities on the TL properties of CSO have been studied by Nambi et al. [33]. Over the years, there has been some models proposed to better understand the TL process in CSO:RE (rare earth). Two main models are the following:

a) The 'redox reaction' model proposed originally by Nambi et al. [33] and later supported by Calvert, Danby and Dhopte (1984, 1991a). In this model, the TL process in CSO is described as follows: when $CaSO_4$ is doped with a rare earth (RE), the RE^{3+} ion replaces Ca^{2+} in the lattice. During the irradiation stage, the RE^{3+} ion is reduced to RE^{2+} (electron capture) resulting in a hole trapped in the lattice (for example at SO_3^- or O_3^- radicals). During heating, the hole releases from the lattice, recombines with the trapped electron at RE^{2+} site, and the RE^{2+} ion is oxidized to an excited state of RE^{3+}. The subsequent decay of excited RE^{3+} to its ground state will result in the TL emissions characteristic of the RE^{3+} ion. Figure 5 shows the band diagram for this model.

Irradiation:

$$RE^{3+} + e^- \rightarrow RE^{2+}$$
$$h^+ + SO_3^- (O_3^-) \rightarrow SO_3 (O_3) \qquad \textbf{(0.12)}$$

readout:

$$SO_3 (O_3) \rightarrow SO_3^- (O_3^-) + h^+$$
$$h^+ + RE^{2+} \rightarrow (RE^{3+})^* \rightarrow RE^{3+} + h\nu$$

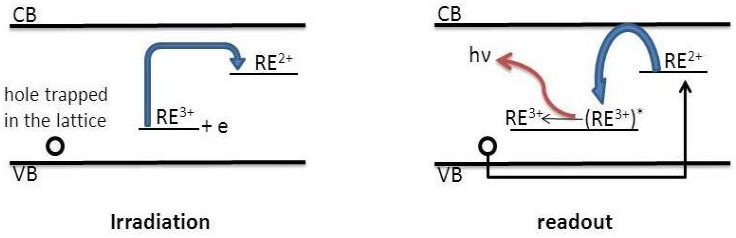

Figure 5. Band diagram depicting Nambi's redox-reaction model for TL process in CSO:RE

The nature of trapping centers and their energy depth highly depend on the RE energy levels relative to the valence and conduction bands [37]. This model fails to explain the emissions from several lanthanides such as Ce^{3+}, since in these lanthanides the RE^{2+} energy levels are very close to or located in the conduction band, so the electrons can easily escape to the conduction band. Some other lanthanides such as Pr, the trap depth is too small, therefore, the trapped electrons are not stable in the room temperature [38].

b) The 'recombination/energy transfer' model proposed by Nambi et al [33] and supported by other researchers [35, 39, 40]: Here, the choice of dopant does not affect the basic trapping and recombination processes. According to this model, during the irradiation stage, electron and hole traps are produced. The hole traps ("radicals" such as SO_3^-, O_3^-) produce stable trapping sites with varying activation energies that results in the multipeak TL glow curves. In undoped CSO, these trapping sites may not be produced with high efficiency or they may recombine shortly after production. During the readout stage, the electrons and holes recombine producing energy. This energy is then transferred to RE dopant resulting in the characteristic emission of RE. Figure 6 depicts the band diagram of energy transfer model.

$$RE^{3+} \xleftrightarrow{irrad} RE^{3+} + h^+ + e^- \qquad \textbf{(0.13)}$$

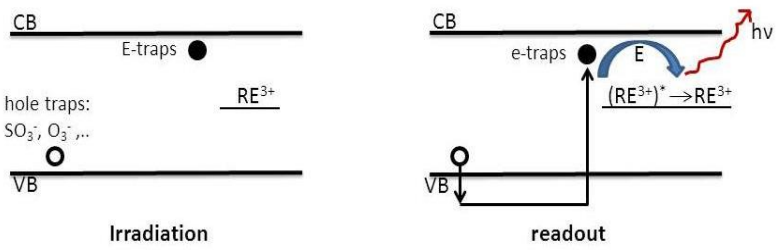

Figure 6. Band diagram depicting Stoebe's energy transfer model for TL process in CSO:RE

According to this model, TL peaks should always occur at the same temperatures since the trapping centers are the intrinsic centers inside the CSO lattice regardless of the choice of dopants. However, this model does not identify the recombination centers. In addition, the details of such an efficient energy transfer that can be applicable within the distance of recombination sites and lanthanide defects are still unknown.

Previous development at OSU

CSO was previously doped with 0.2% of Ce and Tb in the OSU laboratory and the samples were characterized by XRD, SEM and TL techniques. The crystalline structure of CSO was confirmed by XRD and, by using the micrographs from SEM, it was shown that grain size of less than 20-30 μm can be obtained [13]. The main TL peak from CSO:Ce,Tb was reported at 350 ^oC, and the TL emissions at ~ 306 and 324 nm were reported to correspond to Ce^{3+} emission. Other emissions were attributed to Tb^{3+}. The TL kinetics was shown to be close to one.

There is at present very little information on CSO regarding the nature of trapping and recombination centers. There has been no systematic study to show the temperature of occurrence and wavelength of the lanthanide TL emissions simultaneously (TL emission spectra are reported only for a few lanthanides). Also, there has been very little reported on the role of co-doping lanthanides with other lanthanides or other elements (such as alkali metals). The effect of co-doping on the TL properties of CSO has not been yet reported in a systematic way. Also, the effect of

varying the dopant concentrations and energy-transfer phenomenon in CSO has been studied only for few lanthanides.

TL analysis techniques

In order to understand the behavior of TL curves, we need to have insight into the kinetic order of the TL peaks and the characteristic trapping parameters including the trap depth, E, the frequency factor, s, and the densities of traps and recombination centers. Although calculating these parameters does not imply a full understanding of the defect models, it is still the first step to understand the behavior of the TL glow curve during irradiation and heating and choose the appropriate rate equation governing the process in order to develop the suitable TL materials. The real TL materials developed in the lab typically have multiple TL peaks and for the better fitting of a TL glow curve into a set of peaks, linear superposition is assumed. The linear superposition can be used for curve fitting only if the peaks have first-order kinetics [41]. For the higher-order kinetics, however, since the traps are not independent, the curve fitting with superposition assumption is flawed. Therefore, it is important to recognize the order of kinetics for each TL peak of the developed material. The analysis of the TL data is usually divided into two groups, trap emptying (such as initial rise, peak shape, and peak position methods) and trap filling (dose-response) and both parts together can give us a good estimation of the order of kinetics. In this section, multiple methods to determine the kinetic order of the trapping centers are introduced.

Dose Response

The dose-response curve is a property to investigate the behavior of TL curves as the trapping centers are being filled. If the sample is irradiated to different doses, and the TL intensity versus dose is plotted, and if the position of maximum TL peak is not shifted as the traps are being filled, this might be due to the first-order kinetics. To confirm, we need also to look at the order of kinetics of the TL peak as the traps are being emptied.

Initial rise method

The Initial Rise Method (IRM) first introduced by Garlick & Gibson (1948). In this method, the initial part of a TL curve is assumed to be dependent on temperature according to the following equation and that the heating temperature is low enough to keep the trap occupancy (n) approximately constant in the initial part of the curve [1]. If we assume that n is approximately constant in any of the equations 3.8, 3.9, and 3.11 we can write:

$$\boldsymbol{I(t) = C * exp\,(-\frac{E}{kT})} \qquad \textbf{(0.14)}$$

where C is a constant. If we plot ln (I) versus 1/kT over the initial region, the slope of the line will be –E allowing us to determine the activation energy, E. Figure 7 shows the schematic representation of the regions use in IRM.

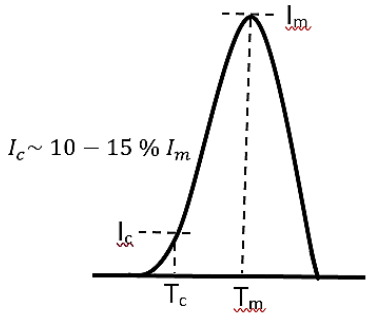

Figure 7. Schematic representation of the initial region in IRM

If we assume that $T \cong T_0$ in the initial rise limit, the integral $\int_{T_0}^{T} \exp\left(-\frac{E}{kT}\right) dT$) becomes zero and RW equation (equation 3.9) will simplify to equation 3.14. If the initial rise rise region behaves like a first-order kinetics and is well isolated, the frequency factor, s, is calculated by equating the derivative of equation 3.9 to zero to find T_m and by algebraic replacements s is calculated as

$$\boldsymbol{s = \frac{\beta E}{kT_m^2}\ exp(\frac{E}{kT_m})} \qquad \textbf{(0.15)}$$

where β is the heating rate (K/s), and K is the Boltzmann constant. The limitation that challenges this method is that n remains approximately constant. This requirement becomes invalid while a temperature exceeds a critical value, T_c. Kivits & Hagebeuk (1977) demonstrated that the corresponding intensity of the initial part of the curve should not exceed the 10-15% of the maximum intensity [42].

Another limitation for this technique is that it can be only applied when the glow peaks are well separated from each other and well defined. To overcome this limitation and to make sure that the TL peak of interest is not made of multiple, overlapping TL peaks, we employ another method called "step annealing" [42].

Step Annealing

This approach is a modified "Thermal Cleaning" method that was attempted before by Nicholas & Woods (1964). The TL curves often consist of multiple overlapping peaks. To ensure the cleaning of the initial rise of the curve from the low-temperature peaks and isolate the region from the high-temperature peaks, the material is preheated to a given temperature T_{stop} after being irradiated and then, the entire TL curve is recorded from room temperature up to the peak temperature, T_m. The pre-heating temperature, T_{stop}, is raised with steps of 2 - 5 ^oC. This method yields to sequential depletion of low TL curves and helps to isolate the initial rise part of the higher TL temperature peaks. The outcome is called aT_m- T_{stop} plot and contains useful information regarding the order of kinetics (see Figure 8). The following figure compares the first and second-order TL peaks in both TL plot and a T_m- T_{stop} plot. The limitation that T_m- T_{stop} plot has is that smaller peaks (low-intensity peaks) can remain hidden by their more prominent neighbors. The accuracy of this method is only 5 ^oC as described by McKeever [42].

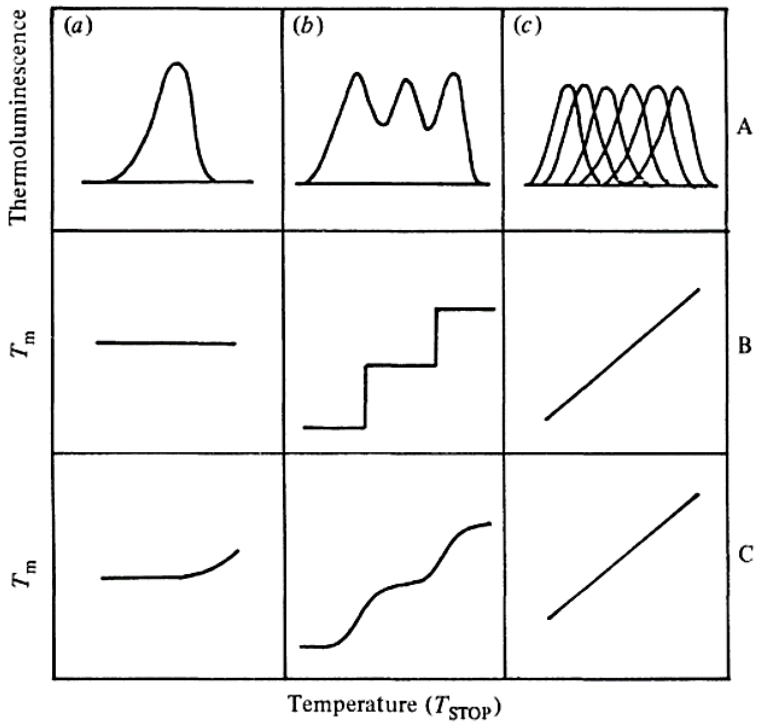

Figure 8. Line A: TL glow curves. Line B: T_m-T_{stop} plot for first-order. Line C: T_m-T_{stop} for second-order. Coloum a: single glow peak. Coloumn b: overlapping peaks. Coloumn C: quasi-continuous distribution of peaks (after McKeever, 1985).

Various heating rate method

The trap depth can also be calculated based on the positions of the maximum of TL peak (T_m). In Various Heating Rate Method (VHRM), E can be calculated from the change in T_m caused by altering the heating rate (β) during TL measurement [42]. During the TL process, heating is generally stays as a linear function, $T(t) = T_0 + \beta t\,;\ \beta = dT/dt$. When the heating rate is increased, and all other parameters are kept the same, the TL peak will be shifted to higher temperatures, the maximum intensity will be decreased, and the width will be increased in order to maitntain a constant total area under the peak as seen in Figure 9.

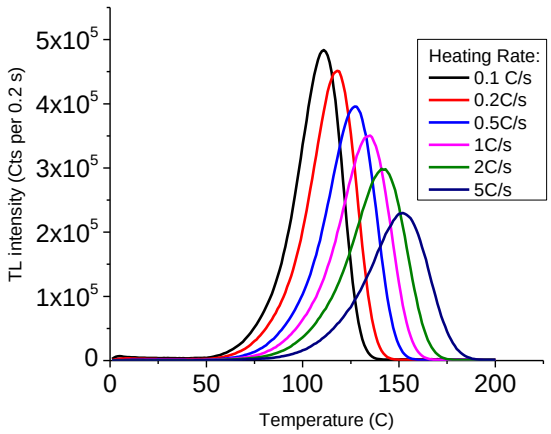

Figure 9. First-order glow curves of CSO:Eu for VHRM

By differentiating the RW equation for first-order peak (eq 3.9) with respect to temperature and equating the derivative to zero at $T=T_m$, the following equation for β can be derived.

$$\beta = (skT_m^2 / E)\exp(-E / kT_m) \qquad \textbf{(0.16)}$$

For the experimental cases, when several heating rates are employed, Hoogenstraaten (1958) suggested noting the value of T_m for each corresponding heating rate and then plotting $\ln(T_m^2 / \beta)$ versus $1/KT_m$. E can be calculated from the slope and s from the y-intercept (Ln(E/sK)) of a linear fit of such a graph. So far, VHRM has been applied to first-order TL peaks but has been shown to be a good approximation for non-first-order kinetic TL processes as suggested by Chen & Winer (1970).

The merit of this method is that the only data needed are T_m and I_m which leads to a fast and simple data collection. However, this method is mostly reliable for the most prominent peaks and can be flawed at higher heating rates. Also, this method fails to determine the activation energy for closely overlapping peaks due to closely grouped trapping centers since it tracks the position of a singular peak and not that of the individual peaks within the distribution.

Objectives of this study

Given the limitations described in previous sections and the lack of ideal TL materials for temperature sensing, particularly in the high temperature range, the objective of this work is to investigate approaches to improve the thermoluminescence (TL) properties of $CaSO_4$ (CSO) for particle temperature sensing applications by controlling the TL properties of CSO and extending its applicability to higher temperatures.

To achieve this, we carried out a systematic investigation of the luminescence properties of CSO doped with lanthanides and investigated the order of kinetics for some of the materials we have developed.

CHAPTER IV

MATERIALS AND METHODS

Synthesis and sample preparation

In this study, instead of crystal growth, the co-precipitation method was used for material preparation. This synthesis method is simple and allows the rapid production of samples doped with different lanthanides in powder form suitable for temperature sensing applications [13].

$CaSO_4$:Ln samples were synthesized by co-precipitation, using the method described by Lakshmanan [34]. $CaCO_3$ and the needed concentration of dopants (see Table 1) were dissolved in deionized water. The solution was stirred at room temperature for 20 min. Sulfuric acid was diluted separately and poured into the $CaCO_3$ solution gradually using a separatory funnel while stirring the solution with a stirring magnet. The solution was then dried on the hot plate at 170 ^oC. Once the solution water was evaporated, the hot plate temperature was raised to 360 ^oC allowing the unreacted sulfuric acid to completely evaporate. The material was annealed in an alumina crucible in a box furnace at 700 ^oC for 2 h. The resultant powder was then crushed and ready for the characterization [38]. The grain size obtained was less than 15 micrometer as will be explained more in the following sections. The samples that were used in this study are summarized in Table 1. All samples were in powder form.

Table 1. Samples used in this study with the order of Lanthanides

Batch Label	Batch Date	Description	Dopant
SB131119-2	Nov. 2013	$CaSO_4:Ce_{0.2\%}$	$Ce(NO_3)_3 \cdot 6H_2O$, REacton®, 99.5%
SB131110-1	Nov. 2013	$CaSO_4:Pr_{0.2\%}$	$Pr(NO_3)_3 \cdot xH_2O$, 99.9%
SB131030-2	Oct. 2013	$CaSO_4:Nd_{0.2\%}$	$Nd(NO_3)_3 \cdot 6H_2O$, 99.9%
SB131106-2	Nov. 2013	$CaSO_4:Sm_{0.2\%}$	$Sm(NO_3)_3 \cdot 6H_2O$, 99.9%
SB131030-1	Oct. 2013	$CaSO_4:Eu_{0.2\%}$	$Eu(NO_3)_3 \cdot 6H_2O$, REacton®, 99.9%
SB131106-1	Nov. 2013	$CaSO_4:Gd_{0.2\%}$	$Gd(NO_3)_3 \cdot xH_2O$, x≈6, REacton®, 99.9%
SB131126-2	Nov. 2013	$CaSO_4:Tb_{0.2\%}$	$Tb(NO_3)_3 \cdot xH_2O$, 99.9%
SB131030-3	Oct. 2013	$CaSO_4:Dy_{0.2\%}$	$Dy(NO_3)_3 \cdot 5H_2O$, 99.9%
SB131107-2	Nov. 2013	$CaSO_4:Ho_{0.2\%}$	$Ho(NO_3)_3 \cdot 5H_2O$, 99.9%
SB131112-1	Nov. 2013	$CaSO_4:Er_{0.2\%}$	$Er(NO_3)_3 \cdot 5H_2O$, 99.9%
SB131126-1	Nov. 2013	$CaSO_4:Tm_{0.2\%}$	$Tm(NO_3)_3 \cdot xH_2O$, x≈5, REacton®, 99.9%
SB13112-2	Nov. 2013	$CaSO_4:Yb_{0.2\%}$	$Yb(NO_3)_3 \cdot 5H_2O$, x≈5 or 6, 99.9%
SB131107-1	Nov. 2013	$CaSO_4$:undoped	
SB131009 SB131016	Oct. 2013	$CaSO_4:Ce_{0.2\%},Tb_{0.2\%}$	
SB140610-8651	June 2014	$CaSO_4:Ce_{0.2\%},Tb_{0.2\%}$<75µm	
SB140703-3	July 2014	$CaSO_4:Ce_{0.2\%},Pr_{0.2\%}$	
SB140703-4	July 2014	$CaSO_4:Ce_{0.2\%},Gd_{0.2\%}$	
SB140703-1	July 2014	$CaSO_4:Ce_{0.2\%},Tm_{0.2\%}$	
SB140703-2	July 2014	$CaSO_4:Ce_{0.2\%},Tb_{0.2\%}, Tm_{0.2\%}$	
SB140525-1	May 2014	$CaSO_4:Li_{0.2\%}$	$LiNO_3$, 99.0%

SB140525-2	May 2014	$CaSO_4:Na_{0.2\%}$	$NaNO_3$, 99.0%
SB140525-3	May 2014	$CaSO_4:K_{0.2\%}$	KNO_3, 99.0%
SB140602-1	June 2014	$CaSO_4:Pr_{0.2\%},Li_{0.2\%}$	
SB140602-2	June 2014	$CaSO_4:Pr_{0.2\%},Na_{0.2\%}$	
SB140602-3	June 2014	$CaSO_4:Pr_{0.2\%},K_{0.2\%}$	

Particle Sieving

To identify the size of the particles dry and wet sieving tests were performed. Since the dry sieving did not pass any measurable amount of material, wet sieving was used as an alternative to get the desired percentage of the particles <13 μm by mass. TL of the material before and after sieving was compared as a way to confirm that the materials' TL properties were not affected after the wet sieving. For the wet sieving, 100 mg of CSO was mixed with 250 mL of ethanol. The mixture was sonicated for 45 minutes followed by 10 minutes of stirring to avoid CSO from aggregating in the ethanol after the initial sonication. Wet sieving passed 95% of the material. We also collected SEM images to verify the size of the particles.

Material characterization

X-ray powder diffraction

We used a powder X-ray diffraction (XRD) to confirm the crystalline structure of the host lattice (CSO). A Bruker Advance D8 diffractometer was used in this study and was equipped with an LYNXEYE detector (D8-25 ADVANCE Bruker AXS GmbH). The equipment operation voltage was 40 kV and the operation current was 40 mA. The diffractograms of the samples were collected by placing the samples in PMMA specimen holders and with CuKα radiation filtered by a 0.02 mm Ni foil. The scanning specifications are 2θ , step size 0.02 degrees, and 0.5 s /step. Crystalline structure and phase recognition of the samples were carried out by matching the x-ray

diffractograms to patterns from the International Centre for Diffraction Data (ICDD) PDF 2 Release 2011 Database version 2.1102, PDF card 00-037-1496.

Scanning electron microscopy

A Quanta 600 field-emission Scanning Electron Microscope (SEM) was used to determine the morphology of the samples. The equipment magnification was around 5000 and the acceleration voltage was 20 kV. The samples were prepared by two methods: wet and dry preparation. In wet preparation, 25 mg of the particles were dispersed in 50 ml of ethanol followed by ultrasonication for 15 min. Then, one drop of the suspension was poured on an aluminum stub, allowed to dry and coated with gold palladium. In dry preparation, a carbon layer was stuck to the top of a sample holder and it became in contact to dry powder so that the carbon layer was coated with only a thin layer of CSO.

Thermoluminescence

TL glow curves were obtained using a Risø TL/OSL-DA-15 reader with a heating rate of 5 ºC/s in nitrogen atmosphere (N_2 flow was present usually for 30 s). Typically 10 mg of material placed in stainless steel cups was used unless mentioned otherwise. The source of radiation was beta particles from $^{90}Sr/^{90}Y$ (dose rate of 0.1 Gy/s). The TL signal was detected using a photomultiplier tube (PMT) together with either U-340 filters (7.5 mm thickness, transmission between 270–380 nm, Hoya Corporation, CA, USA) or Schott BG-39 glass filter (6 mm thickness, transmission between 330-620 nm, Schott AG, Mainz, Germany). To avoid PMT saturation, we used an aperture for higher doses, which will be mentioned when relevant.

Radioluminescence

Radioluminescence (RL) were measured using an optical fiber system (Ocean Optics USB-2000 fiber spectrometer, Ocean Optics, Inc., Dunedin, FL, USA). The Magnum™ X-ray (Moxtek Inc.)

operated at 40 kV with Ag transmission target. The spectra obtained for this study were not corrected for the relative detection efficiency as described by Orante-Barrón, et al. [43].

Photoluminescence

Photoluminescence emission and excitation spectra were obtained using the Fluorolog-3 spectrofluorometer (model FL3-22, Horiba Jobin Yvon Inc.) The instrument uses a Xenon lamp for excitation and a double grating adjustable monochromators for the selection of excitation and emission beams. Light exiting the emission monochromator is collected by a PMT.

Determination of kinetic parameters

Dose-response Curves

A desirable property of a TL material for temperature sensing is a linear relationship between TL intensity and the absorbed dose. Dose-response curves were measured for three samples and three aliquots of each: CSO:Pr, CSO:Tb and CSO:Tm. The amount of materials used was a few grains to avoid the non-uniform distribution of heat to different parts of the cup during the heating stage. Samples were irradiated with β radiation for 1,2,5,10,20,50,100,200,500,1000,2000, and 5000s. The three aliquots of the same material were normalized to dose. We had to use some apertures for bright samples at high doses and the intensities were later corrected for different apertures.

Step-annealing data

Step-annealing is a method to determine the dependence of the curve shape on the different preheat temperatures and to study if there are more complex peak behaviors (non-first-order kinetics) present in our samples. In this method, the material was preheated to a given temperature T_{stop} after being irradiated and then, the entire TL curve was recorded from room temperature up to a maximum readout temperature and the temperature of the first TL maximum (T_m) was recorded.

The pre-heating temperature was raised with steps of 5 ^{o}C. Shift in T_m with T_{stop} can indicate possible non-first-order kinetic for the TL process or the existence of trapping centers closely distributed in energy.

Activation energy by the initial rise method

As explained earlier, IRM technique was employed after step annealing the samples CSO:Tm, CSO:Pr and CSO:Eu to calculate the activation energy. After plotting Ln (I) versus 1/kT, we used three approaches to read the slope of the linear fit trend in the initial part of the graph: in the first approach, we only used our observation to recognize the initial part of the graph looking for the most linear, small section of the graph. This approach is called the "estimate by eye" throughout the dissertation. In the second approach, graphs of Ln (I) vs 1/kT are divided into the temperature zones in which the initial part of the graphs have fixed temperature range. Then, the slope of linear fit in each fixed temperature range is read. We continued the fitting until the graph appears to be non-linear in that temperature zone, then we shifted the fitting to a new temperature zone. This approach is called "const. temp" in the following chapters. In the third approach, linear fitting was employed only to the initial part of the graph in which the temperature does not exceed 10% of the correspondent I_{max}. In chapter 5, the calculated E using different approaches are compared.

Various Heating Rate Method (VHRM)

This method was used for 1 mg CSO:$Eu_{0.2\%}$ using 6 different heating rates (0.1, 0.2, 0.5, 1, 2, and 5 ^{o}C/s) with a 120 s pause after irradiation of (80 Gy) to let the equilibrium of charge carriers. The plot of $\ln(T_m^2/\beta)$ versus $1/kT_m$ was plotted for all heating rates and the activation energy was calculated from the slope of the best linear fit between the data points.

CHAPTER V

BASIC LUMINESCENCE PROPERTIES OF CALCIUM SULFATE

RL of CSO

The RL spectra for $CaSO_4$ doped with different lanthanides are presented in Figure 10. Except from Nd, Ho, Er and Yb-doped samples that did not show significant RL emission, and thus are not presented in this document, all other samples show a clear RL emission.

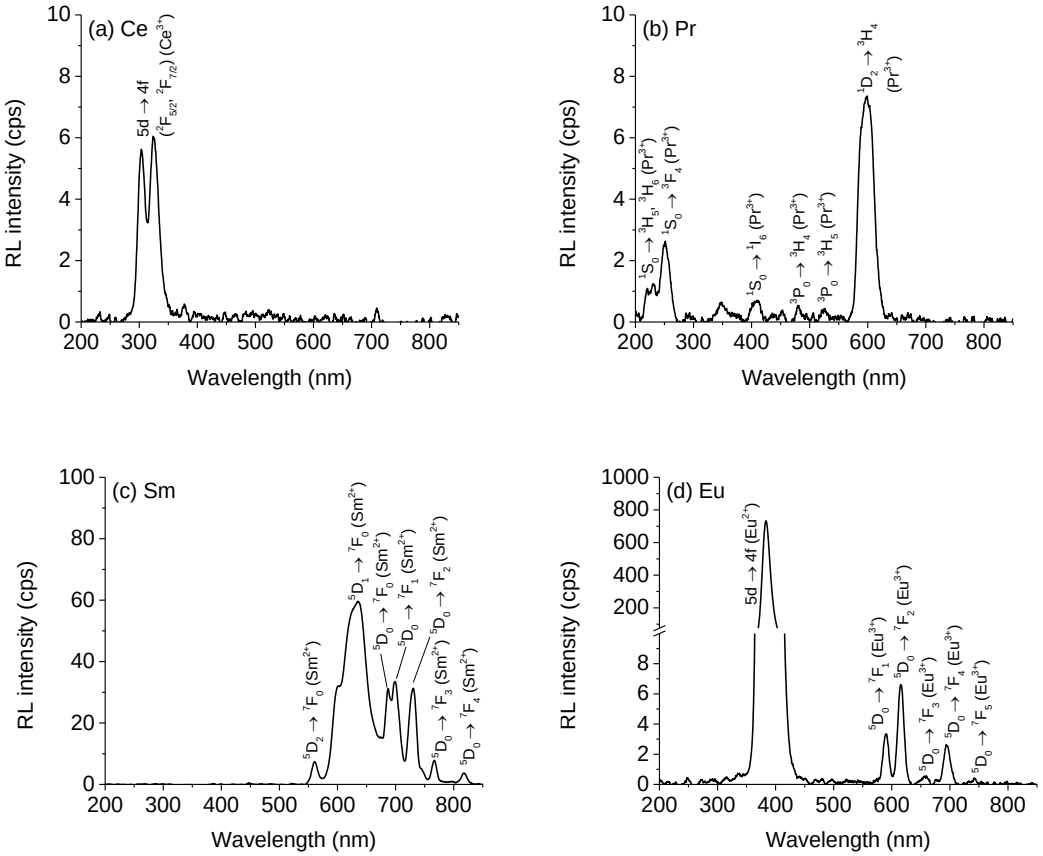

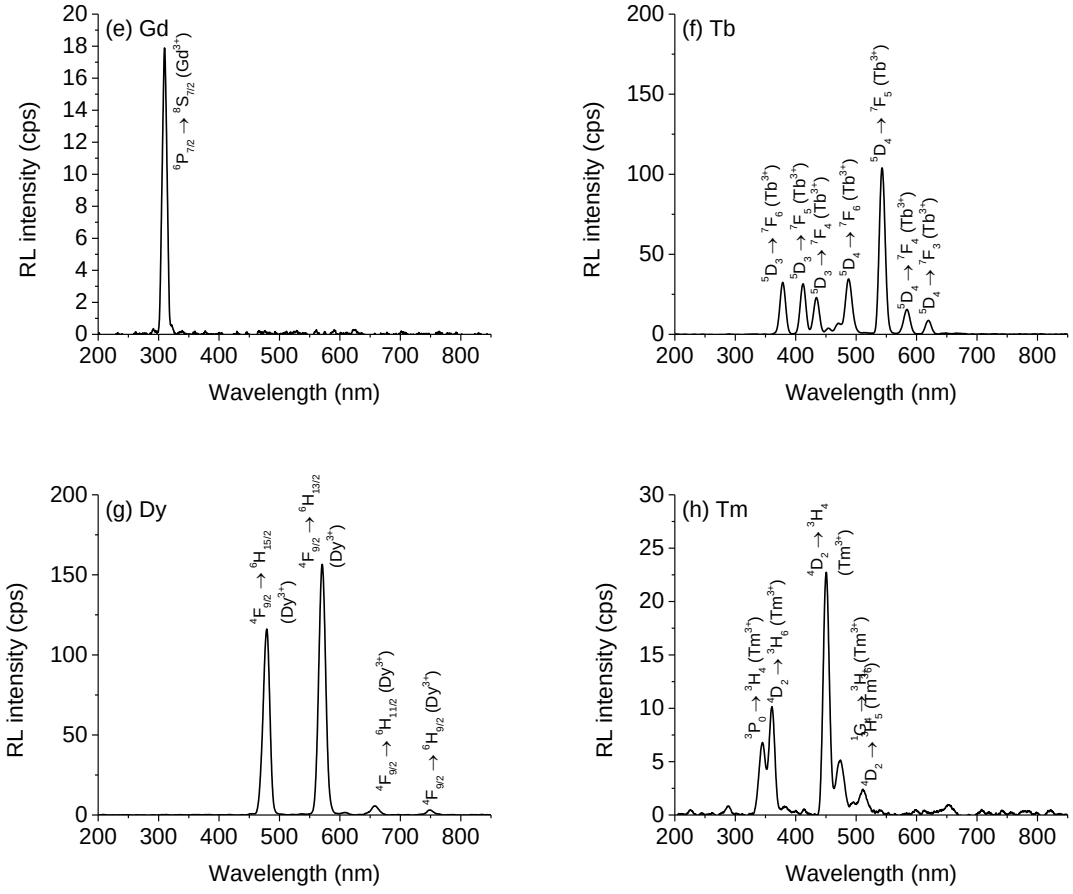

Figure 10. RL spectra of $CaSO_4$ doped with different lanthanides.

As seen in the figure above, the most intense emissions belong to samples doped with Sm, Eu, Tb and Dy. CSO:Ce shows the typical emission bands of Ce^{3+} at ~304 nm and 324 nm associated with $5d \rightarrow (2F_{5/2}, 2F_{7/2})$. For all other lanthanides, the RL emission bands (or lines) are in a various regions of the spectrum (e.g. UV emission for Pr^{3+} and red to infrared emission for Sm^{3+}). These RL emissions are confirmed in the literature and are a good indicator to show that the lanthanides have free f shells [38]. The emission bands (or lines) are normalized to the most intense emission and identified in Table 2.

Table 2. RL emission bands (or lines) identified in $CaSO_4$ doped with different lanthanides. Uncertain assignments are indicated by (?).

Dopants (0.2 mol%)	Emission	Emission (cm^{-1})	Relative RL intensity	Transition
Ce	304 nm	32942 cm^{-1}	0.8 %	5d → 4f ($^2F_{5/2}$; Ce^{3+})
	324 nm	30891 cm^{-1}	0.8 %	5d → 4f ($^2F_{7/2}$; Ce^{3+})
Pr	230 nm	43447 cm^{-1}	0.2 %	$^1S_0 \rightarrow {}^3H_{5,6}$ (Pr^{3+})
	251 nm	39773 cm^{-1}	0.4 %	$^1S_0 \rightarrow {}^3F_4$ (Pr^{3+})
	599 nm	16701 cm^{-1}	1.0%	$^1D_2 \rightarrow {}^3H_4$ (Pr^{3+})
Nd	–	–	–	–
Sm	561 nm	17829 cm^{-1}	1.0 %	$^5D_2 \rightarrow {}^7F_0$ (Sm^{2+})
				$^4G_{5/2} \rightarrow {}^6H_{5/2}$ (Sm^{3+}) (?)
	602 nm	16611 cm^{-1}	4.4 %	$^4G_{5/2} \rightarrow {}^6H_{7/2}$ (Sm^{3+}) (?)
	627 nm	15952 cm^{-1}	7.8 %	$^4F_{3/2} \rightarrow {}^6H_{5/2}$ (Sm^{3+}) (?)
	633 nm	15793 cm^{-1}	8.1 %	$^5D_1 \rightarrow {}^7F_0$ (Sm^{2+})
	687 nm	14548 cm^{-1}	4.3 %	$^5D_0 \rightarrow {}^7F_0$ (Sm^{2+})
	699 nm	14305 cm^{-1}	4.6 %	$^5D_0 \rightarrow {}^7F_1$ (Sm^{2+})
	730 nm	13695 cm^{-1}	4.3 %	$^5D_0 \rightarrow {}^7F_2$ (Sm^{2+})
	766 nm	13050 cm^{-1}	1.1 %	$^5D_0 \rightarrow {}^7F_3$ (Sm^{2+})
	817 nm	12238 cm^{-1}	0.5 %	$^5D_0 \rightarrow {}^7F_4$ (Sm^{2+})
Eu	384 nm	26071 cm^{-1}	100.0 %	5d → 4f (Eu^{2+})
	591 nm	16919 cm^{-1}	0.5 %	$^5D_0 \rightarrow {}^7F_1$ (Eu^{3+})
	616 nm	16228 cm^{-1}	0.9 %	$^5D_0 \rightarrow {}^7F_2$ (Eu^{3+})
	658 nm	15198 cm^{-1}	0.1 %	$^5D_0 \rightarrow {}^7F_3$ (Eu^{3+})
	694 nm	14419 cm^{-1}	0.4 %	$^5D_0 \rightarrow {}^7F_4$ (Eu^{3+})
	742 nm	13477 cm^{-1}	0.1 %	$^5D_0 \rightarrow {}^7F_5$ (Eu^{3+})
Gd	310 nm	32278 cm^{-1}	2.4 %	$^6P_{7/2} \rightarrow {}^8S_{7/2}$ (Gd^{3+})
Tb	379 nm	26418 cm^{-1}	4.4 %	$^5D_3 \rightarrow {}^7F_6$ (Tb^{3+})
	412 nm	24258 cm^{-1}	4.3 %	$^5D_3 \rightarrow {}^7F_5$ (Tb^{3+})
	434 nm	23026 cm^{-1}	3.1 %	$^5D_3 \rightarrow {}^7F_4$ (Tb^{3+})
	454 nm	22022 cm^{-1}	0.5 %	$^5D_3 \rightarrow {}^7F_3$ (Tb^{3+})
	471 nm	21248 cm^{-1}	0.9 %	$^5D_3 \rightarrow {}^7F_2$ (Tb^{3+})
	487 nm	20516 cm^{-1}	4.7 %	$^5D_4 \rightarrow {}^7F_6$ (Tb^{3+})
	543 nm	18424 cm^{-1}	14.2 %	$^5D_4 \rightarrow {}^7F_5$ (Tb^{3+})
	584 nm	17115 cm^{-1}	2.1 %	$^5D_4 \rightarrow {}^7F_4$ (Tb^{3+})
	620 nm	16141 cm^{-1}	1.2 %	$^5D_4 \rightarrow {}^7F_3$ (Tb^{3+})
Dy	479 nm	20875 cm^{-1}	15.9 %	$^4F_{9/2} \rightarrow {}^6H_{15/2}$ (Dy^{3+})
	571 nm	17521 cm^{-1}	21.4 %	$^4F_{9/2} \rightarrow {}^6H_{13/2}$ (Dy^{3+})
	658 nm	15199 cm^{-1}	0.8 %	$^4F_{9/2} \rightarrow {}^6H_{11/2}$ (Dy^{3+})
	749 nm	13358 cm^{-1}	0.4 %	$^4F_{9/2} \rightarrow {}^6H_{9/2}$ (Dy^{3+})
Ho	–	–	–	–
Er	–	–	–	–
Tm	345 nm	28966 cm^{-1}	0.9 %	$^3P_0 \rightarrow {}^3H_4$ (Tm^{3+})
	361 nm	27714 cm^{-1}	1.4 %	$^4D_2 \rightarrow {}^3H_6$ (Tm^{3+})
	451 nm	22194 cm^{-1}	3.1 %	$^4D_2 \rightarrow {}^3H_4$ (Tm^{3+})
	474 nm	21076 cm^{-1}	0.7 %	$^1G_4 \rightarrow {}^3H_6$ (Tm^{3+})
	511 nm	19567 cm^{-1}	0.3 %	$^4D_2 \rightarrow {}^3H_5$ (Tm^{3+})
Yb	–	–	–	–
undoped	347 nm	28845 cm^{-1}	0.2 %	–

	382 nm	26194 cm^{-1}	0.2 %	Eu^{2+} (?)
	493 nm	20298 cm^{-1}	0.1 %	–
	606 nm	16497 cm^{-1}	0.2 %	–

Undoped CSO

The undoped CSO sample, Figure 11, shows a 3D representation of TL emission spectrum (TL intensity versus wavelength and temperature) including a weak TL emission peak at about 100 °C with several emission bands, the main one at ~495 nm. This emission is due to intrinsic defects or contaminants, likely due to trace Mn^{2+} impurities [44 118]. On the other hand, when the samples are doped with lanthanides a variety of luminescence centers are introduced.

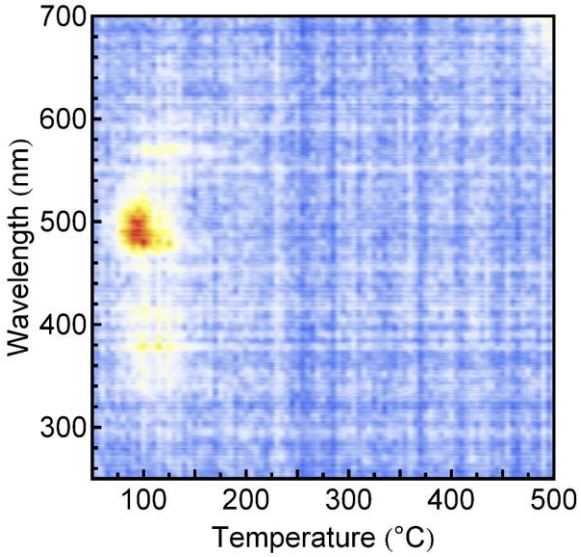

Figure 11. TL emission spectrum of undoped CSO (10 °C/s, 100 Gy). The weak emissions observed, could be due to contaminants.

If we take slices of the TL emission spectrum at $470\ nm < \lambda_{ave} < 500\ nm$, and plot the TL glow curve for that range of wavelength, we can compare the TL glow curve of the same sample obtained directly from TL Riso reader and confirm that the location of the main TL peak matches as seen in Figure 12.

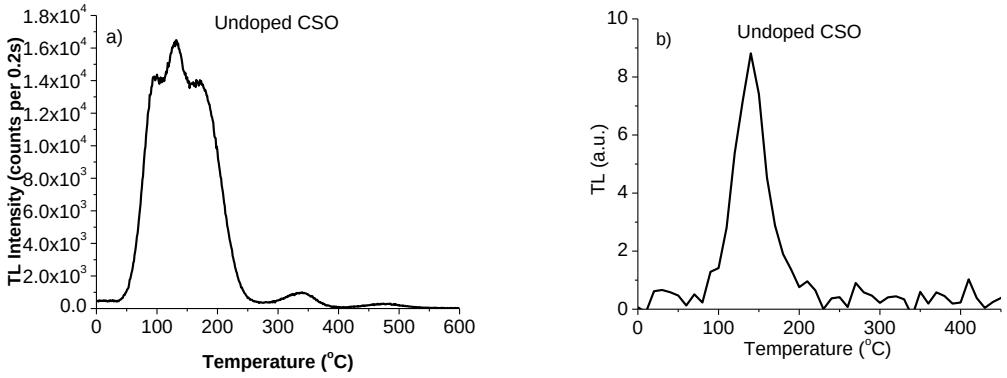

Figure 12. a) TL glow curve of undoped CSO, measured by TL Riso reader (5 ºC/s, 0.5 Gy, U-340). b) TL glow curve of undoped CSO, plotted by choosing the slices of the TL emission spectrum for λ_{ave} between 470- 500 nm (10 ºC/s, 100 Gy).

Similarly, if we take the slices of TL emission spectrum (Figure 11) at temperature of 100 ºC, and plot the emission spectrum (RL), and then compare it with the RL spectrum directly measured , we can see that the undoped sample shows only weak RL emission bands that cannot be definitively identified as observed in Figure 13 except from the emission at 382 nm which is possibly due to Eu contamination. The emissions at 347 nm with a good assumption might be due to traces of Tm and the emissions at 493 and 606 nm possibly indicate the traces of Dy.

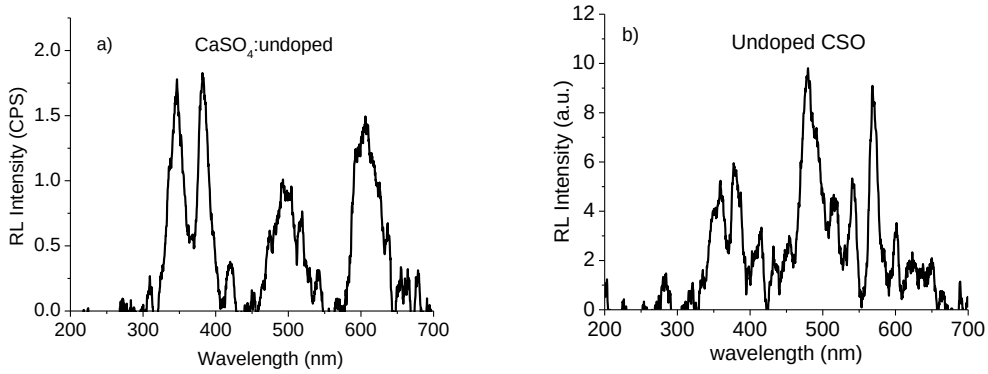

Figure 13. RL spectrum of undoped CSO measured a) directly and b) by choosing the slices of TL emission spectrum at T= 100 ºC.

CSO singly doped with lanthanides

We investigated CSO doped with different lanthanides of major interest for luminescence (Ce, Pr, Nd, Sm, Eu, Gd, Tb, Dy, Ho, Er, Tm, Yb). The resultant RL, TL, and TL emission spectra were characterized.

As an example of the measurements carried out, Figure 14(a) shows RL emission from $CaSO_4$:Eu, indicating Eu^{2+} emission at 380 nm and weaker Eu^{3+} emission around ~600 nm. Figure 14(b) shows that the main TL peak of this sample is at 180 °C, with a higher temperature peak around ~250 °C. Finally, Figure 14(c) shows the TL peak at 180 °C is associated with Eu^{2+} emission; whereas, the secondary peak at 250 °C is associated with Eu^{3+} emission.

(a) (b)

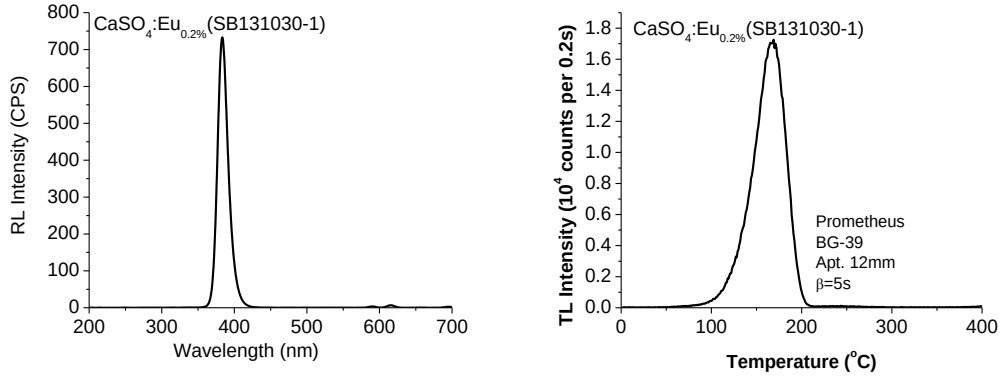

(c)

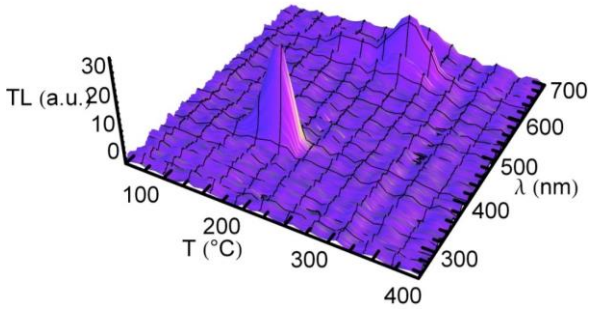

Figure 14. (a) RL spectrum of $CaSO_4$:Eu; (b) TL curve of $CaSO_4$:Eu (5 °C/s, 0.5 Gy, BG-39); and (c) 3D TL emission spectrum of $CaSO_4$:Eu (10°C/s, 100 Gy).

Figure 15 presents the 3D TL spectra of all CSO:Ln samples synthesized in this study. From these results, we can identify total of nine types of luminescence centers participating in the TL process of $CaSO_4$, eight of these centers (Ce^{3+}, Pr^{3+}, Sm^{3+}, Eu^{3+}, Gd^{3+}, Tb^{3+}, Dy^{3+} and Tm^{3+}) show the characteristic Ln^{3+} emission bands (or lines) as identified in Table 2. In CSO:Eu, both Eu^{2+} at ~384 nm and Eu^{3+} at ~ 591 nm and more are observed as we observed previously from RL spectrum (Figure 14a) . The emission bands of Ce are not clearly observed due to low intensity.

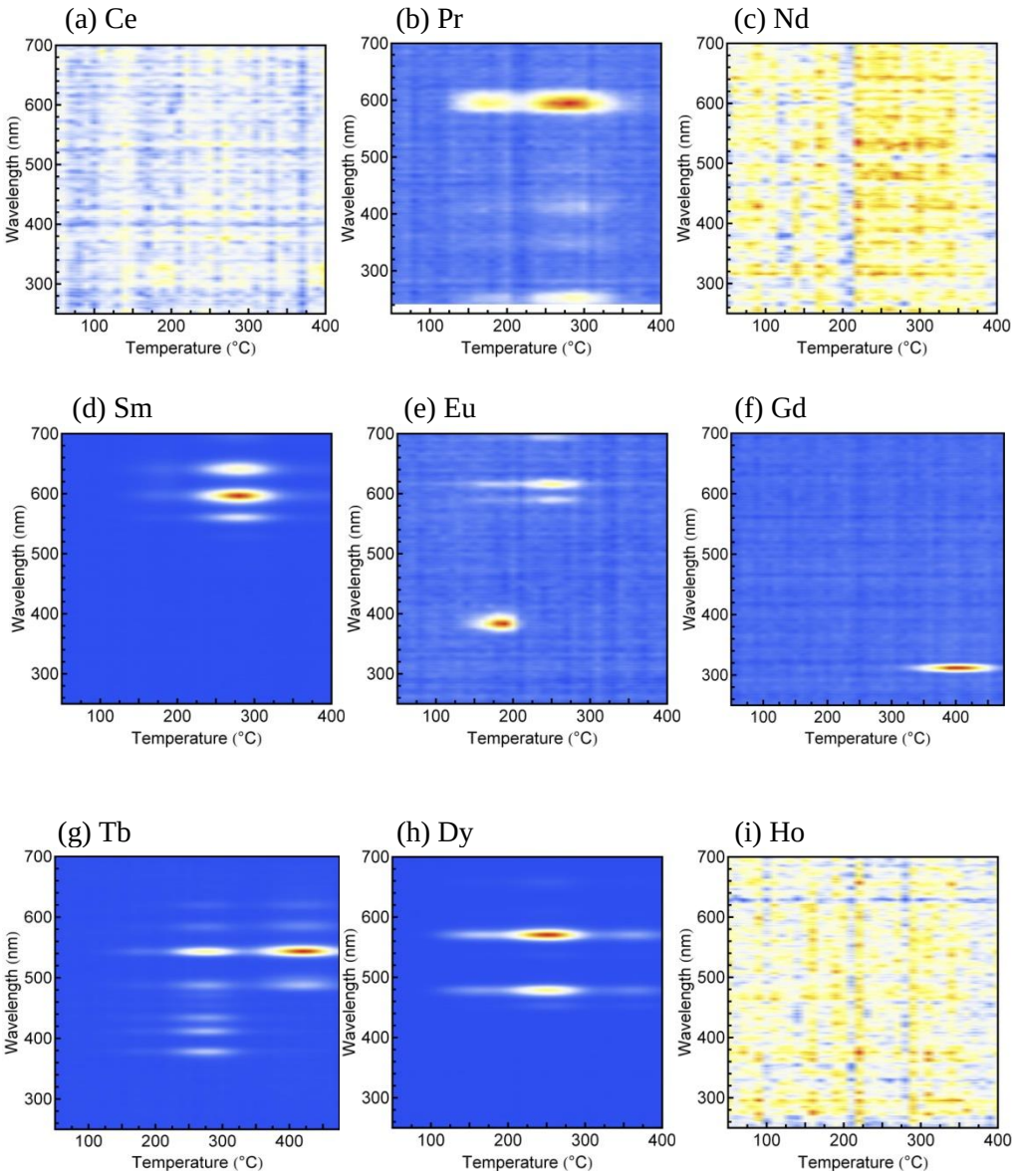

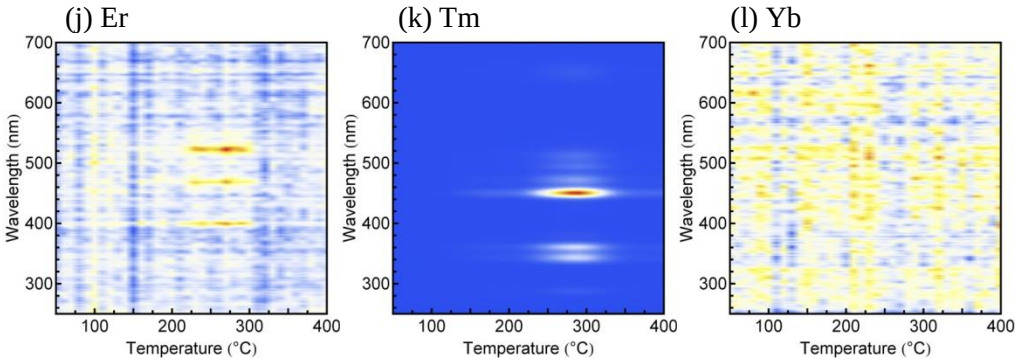

Figure 15. TL emission spectra of $CaSO_4$:Ln (10 °C/s, 100 Gy)

Furthermore, if we plot the absolute and normalized TL curves for various samples using either UV-transmitting filter or visible transmitting filter (see section 0) , there seems to be common TL peaks (Figure 16), resulting in TL emission with various intensities over a wide temperature range, from 50 °C up to 600 °C [38]. These peaks match the result reported by Nambi et al [33].

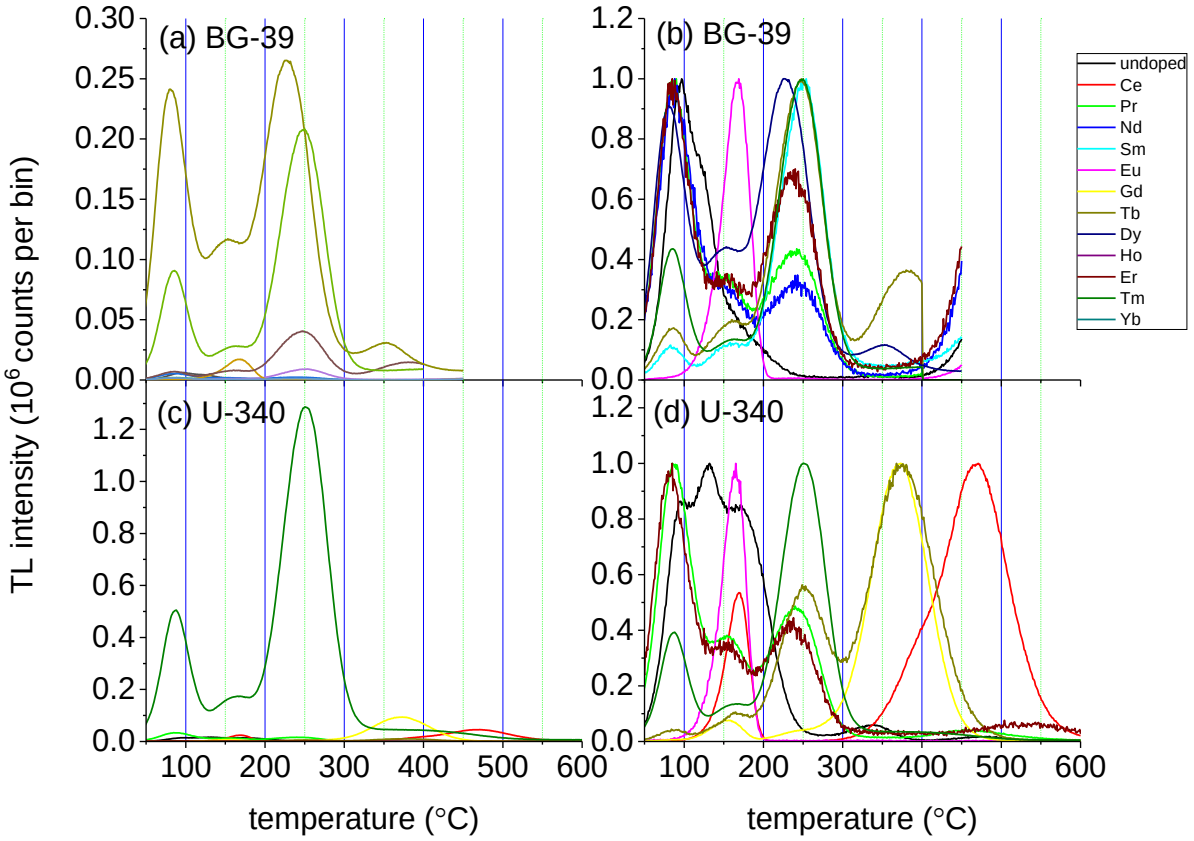

Figure 16. TL curves for $CaSO_4$:Ln measured using (a) Schott BG-39 filters (330 nm – 620 nm transmission) in absolute scale or (b) normalized, or (c) using Hoya U-340 filters (270 nm – 380 nm transmission) in absolute and (d) normalized. Only samples for which the TL intensity reached values > 1000 counts per integration period (0.2 s) were plotted.

Figure 17 shows a comparison of the maximum intensity of TL glow curves of this host material when doped with different lanthanides using both broad band optical filters. Although CSO:Tm showed the highest TL intensity in the UV range, this sample lacked the intense TL peaks for temperature above 300 ^{o}C. Ce and Gd doped samples showed TL peaks for temperatures above 300 ^{o}C. The emission in UV range that makes them interesting for the temperature sensing application.

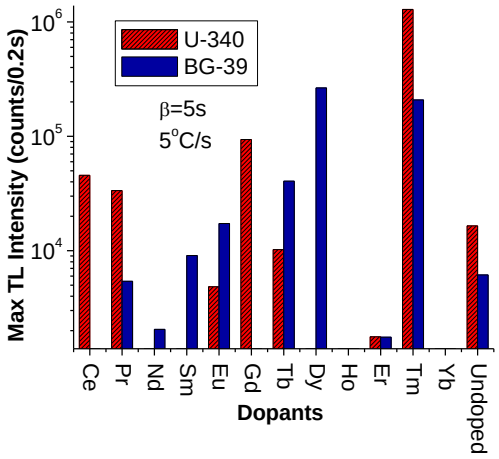

Figure 17. Comparison of maximum TL intensities of $CaSO_4$:Ln (0.5 Gy irradiation) when using Hoya U-340 and Schott BG-39 optical filters in front of the PMT.

The results confirm CSO:Ln as one of the most promising materials for temperature sensing, because of our ability to introduce different TL peaks using selected dopants, and because of the presence of high temperature TL peaks. Ce- and Gd-doped samples have the highest temperature peaks in the UV range and the Tm- and Dy-doped samples exhibit the most intense TL peaks in the visible range.

CSO with lanthanide co-doping

Following the influence of single dopants in the TL curve, we investigated the effect of co-dopants in order to introduce TL peaks at even higher temperatures.

CSO was co-doped with Ce because that leads to UV emission and a TL peak in the high temperature range (~500 °C), combined other co-dopants (Pr, Gd, Tb, and Tm) to obtain as many TL peaks as possible in a broad range of temperature. This selection was based on the 11 lanthanides investigated previously.

By co-doping/triple-doping lanthanides with Ce, we were able to produce multiple TL peaks at higher temperatures with more intensity compared to the singly doped samples. Figure 18 shows how co-doping of CSO affects the TL intensity of the material both in absolute and normalized

scales. As observed in Figure 19, the Ce^{3+} emission is the dominant emission in $CaSO_4$:Ce,Pr and in $CaSO_4$:Ce,Gd. The TL intensity of CSO co-doped with Ce and Pr is higher than the TL intensity of CSO singly doped with Ce or Pr. On the other hand, the position of the high temperature peak of the co-doped sample seems to have a 20 °C shift to the lower temperature comparing to the singly doped samples. The results also show that the co-doped sample combines the TL peaks from the singly doped samples. Similar observations can be made for Ce and Tb co-doping, and Ce and Gd co-doping [38].

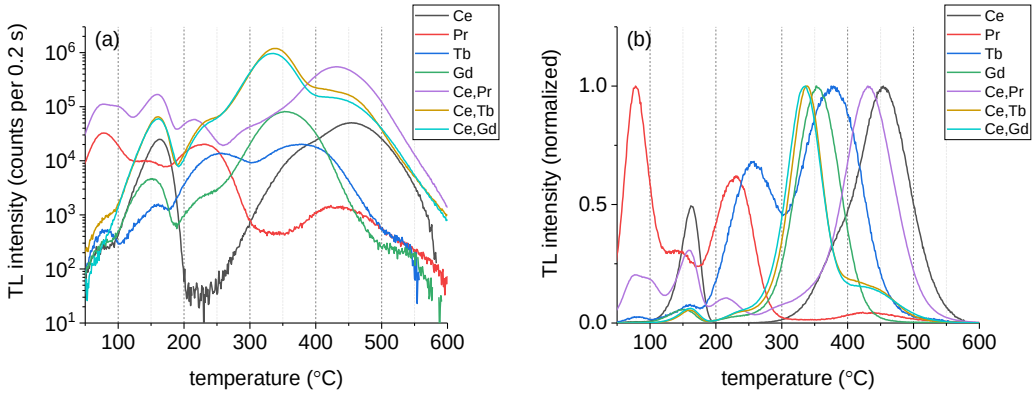

Figure 18. TL curves of $CaSO_4$ single-doped with Ce or X, or co-doped with Ce and X, X = Pr, Tb or Gd in (a) absolute and (b) normalized scales.

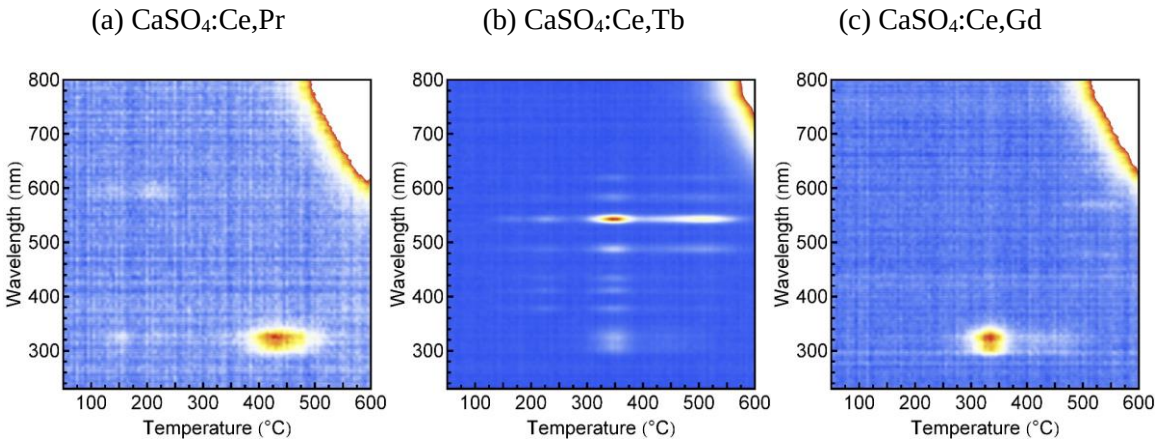

Figure 19. TL emission spectra of (a) $CaSO_4$:Ce,Pr, (b) $CaSO_4$:Ce,Tb and (c) $CaSO_4$:Ce,Gd.

In the case of Ce and Tm co-doping, however, the opposite influence is observed. The co-doped samples CSO:Ce, Tm showed lower intensity than the Tm-doped sample (Figure 20). The TL curve from the $CaSO_4$:Ce,Tm sample shows TL peaks typical of Tm-doped sample (85 °C, 150 °C and 250 °C) and TL peaks typical of Ce-doped sample (450 °C), although shifted to higher temperatures [38].

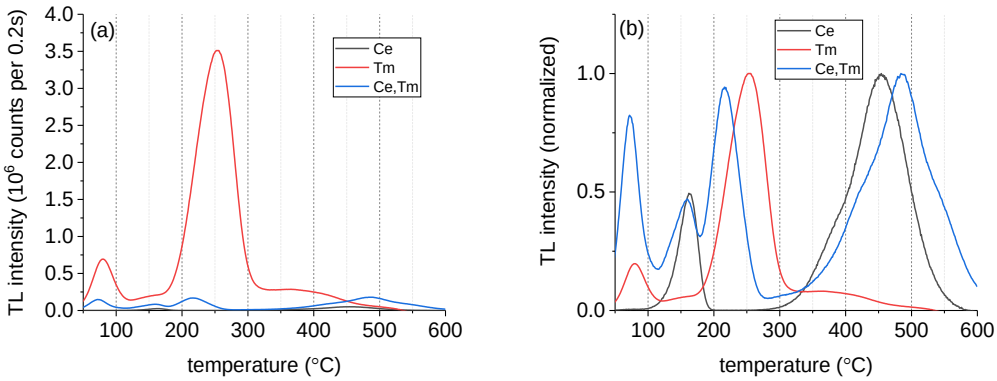

Figure 20. TL curves of $CaSO_4$ single-doped with Ce or Tm, or co-doped with Ce and Tm in (a) absolute and (b) normalized scale.

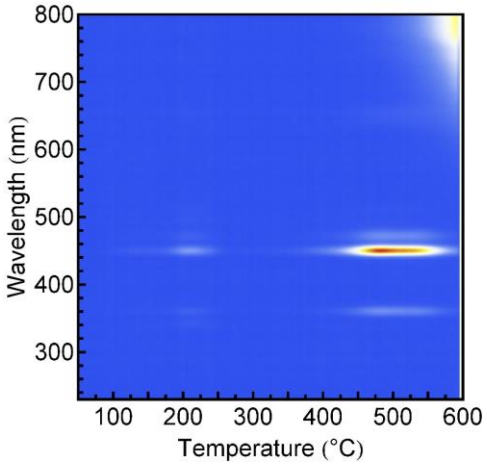

Figure 21. TL emission spectrum of $CaSO_4$:Ce,Tm.

The possibility of improving the samples for temperature sensing application was also investigated by triple doping CSO with Ce, Tb and Tm. Figure 22 shows the TL curves of $CaSO_4$ single-doped with Ce, Tb, and Tm, as well as co-doped with all three lanthanides. Although the TL intensity of

the triply-doped samples is not as intense as that of the Tm-doped sample (Figure 22a), a much wider variety of TL peaks is observed (Figure 22b). Similar to CSO:Ce,Tm sample, it is observed from Figure 23 that Tm^{3+} emission is dominant in the TL emission spectra of $CaSO_4$:Ce,Tb,Tm [38].

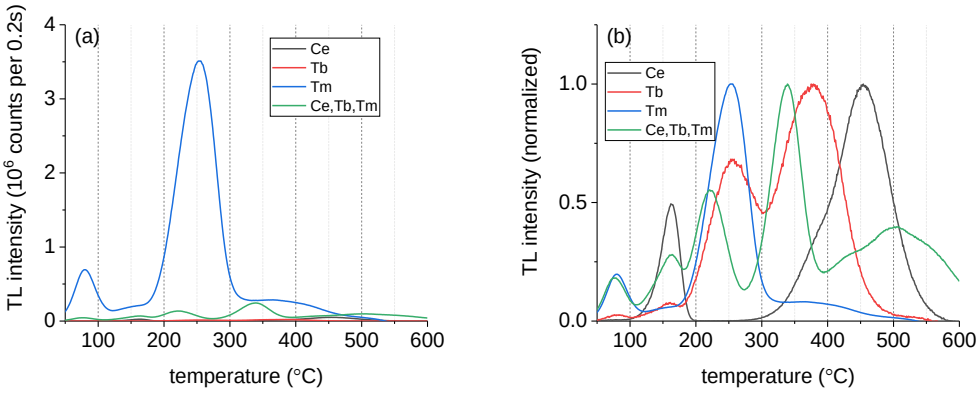

Figure 22. TL curves of $CaSO_4$ single-doped with Ce or Tm or Tb, or triple-doped with Ce and Tb and Tm in (a) absolute and (b) relative scales.

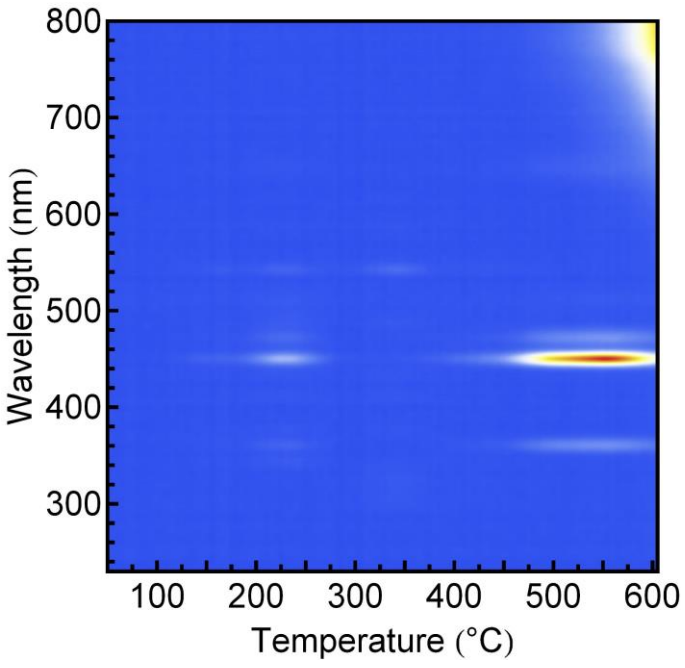

Figure 23. TL emission spectrum of $CaSO_4$:Ce,Tb,Tm.

Based on the results presented we can conclude that:

1. In samples co-doped with Tm, the intensity of TL curve is reduced but the position of TL peak is shifted to higher temperature comparing to the related singly doped samples (Figure 20 and Figure 22).
2. In other co-doped samples, the intensity of the TL from the co-doped sample is increased but the position of the TL peak is shifted to lower temperature comparing to the related singly-doped samples. (e.g., CSO:Ce,Pr)
3. A multiplicity of TL peaks was observed in all co/triply doped samples.

Finally, Figure 24 compares the maximum TL intensity of all co/triply doped CSO. The results show that CSO:Ce,Gd has the highest TL intensity. CSO:Ce,Tm is not as bright but has the highest temperature peak. Being the second brightest sample, CSO:Ce,Pr shows both multiple TL peaks as well as having the peak in higher temperature range. Based on the results above, CSO:Ce,Pr seems to be the most promising material for temperature sensing.

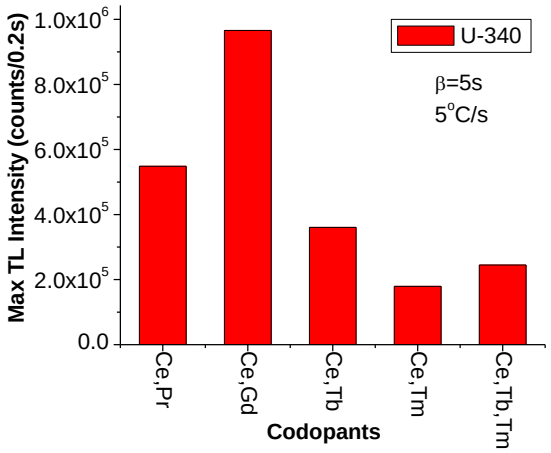

Figure 24. Comparison of the maximum TL intensity of co/triply doped CSO.

Effect of alkali metal co-dopant

Continuing with the development of CSO, we investigated if alkali metals could be used to introduce additional defects in CSO and extend the temperature range of this material towards higher temperatures. Inspired by the effect of Li dopant to improve the luminescence emission in other materials, we examined the role of Li, Na and K as possible charge compensators in order to improve the Ln incorporation into the crystal lattice of CSO [45, 46]. The final goal of this section was to codope CSO containing the lanthanides of interest with these three alkali metals. We started from Pr as the lanthanide since it has a bright TL peak and its emission can be clearly seen in TL emission spectra. Figure 25 and Figure 26 shows how co-doping CSO with alkali metals affects the TL properties of the material. In all three samples co-doped with Li, Na and K, the TL intensity of of CSO co-doped with Pr and the alkali metal is higher than the TL intensity of CSO singly doped with Pr or the alkali metal but this effect is only observed in the lower temperature region, and unfortunately the multiplicity of peaks has decreased especially in higher temperatures [38].

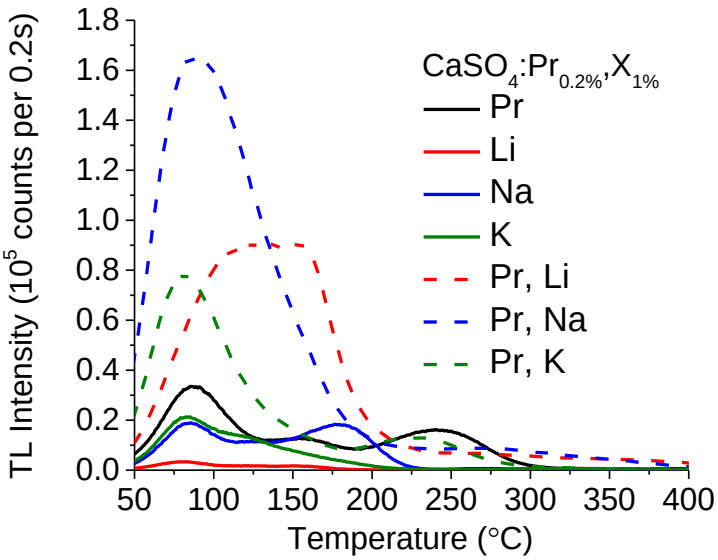

Figure 25. TL curves of $CaSO_4$single-doped with Pr or X, or co-doped with Pr and X, X=Li or Na or K.

(a) Pr,Li (b) Pr,Na (c) Pr,K

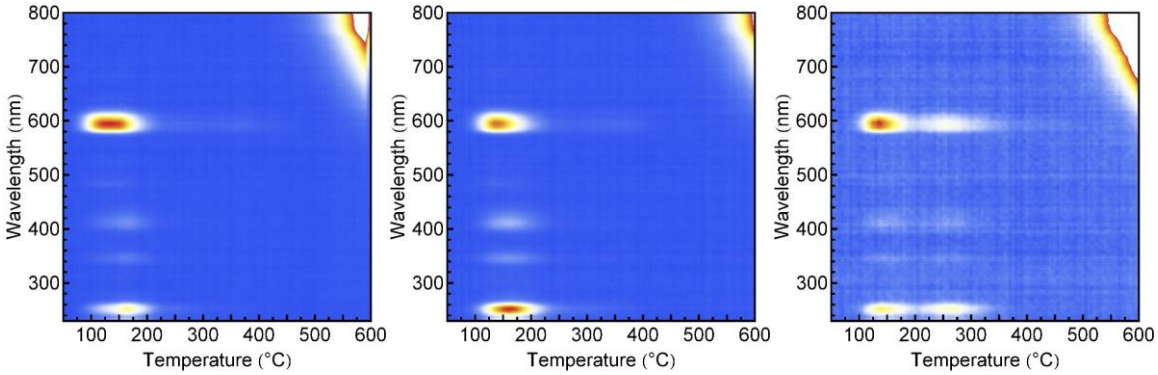

Figure 26. TL emission spectrum of (a) $CaSO_4$:Pr,Li, (b) $CaSO_4$:Pr,Na, and (c) $CaSO_4$:Pr,K.

For temperature sensing applications, we are interested in those samples with multiple TL peaks and in the high temperature zones. Therefore, we conclude that co-doping with alkali metals is not advantageous at least in case of Pr as a lanthanide co-dopant. In future, this study can be broadened to those samples that haves already show high-temperature TL peaks such as CSO:Ce and CSO:Ce,Tm.

Other optimization studies

Acid concentration

To investigate the amount of sulfuric acid that results in maximum TL intensity, $CaSO_4$:Ce,Tb samples were synthesized by co-precipitation as described by Doull et al. [13] using three different amounts of sulfuric acid: the amount that stoichiometrically balances the reaction, $CaCO_3 + H_2SO_4 \rightarrow CaSO_4 + H_2O + CO_2$; an amount that neutralizes the pH upon the conclusion of the reaction (145% of the stoichiometric amount), and an amount as in Doull et al. [13] (360% of the stoichiometric amount). Excess acid was removed by evaporation and calcination of the precipitate. The amount of acid that neutralizes the pH was obtained by dropping the diluted acid into the mixture of $CaCO_3$ and dopants gradually. We then waited for the solution to reach its balance and

read the required pH, as monitored using a digital pH meter (Omega- model PHH-37). The process continued until the solution reached the neutral pH (~7).

Figure 27 shows the TL results from the respective sulfuric acid synthesis amounts. The synthesis using 360% of the stoichiometric balance of sulfuric acid had the greatest TL intensity and, as a result, was the amount used through the duration of this study.

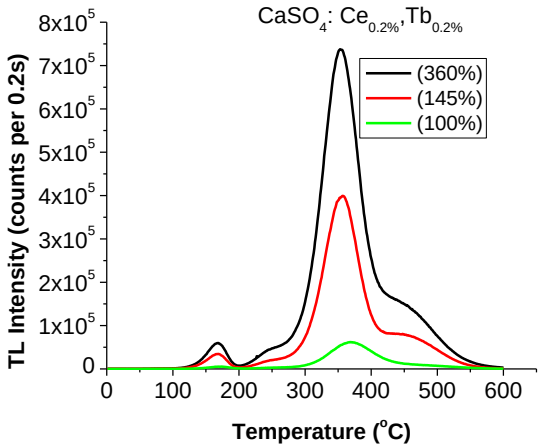

Figure 27. TL glow curves of $CaSO_4$:$Ce_{0.2\%}$,$Tb_{0.2\%}$ with different amounts of sulfuric acid as a percent of stoichiometrically balanced amount (5°C/s), dose: 0.5 Gy, filter: U340.

To avoid evaporation of the acid excess, we also investigated another method to remove the unreacted acid. After the acid was poured into the solution completely, the solution was heated on a hot plate at 170 °C for 30 min. Then the solution was cooled to room temperature and poured into several test tubes. The test tubes rested at room temperature for 4 h to let the $CaSO_4$ precipitate. The liquid was then pipetted from the top of precipitate and the test tubes were rinsed with deionized water into a beaker. The solution was then heated at 200 °C until it completely dried. The product was annealed in a box furnace at 700 °C for 2 h.

Figure 28 compares the TL intensity and shape of TL peak for materials synthesized using this method to those specimens synthesized with the methods used by Doull et al. [13]. As can be seen from the figure, the TL intensity of the sample synthesized via acid separation is slightly more and

has a small shift toward lower temperature i.e. ~10 ^{o}C and ~20 ^{o}C for lower and higher temperature peak, respectively. Therefore, for future synthesis this new method can be used.

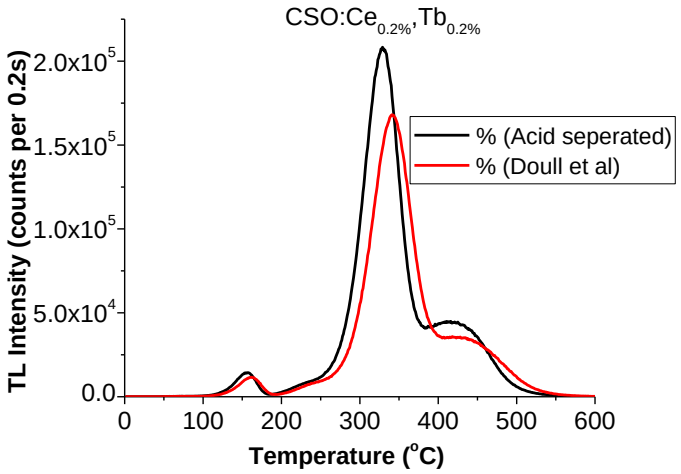

Figure 28. Comparison between the TL curve of acid-separation method and the acid-evaporation method

Particle size measurement

To verify that the particles have suitable properties for temperature sensing (i.e. fast response in time), additional investigations were carried out to ensure that the particles are sufficiently small (< 13 μm). TL for sieved and non-sieved material is compared in Figure 29. As it can be seen, CSO TL curve was not changed after sieving. This can be used as verification that CSO sample was not adversely affected after passing through the sieve. SEM images are shown in Figure 30 and confirm that most particles have at least one dimension <13 μm.

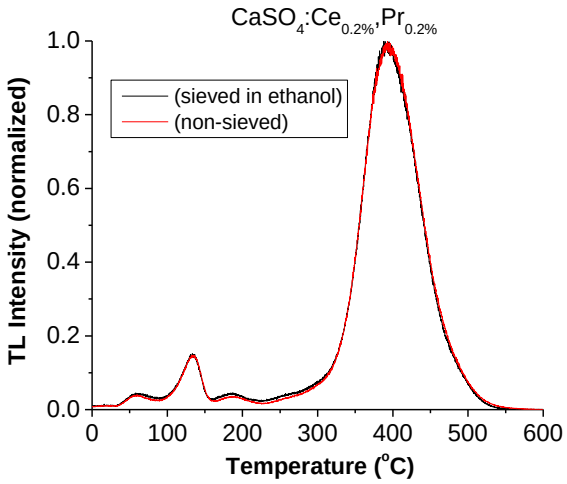

Figure 29. Normalized comparison of the prepared CSO compared with not milled and sieved material. Ethanol sieving do not change the TL properties of the material.

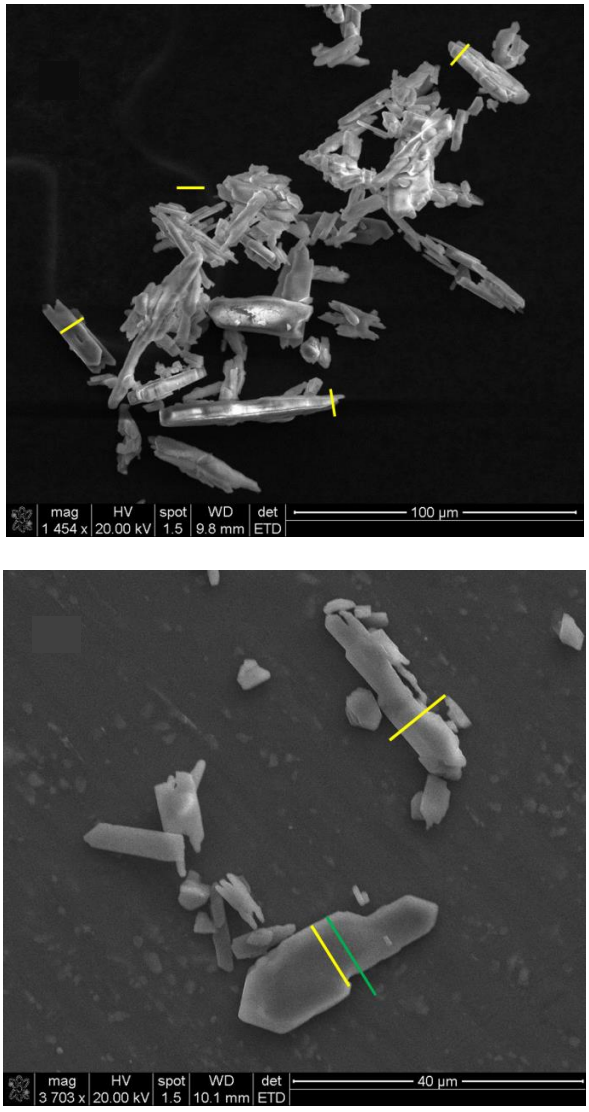

Figure 30. SEM for CSO. Scaled lines have been added as a help to the reader. The yellow lines are approximately 10 µm and green lines are approximately 13 µm. They were added using the scale in an image processing software. As can be seen, most of the particles imaged have at least one cross section <10 µm.

CHAPTER VI

FEASIBILITY STUDIES ON METHODS TO CHARACTERIZE THE TL KINETICS OF CALCIUM SULFATE

The objective of this chapter is to investigate the feasibility of various methods to characterize the kinetics of the TL in CSO, including the determination of the order of kinetics and the activation energy.

Order of Kinetics

Dose Response

Three aliquots of each sample, CSO:Pr, CSO:Tb, CSO:Tm were irradiated with different doses (0.1, 0.2, 0.5, 1, 2, 5, 10, 20, 50, 100, 200, and 500 Gy). Apertures were used in front of the PMT in the case of high doses to prevent saturation of the PMT and/or counter. In the case of CSO:Tm, we could only go up to 200 Gy of irradiation since the TL intensity was very high and close to the saturation capacity of the PMT even when using the smallest aperture available in the lab (4 mm) as seen in Figure 31. Example of TL curves for only one aliquot of each sample in both normal and log scale are shown in Figure 31. We plotted the log scale to be able to track the position of the TL peaks more accurately.

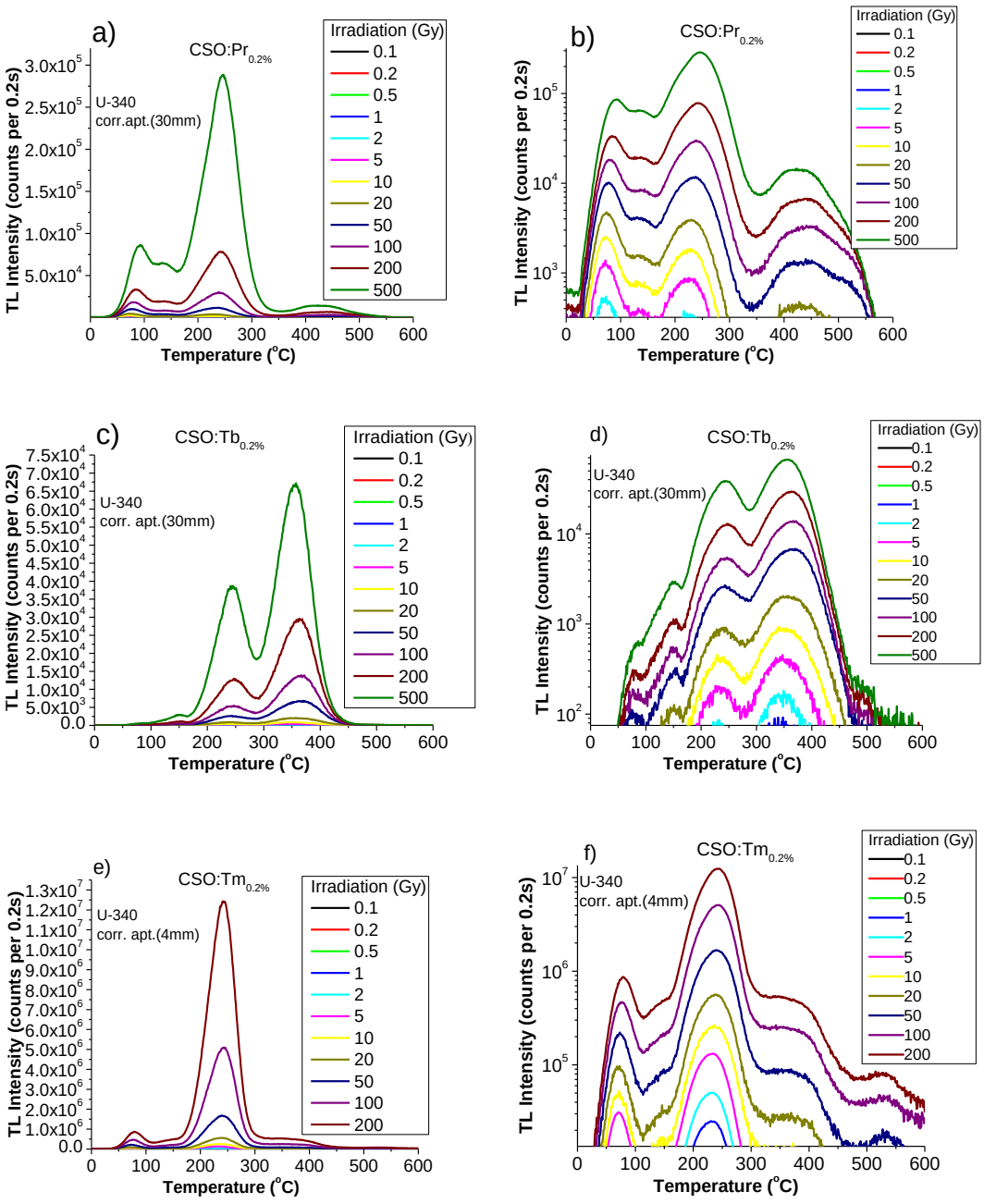

Figure 31. Dose dependence curves in normal and log scale for a,b) CSO:Pr, c,d) CSO:Tb, and e,f) CSO:Tm. Correction aperture is used is needed to prevent the PMT saturation. Heating rate: 5 ºC/s, UV transmitting filter used.

In order to identify the linearity dependence of the TL intensity on irradiation dose, the dose-response curves of the same samples are plotted (see Figure 32). This is the first step to predict the behavior of the traps as they are being filled.

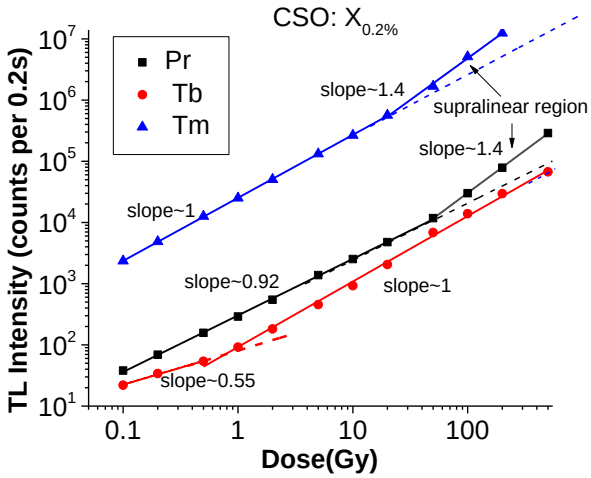

Figure 32. Dose-response plot for CSO:Pr, Tb, and Tm. Heating rate: 5 ºC/s

The dose dependence data show the position of the majority of the TL peaks is not shifted as the traps are being filled (Figure 31). The dose response plot shows that TL intensity of the maximum peak has a linear relationship with the given dose during trap filling for a part of the graph (over a wide dose range) as identified in Figure 32 i.e. the slope of the graph of Ln(I) versus Ln(D) (D being irradiation dose) is one. To evaluate the kinetic order, we need to take a look at the behavior the TL peak as the traps are emptied i.e. step annealing data. For higher does, however, the slope of the graph for Pr- and Tm-doped samples is more than one. This behavior is called supralinearity and is due to the competition between the traps during the heating stage. Briefly, during heating, the electrons released either recombine with holes to produce TL signal or be retrapped in the deeper traps. The deeper traps act as competitors for the recombination sites resulting in supralinearity [25].

Step annealing data

Three aliquots of CSO:Pr, CSO:Tm and CSO:Eu were used for step annealing. We chose CSO:Pr and CSO:Tm for their high-temperature, high intensity TL peaks that are well-separated in the low temperature zone so we can easily analyze them . Figure 33a and Figure 34a show the step

annealing data obtained by pre-heating (50 ºC- 500 ºC) the samples with the steps of 5 ºC. We plotted T_m-T_{stop} graphs to show the peak positions as a function of pre-heating temperatures as can be seen in Figure 33b and Figure 34b.

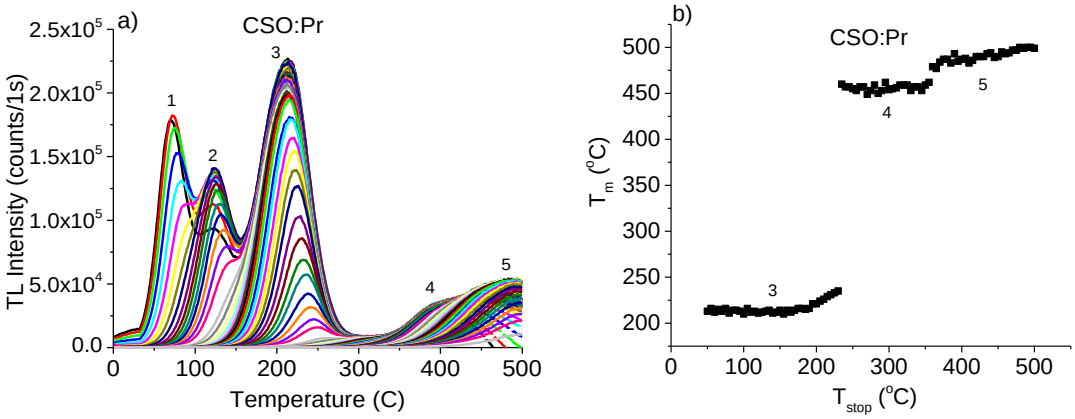

Figure 33. a) Step annealing data obtained from CSO:Pr in 5 ºC steps. UV transmition filter used, Irradiation: 5 Gy, Heating rate: 1 ºC/s. b) T_m-T_{stop} plot obtained from the step annealing data

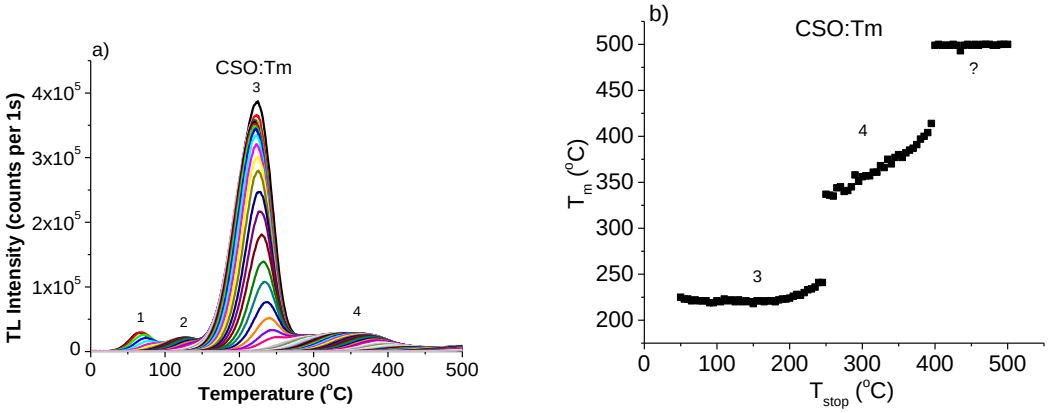

Figure 34. a) Step annealing data obtained from CSO:Tm in 5 ºC steps. UV transmition filter used, Irradiation: 5 Gy, Heating rate: 1 ºC/s. b) T_m-T_{stop} plot obtained from the step annealing data

In figure above, the peaks are identified with numbers for each sample. Figure 33 shows that for Pr doped sample, peaks 4, and 5 have a relatively constant position indicating first-order kinetics (see Figure 8). In addition, the behavior of the dominant TL peak; peak 3; in both CSO:Pr and CSO:Tm samples is an indicator of non-first-order kinetics (Figure 33 and Figure 34). However, in Tm doped sample, the behavior of peak 4 indicates either the 2nd-order kinetics or the close overlap of several

peaks. In this case, the definitive conclusions are not possible. The peaks in less than 150 ^{o}C are not shown in the T_m-T_{stop} plots, due to low temperature phosphorescence that can possibly hinders the TL signal in that region.

Initial rise method (IRM)

As discussed in section 0, three approaches were used to apply IRM to TL data in order to find the activation energy. We chose CSO:Eu to compare these three approaches since this sample has a single peak that makes it easy for our analysis. Figure 35 shows the step annealing data for CSO:Eu. The three approaches will be explained in the following sections using this plot.

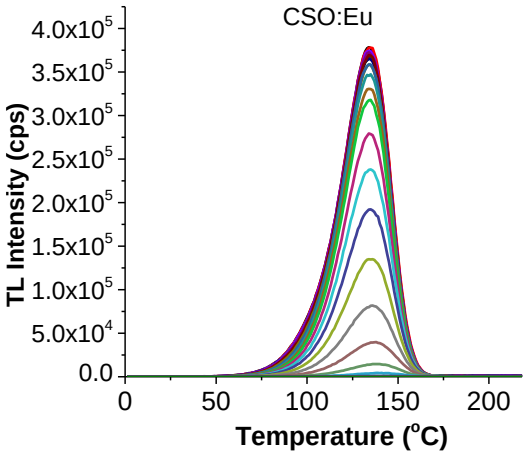

Figure 35. Step annealing data from CSO:Eu in 5 ^{o}C steps. Visible light transmition filter used, irradiation: 5 Gy, correction aperture: 30 mm, heating rate: 1 ^{o}C/s

IRM/ estimation by eye

In this approach after plotting Ln (I) versus 1/kT of the step annealed data, we chose to recognize the initial part of the graph looking for the most linear, small section of the graph as shown in Figure 36a. The slope of the linear part of the graph is *–E*. If we plot the activation energy values versus the T_{stop} and take the average value of activation energy data points by fitting a straight line

in the most linear initial part of the plot, the activation energy for the TL peak of the Eu doped sample can be calculated (Figure 36b).

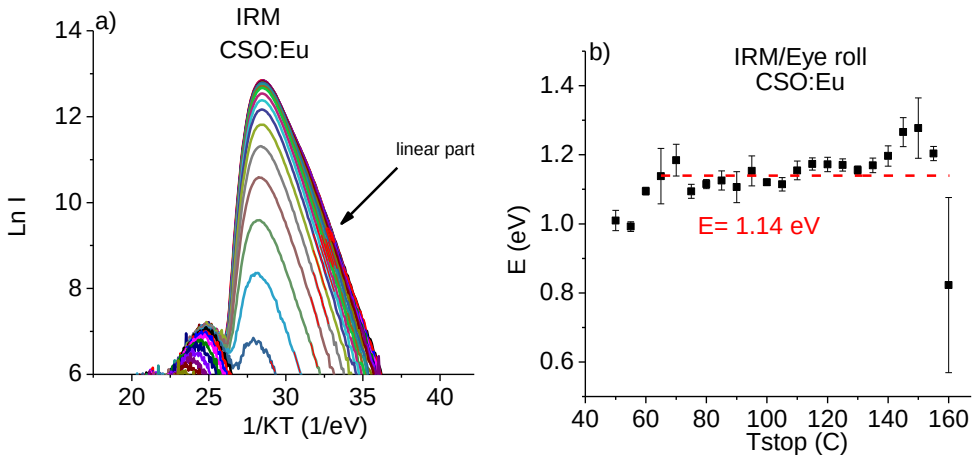

Figure 36. a) Initial rise data obtained from CSO:Eu step annealing curve. The red lines indicate the linear part of the graph observing by eyes. b) Activation energy calculated for each pre-heated TL curve. The red dashed line shows the average of activation energy in the most linear part the plot

Constant-temperature

In this approach, after plotting Ln (I) vs 1/kT, each curve is divided into the temperature zones in which the initial part of the graphs have fixed temperature range (Figure 37a). Then, the slope of linear fit in each fixed temperature range is read. We continued the fitting until the graph appears to be non-linear in that temperature zone, then we shifted the fitting to a new temperature zone. We called this approach the “const. temp” method (Figure 37b).

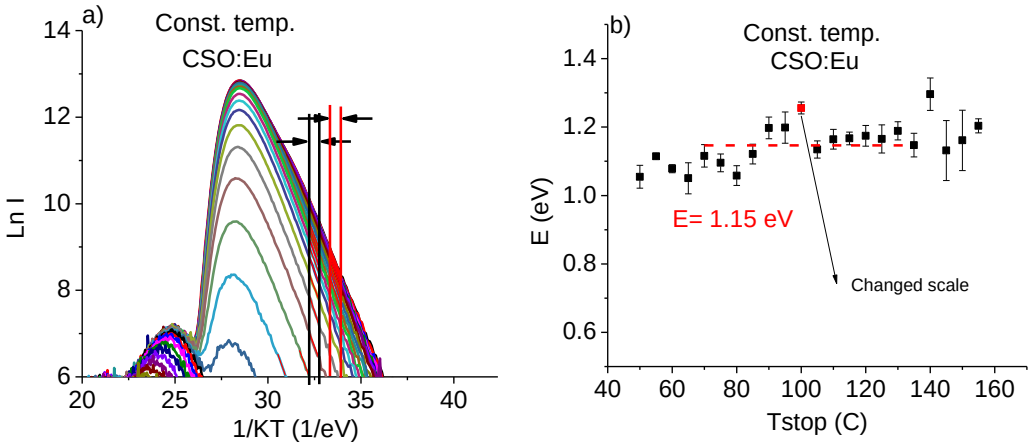

Figure 37. a) Initial rise data obtained from CSO:Eu step annealing curve. The zones in which the initial rise part of the graph has fixed temperature range is defined by red and black slots . b) Activation energy calculated for each pre-heated TL curve using const. temp. approach.

Traditional approach (<10% I_{max})

This approach is the traditional way of measuring the slope of the initial rise of the Ln (I) vs 1/kT graph. In this approach, linear fitting is employed only to the initial part of the graph in which the temperature does not exceed 10% of the correspondent I_{max} as shown in Figure 38.

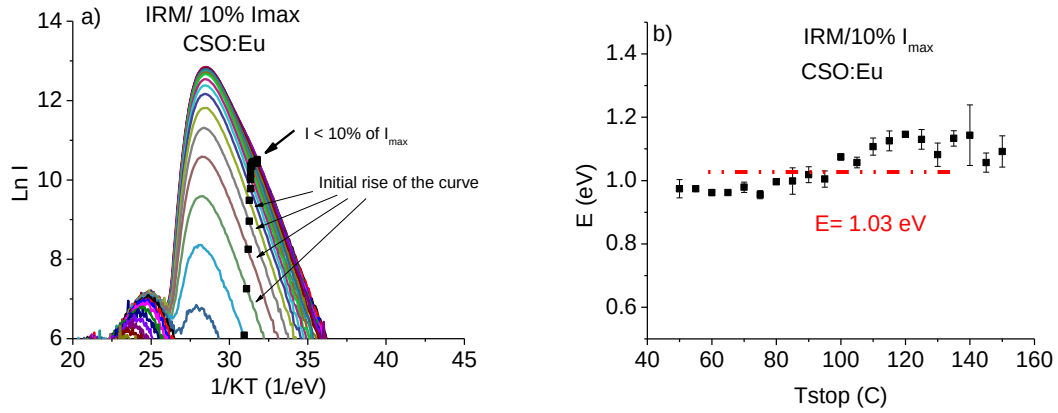

Figure 38. a) Initial rise data obtained from CSO:Eu step annealing curve. Red lines indicate linear fits calculated in the Origin 8.6. b) Activation energy calculated for each pre-heated TL curve.

Comparing the three method used for IRM, one can see that with a good approximation, estimation by eyes and constant temperature methods results in the same activation energy. However, E

calculated by the traditional method is different perhaps due to the larger initial part of the graph chosen that includes the noisy non-linear data.

IRM for CSO:Pr and CSO:Tm

In this section, we used two of approaches of IRM to calculate the activation energy of CSO:Pr (Figure 39), and CSO:Tm (Figure 40). The step annealing data were shown in Figure 33a and Figure 34a. The boxes indicate regions of interest.

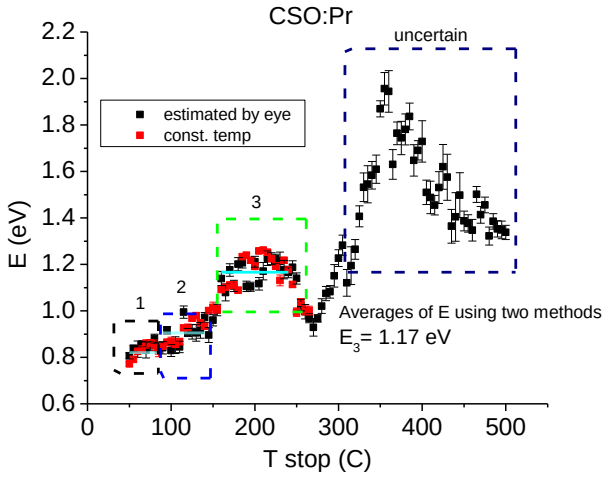

Figure 39. Calculated activation energy for CSO:Pr using the step annealing data, the average activation energy in three regions of interest is calculated

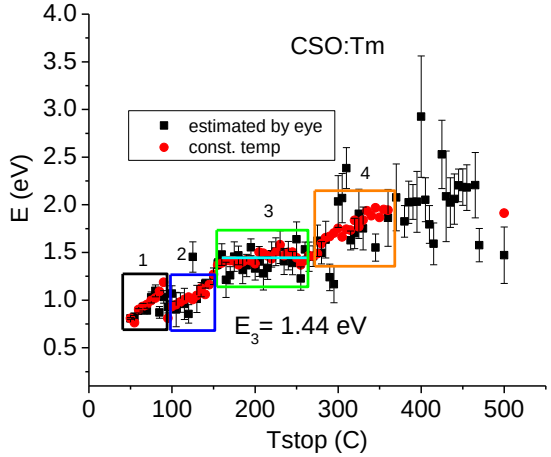

Figure 40. Calculated activation energy for CSO:Pr using the step annealing data

Based on the figures above, the average activation energies for CSO:Pr and CSO:Tm samples are calculated and shown in Table 3. For CSO:Tm, regions 1, 2, and 4 have too much peak overlap and the peaks are too small to get the accurate data. Equation 3.15 was used to calculate the frequency factor.

Table 3. Results obtained from CSO:Eu, CSO:Pr, and CSO:Tm step-annealing and initial rise analysis

Sample	Peak	Average Activation Energy (eV)	Frequency Factor	T_m (°C)	T_{stop} Range (°C)
CSO:Eu	1	1.15 ± 0.01	$(4.26 \pm 1.05)\times10^{08}$	300 ± 1	90-120
CSO:Pr	3	1.17 ± 0.01	$(7.28 \pm 3.97)\times10^{10}$	214 ± 5	50- 120
CSO:Tm	3	1.44 ± 0.01	$(3.58 \pm 1.62)\times10^{13}$	220 ± 3	150-200

The maximum frequency factor is expected to be in the range of ~10^{10}-10^{14} s^{-1}, although values outside this range can be found [42].

Various heating rate method (VHR)

Figure 41a shows the TL curves of CSO:Eu for various heating rates. The peak positions (T_m) were obtained and the plot of $Ln(\frac{T_m^2}{\beta})$ versus $1/KT_m$ was fit (Figure 41b) to obtain activation energy and frequency factor as explained in section 0. The results are shown in Table 4.

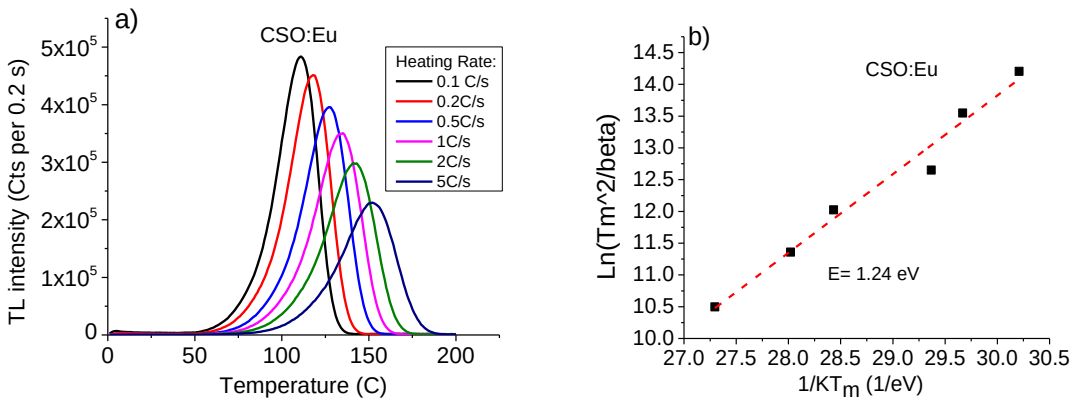

Figure 41. a) TL curve of CSO:Eu sample for heating rates between 0.1-5 ºC/s. b) plot of $Ln(\frac{T_m^2}{\beta})$ versus $1/KT_m$ to calculate E from the slope and s from the y-intercept. Optical filter BG-39, aperture 30mm, 1 mg of sample was used.

Table 4. CSO:Eu activation energy and frequency factor obtained from VHR method

Sample	Average Activation Energy (eV)	Frequency Factor
CSO:Eu	1.24 ± 0.09	$(1.89 \pm 0.14)\times10^{14}$

As can be seen from the table above, the calculated E for CSO:Eu is different from the obtained result using IRM. This could be due to the effect of thermal quenching (TQ). If thermal quenching is occurring, the area under the TL curve decreases as the heating rate is increasing, and the measured TL curve would be the Randal-Wilkins function multiplied by the thermal quenching function ($I_{measured}= I_{RW}\times I_{TQ}$) . Therefore, the corrected TL curve would be the measured data divided by the I-TQ curve. Unfortunately, we do not have any data regarding the thermal quenching available. Therefore, the presented result for E and s obtained from VHRM is just to show how the technique works and not the corrected values.

CHAPTER VII

CONCLUSION OF PART 1

To conclude the first part of this work, we synthesized CSO with the co-precipitation method and the optimal conditions of synthesis were determined. Then, a characterization of the radioluminescence and thermoluminescence of Ln-doped samples was provided. In RL, typical Ln^{3+} emission was observed, in addition to Sm^{2+} and Eu^{2+} emission. In TL, the emissions were mostly from Ln^{3+}, except for Eu^{2+}. Next, we studied the effect of co-doping samples in which the TL intensity was higher than the combination of the single-doped samples. In addition, by co-doping lanthanides, TL peaks over a wide range of temperatures were produced. Moreover, co-doping lanthanides with alkali metals produced adverse effect for our purpose. The results of material development show that by the appropriate choice of dopant, we can produce samples suitable for temperature sensing applications. Based on our result, we proposed CSO:Ce,Pr as the most appropriate sample for temperature sensing.

The kinetics of the TL in CSO was studied with several techniques (dose response, IRM, VHRM). In IRM, we used three methods and we concluded that eye screening of graph and the constant-temperature method result in more accurate E. Finally, E and s was found for the dominant peak of CSO:Eu, CSO:Pr, and CSO:Tm.

PART TWO

Gold Nano-Particles

CHAPTER VIII

INTRODUCTION

Over the past several decades, developments in synthesis and characterization techniques of nanoparticles have shown their utility in various biomedical applications such as bio-imaging [47, 48], tumor targeting [49], and drug delivery [50, 51]. Among them, gold nanoparticles (GNPs) have been investigated over the years for various applications in cancer diagnosis and therapy.

In particular, GNPs have been proposed as novel candidates for radiosensitizing due to their strong photoelectric absorption coefficient and ease of synthesis. The photoelectric absorption cross-section and, subsequently, the radiotherapy effects of the radiosensitizing agent, are directly determined by their atomic radius. In this regard, gold (Z=79) is an ideal candidate for radiotherapy. NPs with a larger atomic radius than gold atoms (~0.17 nm) are known to have a strong radiation enhancement effects [52]. GNPs injected into patients can be delivered to tumors either by passive or active targeting. In passive targeting, GNPs of certain sizes enter into the tumor tissue more readily compared to normal tissue due to large size of the tumor's blood vessel pores, the poor lymphatic drainage (movement of lymph fluids around the cells) from the tumor tissue, and the leakiness of the newly formed blood vessels in tumors. The consequent effect is called Enhance Permeability and Retention (EPR). The EPR effect leads to the blood vessel walls not sealing tightly together, leaving enough space (200-800 nm) for GNPs to accumulate in the tumor tissue [53]. The active targeting works by conjugating GNPs with a variety of ligands such as antibodies or peptides specific to the cancer cells which leads to the binding of targeted GNPs to tumor cells with specific antigens or receptors.

Molecular Imaging is considered a very important tool for cancer diagnosis, management, and the follow up of this disease. Of all the molecular imaging modalities, the two most sensitive non-invasive ones are nuclear imaging modalities, namely Positron Emission Tomography (PET) and Single Photon Emission Computed Tomography (SPECT). As these two modalities are expanding, the need for the new agents and strategies to be used with them is also increasing. Moreover, there has been a great interest to merge diagnostic and treatment functions within a single tool. The agents that can be used as both diagnostic and therapeutic agents (theranostics), such as GNPs, can make this interest happen. GNPs have a potential to be easily loaded with a variety of targeting and/or therapeutic agents due to their well-developed surface chemistry.

However, the same challenges for using GNP for in vivo imaging also hinders their application for radiotherapy and other clinical applications. One of the most important challenges is that GNPs administered to patients are distributed both to tumors and normal tissues, therefore, without accurate and detailed information about the distribution of GNPs in vivo, severe damage can occur to healthy tissue when radiotherapy is administered. In addition, toxicity to surrounding healthy cells often limits the maximum irradiation dose that can be delivered to tumors [54, 55].

Therefore, the second part of this dissertation focuses on this area of research. The main objective is to develop novel hybrid GNPs that are suitable for use as radiosensitizers for radiation therapy and allow PET imaging to determine their localization. In the following chapters, we focus on the synthesis of novel GNPs and their application for bio-imaging. The novel ^{64}Cu (a positron-emitter with a half-life of 12.7 h) doped Cu@Au GNPs we are developing have a core-shell (copper core and gold shell) structure with the majority of material (>90%) being gold and therefore is expected to have similar radiosensitization properties to conventional GNPs. Our hybrid GNPs are inherently radioactive (radionuclides are located in the core), therefore, we expect a lower risk of radionuclide dissociation, which in turn can lead to more accurate in vivo imaging and will allow us to administer the radiotherapy with minimal collateral damage.

CHAPTER IX

BACKGROUND

Gold Nanoparticles and Synthetic Methodologies

Historical Background

Around the 5th century BC, Egyptian and Chinese authors first mentioned solutions of gold (Au) and their healing powers. A very famous example of using colloidal Au in aesthetics is the Lycurgus Cup, which displays a red color in transmitted light and a green color in reflected light due to gold nanoparticles used in its structure (Figure 42)[56]. In the middle ages, soluble gold was used in medicine to cure a great variety of diseases such as heart problems, epilepsy and tumors as reported in a book by the medical doctor Francisci Antonii in 1618 [57]. Michael Faraday was the first to study the gold nanoparticles in a scientific way around 1850. He noticed that the red color of gold particles was due to their tiny size and introduced a technique to turn that color to blue [58]. He also reported the formation of colloidal gold by reduction of $AuCl_4$ solution by phosphorus in CS_2 [57]. After Faraday, several scientists developed techniques to synthesize gold particles. To date, there have been many reports on the size and shape of GNPs varying from nanoshells, nanorods, nanocages to nanostars [59, 60].

Figure 42. Lycurgus Cup, left-reflected light and right-transmitted light (taken after [61])

Synthesis of Gold Nanoparticles

Gold nanoparticles have a long history in synthesis and characterization. Many properties of GNPs are related to the ratio of their surface area to their volume and the spatial confinement of the electrons and the electric fields in and around them [62]. In order to make particles with specific size and shape, we need to have a good knowledge about the bonds between the particle surface and the stabilizing agents. The GNPs are usually formed when the Au(III) salt is available in the reaction medium and as long as the stabilizing agents make more bonds with the particle surface than the solvent molecules, which will prevent the aggregation of particles. Therefore, the stabilizing agent has to have lone electron pairs to ensure binding to the surface of the GNP [63]. The potential stabilizing agents that fulfill the mentioned requirements could be chosen from the amino acids [64], polymers [65, 66], PEGs [67-71], and proteins [72-74]. The most popular methods to synthesize spherical GNPs are as follows:

Turkevich-Frens method

The most popular method to synthesize GNPs was introduced by Turkevich [75, 76] in 1951 and later modified by Frens in the 1970s [77]. This method consists of reducing of Au(III) in chloroauric acid ($HAuCl_4$) by a boiling solution of sodium citrate (60-80 ^oC) for one hour. The average particle size obtained with this method is 10-20 nm and the size can be controlled by varying the citrate/gold

ratio. In this method, sodium citrate acts as both a reducing and a stabilizing agent. Due to the non-covalent nature of the citrate-gold binding, the GNPs obtained by this method can be easily used as precursors for the synthesis of other GNPs and the binding can replaced by other molecules of interest, such as thiol groups [57, 78].

Brust method

In 1994, Brust and Schiffin introduced another method to make GNPs in solvents with reduced dispersity and controlled size [79, 80]. In this method, sodium borohydride is used as a reducing agent (reducing Au(III) to Au(I)) and tetraoctylammonium bromide (TOAB) acts a stabilizing agent. The reaction of the chloroauric acid with these two agents takes place in toluene. The average size obtained by this method is 5-6 nm. However, TOAB can be replaced by a stronger binding agent such as thiol to prevent the aggregation of the GNPs, which normally takes place over the course of two weeks and is the normal trend of the particles obtained by this method due to the weak binding of TOAB to the surface of the GNPs. The soft character of both Au and S allows strong binding between the gold and thiolated ligands. By shifting the ratio to thiol/Au, one can control the size of core nanoparticles. The larger ratio of thiol/Au leads into smaller core size with less polydispersity [Gamma 149, 152, 153].

Sodium borohydride reduction method

So far, this method is the fastest and easiest method of synthesizing GNPs. The method consists of reduction of $NaAuCl_4$ (gold salt) by sodium borohydride which is a very strong reducing agent, and can produce GNPs even at room temperature. The stabilizing agents that could be used in this method involves peptides [81] and proteins [82]. The particle size obtained by this method is between 4-25 nm.

Gold Nanoparticles in Cancer Diagnosis and Therapy

Cancer

Undoubtedly, cancer is one the leading causes of mortality in recent years. The International Agency for Research on Cancer (IARC) reports the expected growth rate of cancer worldwide to be 21.4 million new cancer cases per year by 2030. Cancer is characterized by an up-regulated and increased process of cell growth that leads to the formation of masses, the so called tumors [83]. Currently, more than a hundred types of cancer have been diagnosed, each being classified by the cells that are involved (http://www.cancerresearchuk.org/cancer-help/about-cancer/what-is-cancer/).

Before any type of cancer can be treated, a high-resolution image of the cancerous cells or tumors, which can define the location, size and shape of the cancerous tissue, is required. In many cases, after the cancerous tissue is surgically resected, residual cancer cells, which are often microscopic, can be left behind and increase the reoccurrence rate in the future. In many other cases, cancerous cells in their early stages and of microscopic size, and/or the hindrance by other organs, make it difficult for the current imaging technologies to target them. Therefore, many researchers have been looking for different technologies that can help detect the cancerous cells, tissues and tumors at the microscopic scale before or after the surgery, and can image them with high resolution and defined margins [84].

Cancer Targeting

As mentioned in previous sections, the targeting of cancer cells can be done using both passive and active routes. Overall, targeted therapy and imaging is based on exploiting the receptors that are overexpressed in cancer cells membrane. These receptors help us target the cancer cells by improving the selectivity and signal of the imaging techniques. A good example of cell membrane receptors are peptide receptors. Peptides are small chains of amino acids that are used for targeting

the membrane receptors expressed in tumors. Peptide targeting usually works by small peptides binding to specific receptors with high affinity. Some of the advantages of using peptides for targeting includes, but is not limited to, their small size and ease of preparation, resistance to degradation in harsh chemical or radiolabeling conditions, rapid clearance from blood, high tumor penetration, and low toxicity. The disadvantages of using peptides include their short biological half-life, and the required detailed knowledge of molecular engineering of synthetic peptides. To be more elaborate, peptides can be degraded by peptidases and proteases (enzymes that have a role in breaking down bigger molecules into smaller parts, i.e. breaking peptides into amino acids in this case) when administered in vivo [85].

Nuclear imaging modalities

The systematic use of radionuclides in medicine was initiated with the development of the cyclotron and nuclear reactors in 1930s. Nuclear Medicine was established due to the potential of producing several radioisotopes suitable for medical applications using cyclotrons [86]. Radiopharmaceuticals are drugs with some kind of radionuclides existing in their constitution. The radiolabeled nanoparticles used for cancer diagnostics and therapy is one type of radiopharmaceutical [87]. Radionuclides are atoms of unstable nucleus and excessive energy. A radionuclide releases this excess of energy by the radioactive decay of its nucleus leading to the emission of high energy particles such as alpha, beta, positron, and gamma rays. The half-life of a radionuclide ($T_{1/2}$) is a characteristic of each radionuclide and is defined as a time needed for the number of nuclei to reduce to half of the initial number. For cancer theranostics (therapy and diagnostics), the selected radionuclide should have the appropriate half-life along with the desired emitted radiation and/or particle [88-90].

Due to high ionizing energies and low tissue penetration, the α or β^- emitting radionuclides are used as therapeutic radiopharmaceuticals. An example of such a radiopharmaceutical is the first FDA-approved, α-emitting $^{223}RaCl_2$ for bone metastases therapy. However, γ or β^+ emitting radionuclides

are more suitable for the development of diagnostic radiopharmaceuticals to be used with PET or SPECT [91].

PET imaging is a nuclear medicine functional imaging technique that is used as an aid to the diagnosis of cancer. This imaging technique works with the use of β^+ emitting radiopharmaceuticals and is based on the detection of two photons of 511 KeV energies simultaneously. These photons are produced from the annihilation of the positrons and electrons in the medium. ^{18}F with a half-life of 110 minutes is the most common radionuclide used with PET. SPECT is another nuclear imaging technique that relies on the use of γ-emitting radionuclides with energies between 30-300 keV. ^{99m}Tc is the most used SPECT radionuclide [92].

^{64}Cu is specifically an isotope of interest for both radiotherapy and PET imaging due to favorable emission characteristic ($t_{1/2}$= 12.7 h, β^+ 17.4%, E_{max}= 0.656 MeV). The short positron range of this isotope compared to other positron emitters makes ^{64}Cu a better candidate for producing high-resolution images. In addition, its longer half-life is an advantage over other positron emitters (e.g. ^{18}F) for both imaging and therapy purposes, where longer circulation times are necessary to achieve optimal target uptake [93].

The development of a non-invasive imaging tool for monitoring the distribution of GNPs in vivo is critical for successful applications of GNPs in the progress of basic biology research as well as clinical research. Techniques of directly labeling GNPs with radioisotopes are currently available and this is usually done using γ-emitting radionuclides [94, 95]. However, this method requires binding linkers between GNPs and radionuclides, which can further alter the outer structure of the GNPs. This change may affect the radio-sensitization properties of the GNPs and alter the intracellular uptake and biodistribution of the radiolabeled GNPs compared to those that are not labeled. Additionally, the possible detachment of radioisotopes from GNPs may lead to erroneous estimations of GNP distributions considering that these detached isotopes are counted as GNPs [96, 97]. In order to utilize the highly sensitive nuclear medicine modalities, GNPs are often externally labeled (radiolabel) with radionuclides before patient administration and PET or SPECT in vivo

imaging is obtained. These external radiolabeling methods are not always stable which may lead to the dissociation (or separation) of radionuclides from the GNPs.

Nanomedicines

Nanotechnology is a wide filed involving engineering, physics, chemistry, biology, and medicine and includes designing, characterizing, producing and applying the nanoscale devices and systems. Nanoparticles have high particle numbers per mass and larger surface area comparing to microparticles that enhances their reactivity in chemical reactions [98-100]. Nanoparticles can be produced by the use of a large variety of other materials from inorganic metallic compounds to organic polymers [101]. Figure 43 shows some example of different types of nanoparticles.

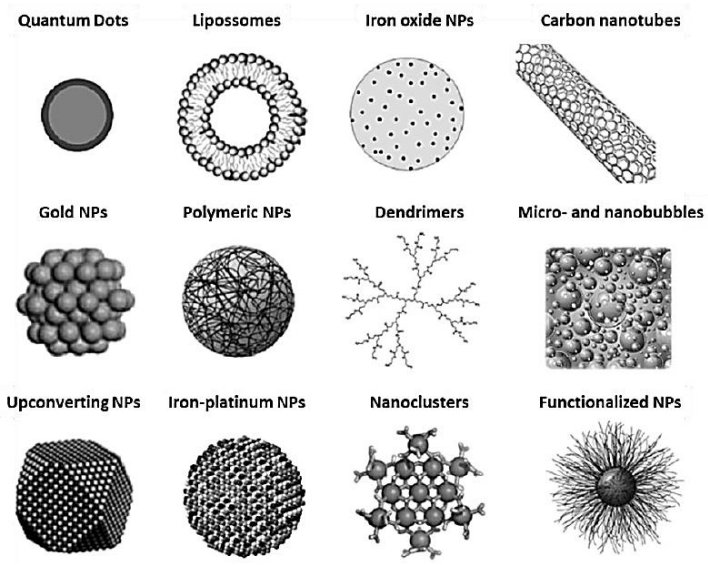

Figure 43. Examples of different types of nanoparticles for biomedical applications [102]

Nanomedicine is a field of science that utilizes nanoparticles or devices for monitoring, diagnosis, and treatment of diseases. The main applications of nanomedicine are for drug delivery, regenerative medicine, and in vitro and in vivo imaging. In vivo imaging includes MRI, ultrasound, optical imaging, PET, and SPECT [103, 104]. Compared to conventional drugs with adverse effects or lack of effects due to improper/insufficient dosage (e.g. chemotherapy drugs), nanomedicine

allow a more efficient drug accumulation at the target size due to their small size and ease of penetration into tissue barriers, leading to the reduction of the unwanted adverse effects and toxicity of the cancer drug [105, 106].

The integration of radionuclides in nanoparticles can happen either with conjugating the chelating agents to the core of nanoparticles for the coordination of radionuclides, or with encapsulating the radionuclides inside the nanoparticles. The stability of radionuclide incorporation is very important for nuclear imaging and therapy during the in vivo administration, otherwise, the imaging data will no longer reflect that of the nanoparticles [107] .

Some of the radiolabeled nanoparticles developed for nuclear imaging applications are presented in Table 5.

Table 5. Examples of radiopharmaceuticals and their application in imaging

Nanoparticle	Radionuclide	Imaging	Reference
Iron Oxide NPs	^{18}F	PET/CT	[108]
Quantum Dots	^{18}F	Multimodal	[109]
Quantum Dots	^{64}Cu	PET/NIRF	[110, 111]
Carbon NPs	^{111}In	SPECT	[112]

The advantage of using nanocarriers in cancer imaging is that they can increase the uptake of the agent due to passive targeting as well as the ability to conjugate nanocarriers to biological agents for active targeting. Figure 44 compares active and passive targeting using nanoparticles.

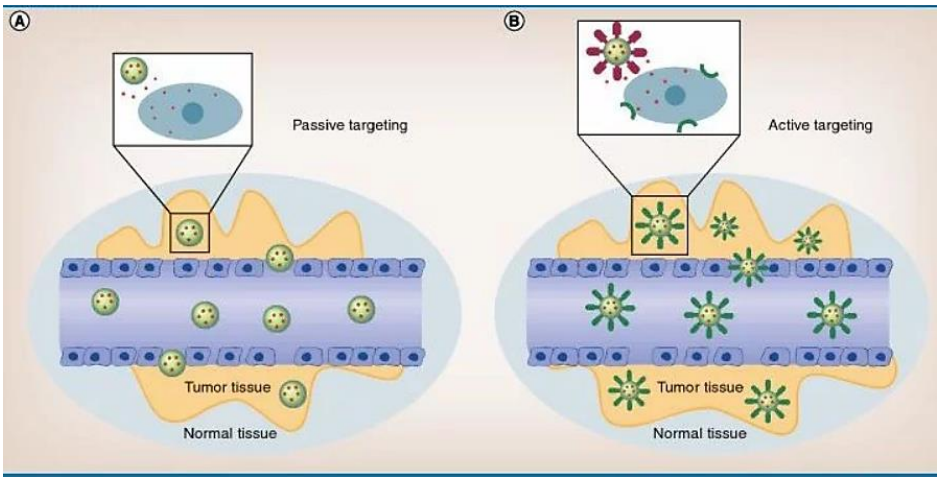

Figure 44. A: Passive targeting work based on "Enhanced Permeation and Retention" (EPR) effect, B: Active targeting works based on attaching the ligands that only bind to specific receptors on the cell surface as explained in Error! Reference source not found.**, taken after [[113]]**

GNPs in cancer theranostics

GNPs have been widely researched as pharmaceuticals for cancer theranostics (therapy and diagnosis). GNPs are biocompatible due to resistance to oxidation under physical and biological conditions. They also possess unique optical properties that can be controlled by their size and shape. Furthermore, they offer multiple functionalization with biomolecules for targeting tumor cells [57, 114]. All these properties make GNPs promising agents for cancer imaging and therapy. GNPs can be used as Computed Tomography (CT) contrast agents for cancer diagnosis since gold can absorb the X-ray energy at a higher ratio than its surrounding cells (approximately 100 times) due to its high atomic number [115]. Figure 45 shows the micro-CT scan of kidneys in a live mouse 60 minutes after injection of GNPs compared to iodine contrast agent [http://www.nanoprobes.com/newsletters/ImgGold.html].

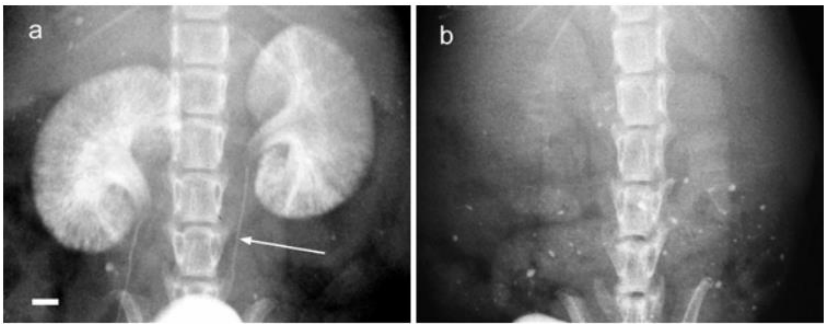

Figure 45. micro-CT scan of kidneys in a live mouse using a) gold nanoparticles, and b) iodine contrast agent (*Omnipaque H*) as contrast agent [*http://www.nanoprobes.com/newsletters/ImgGold.html*]

Besides imaging modalities, GNPs are applied as therapeutic agents. GNPs are good candidate sensitizers for radiation therapy. After GNPs are bombarded with radiotherapy beams, they interact with the radiotherapy primary beams resulting in the cascades of secondary radiation (i.e. electrons). The secondary radiation produced by this interaction provides radio-sensitization for cancer cells that are impregnated with GNPs. The concept behind using GNPs as the radiosensitizing agents well be discussed in more detail in the next section.

Another application of GNPs as therapeutic agents is for photothermal therapy. GNPs can reach temperatures of 70- 80 ^{o}C when irradiated by laser pulses with appropriate wavelength leading to the destruction the cancer cells [116, 117].

Besides imaging modalities and therapeutic applications, GNPs can also be conjugated with various chemo drug molecules for targeting specific tumor cells [118-125]. For example, GNPs have been used as a carrier of the cytotoxic drugs such as doxorubicin (a bacterial antibiotic that is widely used to treat leukemia and various other forms of cancer). When used as drug delivery platform, GNPs can enhance the cytotoxicity of the molecules they are carrying by shielding the drug and avoiding its degradation in the healthy tissues, the so called “bioavailability” effect [126, 127].

So far, three generations of GNPs have been developed for cancer theranostics. The first generation are the GNPs produced based on basic surface chemistry. The second generation of GNPs are the ones that are coated with polyethylene glycol (PEG) exhibiting improved stability and optimized surface chemistry. This generation allows the passive targeting through the EPR effect. The third generation corresponds to the GNPs modified by bioconjugation such as peptides for active targeting [128, 129]. Figure 46 shows the schematic of these three generations.

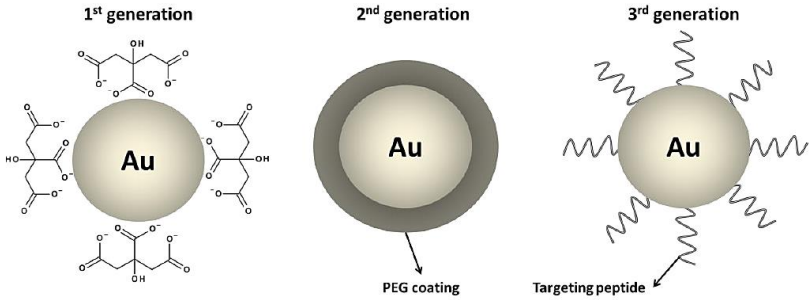

Figure 46. Schematic of the three generations of GNPs (taken after [61])

GNPs as radiosensitizers

Radiotherapy is a commonly used treatment with application rate as high as 80-90% for several types of cancers such as breast cancer[130, 131]. In a radiosensitization process, radiosensitizers present at the tumor location interact with irradiation dose and/or the biological targets to enhance the effect of radiotherapy via physical, chemical, and biological mechanisms. GNPs have been known as potent radiosensitizers due to their exceptional physical and chemical properties [131-133].

The physical basis of GNPs radiosensitization come from the fact that metal-based nanoparticles such as GNPs, with high Z, enhance the contrast between tumor and soft issues, thus decreasing side effects compared to radiotherapy alone [134].

The physical interactions between radiation and nanoparticles happen through three mechanisms: 1) photoelectric effect usually followed by Auger cascades, 2) Compton effect, and 3) pair production. The photoelectric effect dominates at lower energies of the incident photon (10-500

keV), leading to the ejection of an electron from the inner atomic orbitals. The vacant orbit is filled by an outer shell electron with high energy, causing the release of low-energy photons that in turn release secondary electrons (Auger cascade). This process has the major contribution in causing ionizing events. The photoelectric absorption cross-section is proportional to Z^{3-5}. Therefore, materials with higher Z, such as gold, have higher mass energy absorption coefficient compared to materials with low Z. The absorbed radiation energy is released locally by the emission of photons and secondary electrons causing damage to biological components around them [84, 135].

Biological Properties

Toxicity

GNPs have been widely examined for in vitro and in vivo biocompatibility [136-139]. The toxicity of GNPs depends on their shape, size, surface charge and surface coating but the general toxicity of GNPs is in an acceptable level [140-144]. However, since anything can be toxic at high-enough doses, we need to examine thoroughly how toxic our synthesized GNPs are at the concentrations they might be possibly used in future. Hence, it is mandatory to evaluate the cell viability and cytotoxicity of ^{64}Cu@Au GNPs by investigating their effects in human cells. The toxicity of GNPs can be shown with half-maximal inhibitory concentration (IC_{50}) which is a quantitative measure that indicates how much of GNPs is needed to inhibit a given biological process or biological component (i.e. cells viability) by 50%.

Biodistribution

The biodistribution information will allow us to administer the radiotherapy with a pre-knowledge of the clearance characteristic of our material.

Pharmocokinetics

Pharmacokinetics (PK) data are useful for gaining insight into the clearance of drug from the blood. PK studies is the type of study describing the time course and factors affecting the handling of drugs by the body until its complete elimination [145]. In other words, by PK analysis, we can extract information regarding what the body does to the drugs by calculating the rate of drug absorption (entry into blood circulation), distribution (dispersion or dissemination in fluids and liquids), metabolism (irreversible decomposition into daughter metabolites), and excretion (elimination of the substances from the body). A typical PK graph relates the time course of administration to the drug concentration in the body.

There are several models for PK analysis. We will be using the simplest model (one compartment model) throughout this dissertation. This model uses the following equation to give a concentration (amount per volume) as a function of time.

$$C = C_{max} e^{-\lambda t} \tag{0.1}$$

where C is the concentration, C_{max}, λ is the elimination rate constant, and t is time.

Figure 47 Shows an example of a PK graph when the drug is injected in the body by intravenous (iv) route.

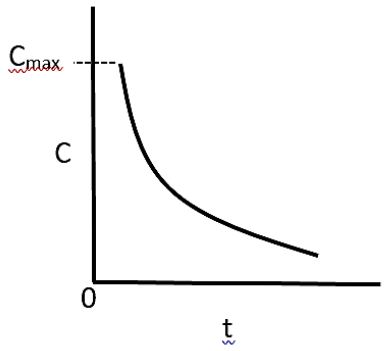

Figure 47. Schematic of an expected PK graph

Objective of this study

We were motivated to develop hybrid GNPs with radiosensitizing and PET/SPECT imaging capabilities. The hybrid NPs we developed have a core-shell structure with the majority of material (> 95%) being gold. The core is made of Cu, which was then covered with an Au (gold) shell.

The hybrid GNPs have the potential as image-ready GNPs. When GNPs first commercially became available, they were provided as bare GNPs. Due to their increasing popularity in biological and medical applications, most companies now provide them as PEGylated-GNPs with linkers. When doped with radionuclides, the core changes to positron emitters, which allows for imaging using PET.

In the following chapters, we first report the development and characterization of non-radioactive GNPs confirmed by TEM, UV-vis and ICP. Our hybrid GNPs were functionalized with varying amounts of c-Met binding peptide (cMBP) to specifically target Mesenchymal-epithelial transition factor (c-Met). c-Met is a receptor that is expressed in many human cancer cells such as the A549 human lung cancer cells. Later, we produced radioactive hybrid GNPs by doping them with ^{64}Cu and evaluate their binding properties in cell binding studies.

Simultaneously, GNPs were traced by Gamma detection. The radioactive hybrid GNPs were then injected into animals for studying their biodistribution and pharmacokinetics.

The radiolabeled hybrid GNPs are inherently radioactive, therefore, there is no risk of detached radiolabels being counted erroneously. Since our hybrid Cu@Au GNPs (in which the shells are gold) have identical outer structures to that of regular GNPs, the existing GNP targeting and nano-carrier methodologies can be utilized. This allows an easy transition of the technology into basic science investigation and possible clinical practice.

CHAPTER X

MATERIALS AND METHODS

Synthesis of core-shell Cu:Au GNPs

The procedure of synthesis we used is the modification to the synthesis process used by Zhang et al. [146]. Briefly, aqueous solutions of $CuSO_4$ and sodium citrate were added to 20 ml of water at $12 \pm 2\,^{o}C$ while stirring at 1,000 rpm. Then 1 mL of freshly prepared $NaBH_4$ solution was rapidly added to the reaction mixture. After 15 min, $HAuCl_4$ solution was added to the reaction mixture and continued stirring for another 20 minutes. The optimized conditions for the formation of Cu@Au GNPs are shown in Table 6. The final product had a red-wine color as shown in Figure 48. Next, the final product was treated by size-exclusion chromatography (also known as gel filtration) to remove the excess salts and unreacted molecules. In the final step, the GNPs were functionalized with PEG only or with PEG and cMBP peptide for targeting purposes.

Table 6. Optimized condition for the formation of unfunctionalized Cu@Au GNPs

Chemical	Molarity (M)	Volume
Water		20 ml
$CuSO_4$	0.1	50 µl
Sodium citrate	0.1	150 µl
$NaBH_4$	0.025	2 ml
$HAuCl_4$	0.1	150 µl

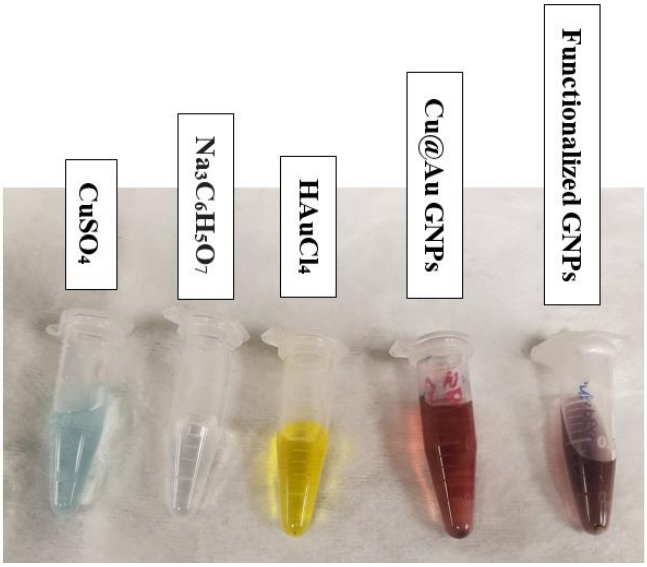

Figure 48. The reagents and final products in synthesis GNPs

Peptide synthesis

As discussed earlier, peptides are being used for in vivo cancer detection due to their ability to increase the tissue-specific uptake. The c-Met is overexpressed by many cancer cells such as lung, breast, prostate, head and neck, ovarian, renal, melanoma and many more [147-150]. The following steps show the synthesis procedure for functionalizing the GNPs.

1. The cMBP, Lys-Ser-Leu-Ser-Arg-His-Asp-His-Ile-His-His-His, identified from a phage display of a combinatorial peptide library by Kim et al. (2007) was used as a c-Met targeting vector to functionalize our novel ^{64}Cu doped hybrid Cu@Au GNPs [151].
2. The c-Met binding peptide conjugate, cMBP-$(PEG_2)_3$-Cys-NH_2, was synthesized on an in-house built peptide synthesizer [152]. The peptide conjugate was purified by HPLC and characterized by matrix-assisted laser desorption/ionization (MALDI) mass spectrometry. Figure 49 shows the MALDI -mass spectrum of the cMBP-$(PEG_2)_3$-Cys-NH_2 performed at OUHSC core facility.

3. In the final step, our hybrid Cu@Au GNPs were functionalized with varying amounts of cMBP to specifically target c-Met. The schematic is drawn in Figure 50.

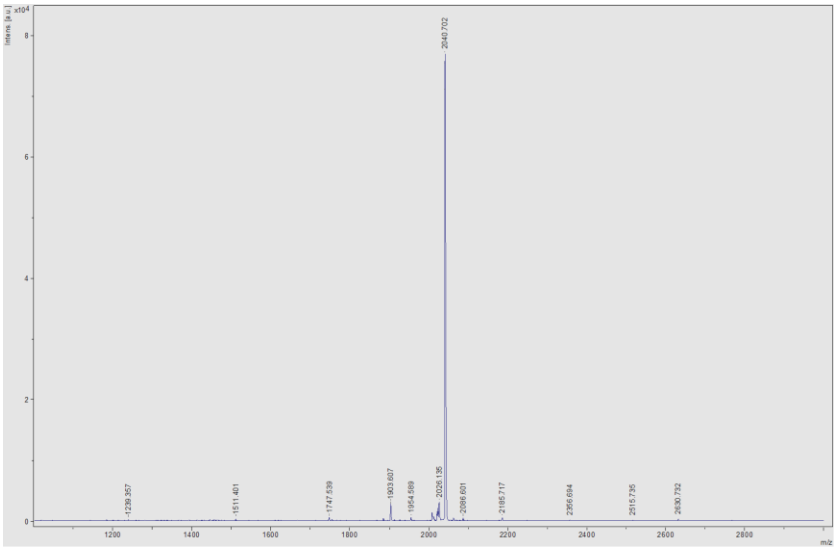

Figure 49. MALDI mass spectrum of cMBP-(PEG2)3-Cys-NH2 (MW – 2,040.7)

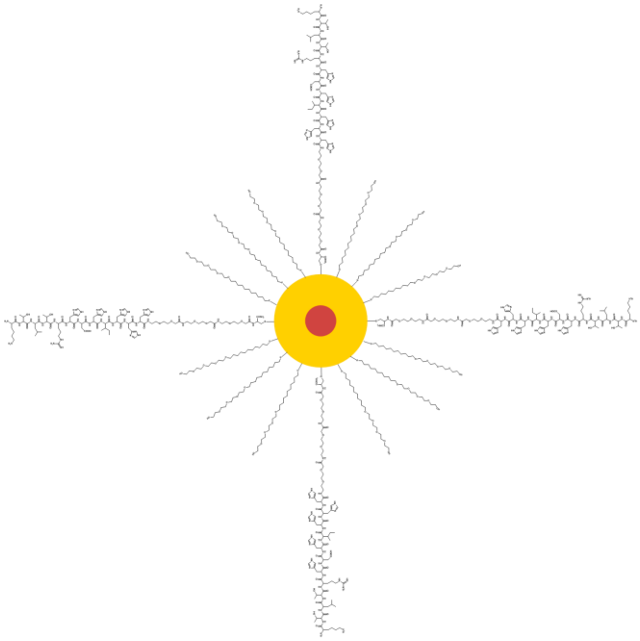

Figure 50. Schematic of Cu@Au GNPs functionalized with cMBP to target c-Met

Radiolabeling

All experiments involving radioactivity were performed after thorough planning and a dry run, in compliance with the regulation of OUHSC and ALARA (as low as reasonably achievable) radiation-protection principle. ^{64}Cu was purchased from Washington University School of Medicine cyclotron facility. The radiolabeling process was carried out in a lead-shielded fume hood. The synthesis procedure was the same as that reported in section 0 with the addition of ^{64}Cu-chloride aqueous solution according to the activity needed for each experiment.

Material Characterization

The following sections will review some basic principles of the characterization techniques used in this study.

Ultraviolet-Visible Spectroscopy

Ultraviolet-Visible Spectroscopy (UV-vis spectroscopy) is a commonly used technique to characterize GNPs. UV-vis spectroscopy is a reliable technique to study and identify GNPs since GNPs inherit optical properties that vary with their size, shape, concentration, and the index of refraction near their surface. The optical absorbance peak of the GNPs was measured using a Cary 5000 UV-Vis-NIR spectrophotometer (model Cary 5000, Varian).

The color transitions in GNPs is correlated to the size or the thickness of a shell in a core-shell structure. Most of these transitions occur in the visible portion of the spectrum and can provide information about the size and the morphology of the particles [153].

Transmission electron microscopy (TEM)

Transmission electron microscopy (TEM) is a more advanced technique to determine the size, shape and arrangement of GNPs that allows direct imaging of the particles. In a typical TEM measurement, a focused beam of electrons is transmitted through the sample leading to the formation of an image in a similar way to a light microscope. The samples were prepared by

dropping 2 µl of GNPs onto a carbon-coated copper grid and letting them air dry for 4 minutes. The grid was then mounted in the instrument (JEOL, JEM 2100). The images of the nanoparticles were obtained with different zooming modalities of the instrument. The light areas of the TEM images indicate the parts of the grid where that material is less dense and therefore more electrons have passed through.

TEM/EDS

Further studies were performed with the intention of getting more information regarding the core/shell structure of the Cu@Au GNPs by combining TEM with Energy Dispersive X-ray Spectroscopy (EDS). EDS is a spectroscopic technique that offers information on the elemental composition of a nano-sized area [61]. Both TEM and TEM/EDS measurements were carried on at the OSU electron microscopy laboratory.

Inductively Coupled Plasma atomic emission spectroscopy (ICP)

ICP is the best technique for quantifying the metals present in GNPs. ICP can detect metals like Au and Cu over a wide range of concentrations. ICP measurements were performed at OSU soil, water and forage analytical lab by using Spectro Arcos.

X-ray Photoelectron Microscopy (XPS)

XPS can provide information about the nature of Au bonds as well as surface analysis. In a typical XPS measurement, the samples are irradiated with mono-energetic X-rays leading to photoelectrons emitted from the surface. An energy analyzer is used to detect these photoelectrons to determine their binding energy and the respective intensity [http://www.casaxps.com/help_manual/manual_updates/xps_spectra.pdf]. The XPS samples were prepared by dropping the material on cleaned silicon wafers and allowing them to dry in air.

In vitro studies

Cell binding studies

In vitro cell binding studies were performed to determine the binding affinity of cMBP-GNPs to c-MET expressing cells and optimal mount of peptide functionalization. In the first method, different peptide-functionalized (0%, 1%, 3%, 5%, 10% functionalization of the estimated Au atoms present on the surface) nonradioactive GNPs and the A-549 cells (1×10^6 cells/well) were incubated in 6-well plate. After 45 minutes, the cells were washed with PBS three times to remove the residual GNPs that are not taken by the cells. Then, the cells were digested with NaOH(0.1M)/SDS(0.1%) and collected and submitted for ICP measurement to determine the Au/Cu concentrations. Due to the insignificant results, the whole experiment was repeated for 1 h and 4 h incubation time.

In the second method, the same procedure was followed with radiolabeled GNPs. The same concentration of peptide (0%, 1%, 3%, 5%, 10%) was bound to the radiolabeled ^{64}Cu@Au GNPs. An activity of 1 μCi was added to each well. The cells were incubated for 2 h before measuring the cell-bound activity using a gamma counter. The result is reported in section 0.

Cytotoxicity

A-549 cells were seeded in a 96-well plate at 3×10^3 cells per well. The cells were then cultured in a standard condition in an incubator for 24 h. Different concentrations of Cu@Au GNPs (1,000, 750, 500, 250, 100, 50, 25 μg/ml diluted in RPMI medium) were then added to the wells, and the cells incubated for 48 h. After that, MTT was added to each well. Finally, a plate reader (Synergy 2, BioTec) was used to evaluate the in vitro cell viability/toxicity profile.

An MTT (reagent 3-(4,5-dimethylthiazole-2-yl)-2,5-diphenyl tetrazolium bromide (Alpha-Aesar) 5 mg/ml in PBS) was used for MTT assay. The MTT assay determines cell viability by measuring the activity of living cells via mitochondrial dehydrogenases. Unlike traditional methods, which evaluate toxicity based on dye uptake in treated non-viable cells, this method provides greater sensitivity and

accuracy. The viability of the control cells was considered 100%, with treated cell viability expressed relative to the control.

In a typical NP cytotoxicity experiment, 20 µl of MTT is added to each well, following by a rest time of 2 h to let the cells absorb the MTT. The live cells then turn the yellow color of MTT to blue. The cells are digested in 100 µl of Dimethyl sulfoxide (DMSO)/well and the optical density is read at 570 nm to record the viability. However, for the GNPs we developed, we could not use the typical method since the color of GNPs are red and this makes it difficult to see the optical absorbance. Instead of adding MTT to the wells, first we had to empty the GNPs and medium from the top of each well carefully. For that purpose, we used a vacuum pipe that was installed in the cell culture fume hood. We used extra caution not to vacuum the cells from the well. Then, 20 µl of MTT diluted in 100 µl of medium was added to each well and the plate reading was followed. The result was used to calculate IC_{50} as shown in section 0.

In vivo Studies

All animal studies were carried on following the protocol approved by (Institutional Animal Care and Use Committee (IACUC)). We performed the biodistibution studies using a mice model and pharmacokinetics on a rat model, as described in the following sections.

Biodistribution

A preliminary biodistribution study was performed to investigate what organ/organ-systems are responsible for clearance of ^{64}Cu@Au GNPs from the blood. For this purpose, healthy CD-1 mice were used. Different doses of ^{64}Cu@Au GNPs were injected into the tail vein of the mice under isoflurane anesthesia. For each data collection time, four mice were injected and the injection dose was different for each data time: 1h (10 µCi/mouse), 4h (15 µCi/mouse), 24 h (50 µCi/mouse) and 48h (100 µCi/mouse) (n=4 mice/timepoint; Total=16). At each time point after injection, mice were euthanized by cervical dislocation and various organs were collected to determine the activity

present in the tissue (using a well-counter). The activity was normalized to the weight of the tissue and presented as the percentage of the injected dose per gram of tissue and subsequently as the percentage of injected dose per organ.

Pharmocokinetics

In order to determine the pharmacokinetics of ^{64}Cu@Au GNPs, male Sprague Dawley rats were used. Rats of 200-225 g weight have optimal size for the installation of indwelling femoral artery catheter. This catheter can be used to sample blood at intervals to determine the clearance rate of ^{64}Cu@Au GNPs. 7 rats were injected with different amount of ^{64}Cu@Au GNPs while the injection dose was kept the same ~ 40 μCi for all injections. In order to have a good statistical data, 3 rats were injected with 5X (X= concentration of GNPs) and 4 rats were injected with 3X. The sampled blood of 7 rats were collected according to the following volume and time points: 0.1 ml at 2 min, 5 min, 10 min, 20 min, 30 min, 1 h, 2 h, 4 h , 6 h, 0.3 ml at 24 h, 0.6 ml at 28 h and 48 h. The sampled blood was the counted by a gamma counter (Ludlum Measurements Inc., Model 2200 Scaler Ratemeter). The activity was then corrected for decay based on the standard counts and for the volume of withdrawn blood. The result is reported in counts per minute per μL.

CHAPTER XI

RESULTS AND DISCUSSIONS

Synthesis and Characterization of Cu@Au GNPs

Based on optimum condition listed in Table 6 we synthesized the GNPs. The characterization results are as the following. Figure 51 shows the UV-Vis spectra of three different samples. The absorbance peak appeared around 526 nm, which is the typical absorbance peak of gold. We observed that upon addition of $HAuCl_4$, the solution turned wine red instantly. These results are in line with the results obtained by Zhang et al. As suggested by them, during the synthesis, the galvanic displacement reaction between $HAuCl_4$ and Cu nanoparticles takes place following by reduction of $HAuCl_4$ by the remaining $NaBH_4$ after generation of Cu NPs. They also observed the same color change (the solution turning wine red immediately) upon the addition of $HAuCl_4$, indicating a prompt growth of Au shell onto the Cu NPs core. In addition, they further more investigated that the absorbance of $HAuCl_4$ centered at 218 and 293 nm disappeared after the reaction, and a new absorbance band emerged at 520 nm which is the feature of gold surface Plasmon resonance SPR. In their experiment, after 24 h the new gold SPR band was extended to 530 nm and became a little more intense displaying a quick growth of Au shell onto the Cu NPs core. This could be an indicator of a complete transformation of $AuCl_4$ to clusters of Au atoms, with an average size above 2 nm that confirms the color of our synthesized Cu@Au GNPs and the UV-Vis spectra we obtained within the 24 h of synthesis [146] .

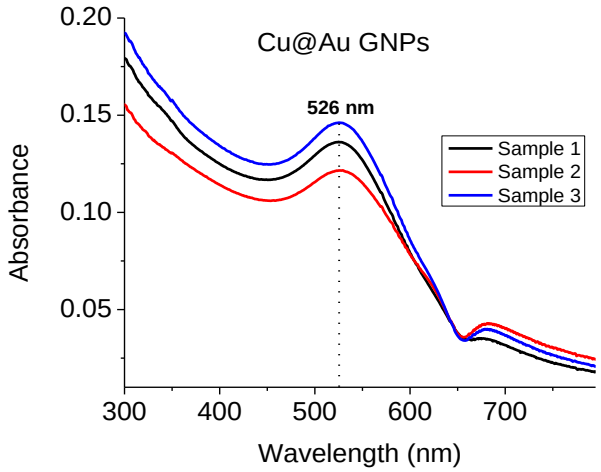

Figure 51. Absorbance peak of Au around 526 nm confirmed by UV-Vis spectrometer for different samples

TEM measurement was performed to assist the understanding of the shape, size and the distribution of both stable GNPs and the radiolabeled GNPs after the complete decay of ^{64}Cu. The Cu@Au GNPs 2 h post synthesis were more irregular in geometry and more separated with average size smaller than 10 nm (Figure 52 a, b). After 24 h, more regular, spherical particles occurred, with a clustered distribution (Figure 52 c, d).

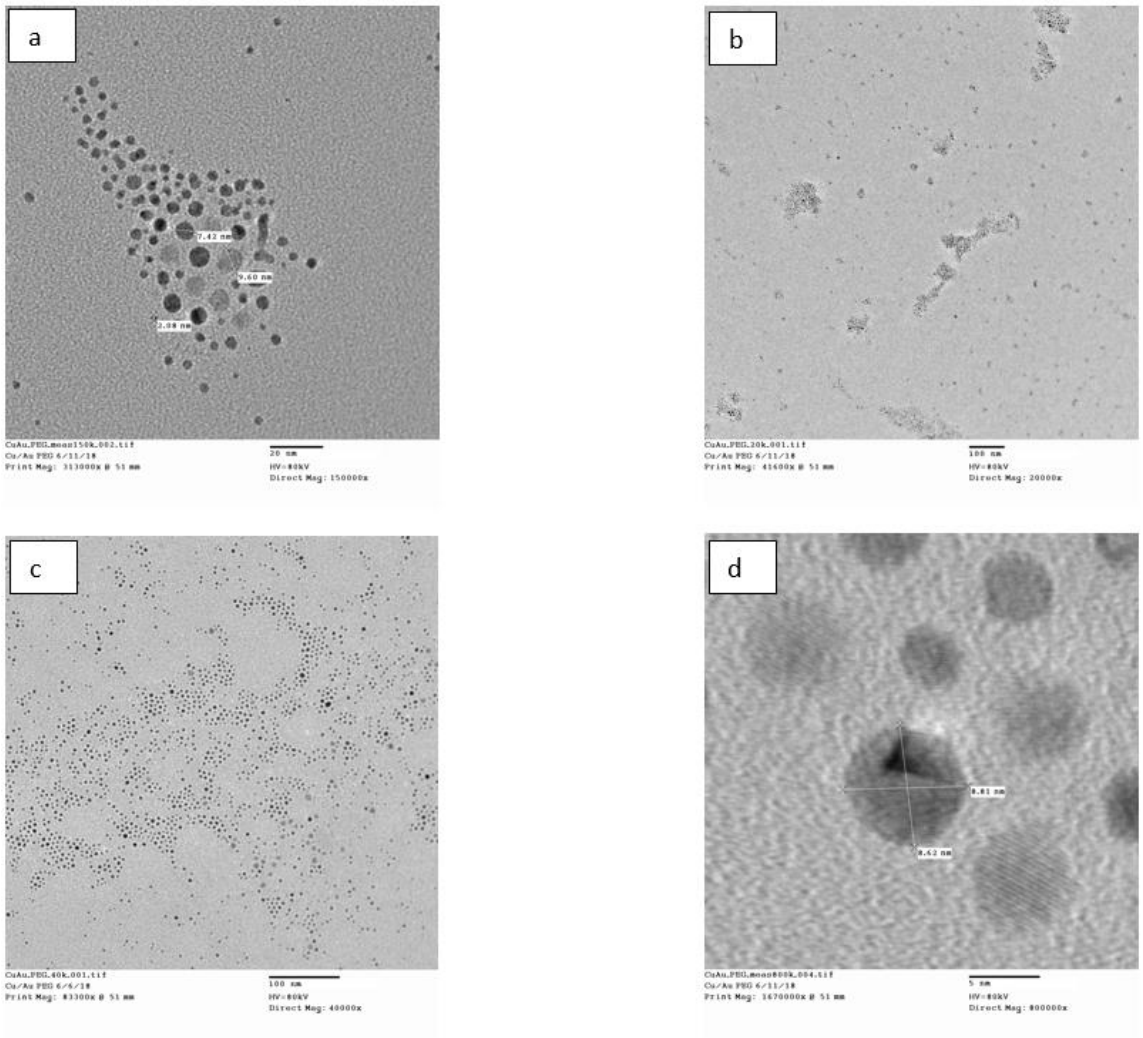

Figure 52. a) TEM on GNPs after 2 h, magnification: 150K. b) Distribution of GNPs after 2 h, magnification: 20K. c) Distribution of GNPs after 24 h, magnification: 40K . d) GNPs showing spherical shape after 24 h, magnification: 800K.

The radiolabeled ^{64}Cu@Au GNPs shows the same average size, distribution and morphology as the stable Cu@Au GNPs as shown in Figure 53.

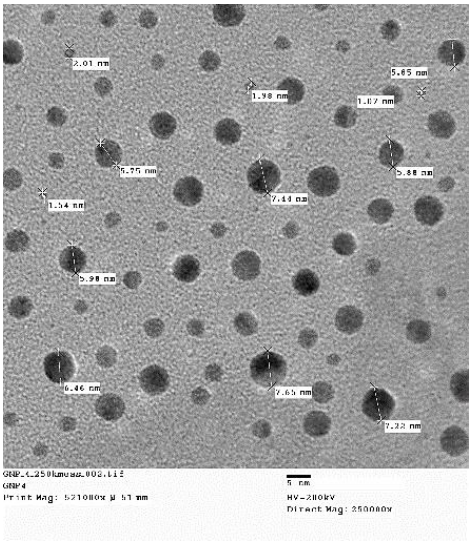

Figure 53. TEM on the radiolabeled GNPs after decay. Average size is less than 10 nm, magnification: 250K

We performed TEM/EDS (energy dispersive X-ray spectroscopy) analysis on different parts of the grit to obtain more detailed information about the copper and gold distribution in the sample. To reduce the effect of the presence of Cu in parts of the electron microscope and in the grits, we used Ni grit and the background was subtracted (a value typically found on empty grits and on areas not containing particles). Also, due to the small size of particles (< 10 nm), and the limitations in the magnification of our device, we were not able to take the measurement from one particle only. Therefore, the reported quantities is only from a micrometer-sized areas of the grit containing several particles rather than just one particle. The TEM/EDS spectrum from a partial region of Cu@Au GNP sample is shown in Figure 54. The result showed the presence of X-ray dispersion energy peaks characteristic of gold (Au(M) ≈ 2.120 keV, Au(Lα) ≈ 9.712 keV), as well as less intense characteristic X-ray dispersion energy peaks of copper (Cu(Lα) ≈ 1.00 keV, Cu(Kα) ≈ 8.00 keV). These results are similar to the results of EDS analysis of nanoparticles containing Au and Cu reported in the literature [61, 154, 155].

a) b)

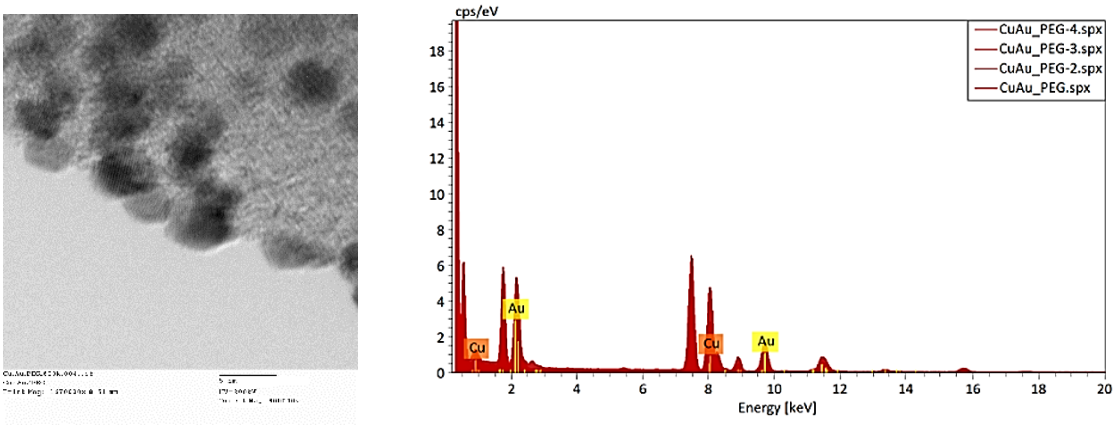

Figure 54. a) TEM and b) EDS analysis of Cu@Au GNPs on a micrometer sized areas of a nickel grit

The values of Au and Cu present in the micrometer-sized area of the grit was measured several times from different parts of the grit and the average is shown in the following Table.

Table 7. The average percentage of Au and Cu present in the microemeter sized area of the grit

Cu@Au GNPs/PEG	Gold	Copper
Average	23.57 %	76.43 %

The XPS analysis can be used to confirm the core/shell structure of GNPs with a good approximation. As seen in Figure 55a, Au 4f7/2 XPS spectrum exhibited a binding energy (EB) at 84.3 eV with a well-separated spin-orbit components (Δ=3.7eV), consistent with metallic gold atom binding energy (Au^0, E_B=84.0 eV). The shift of binding energy for Au 4f7/2 when compared to that of zero-valance gold atom(84.0 eV), could be due to an electronic modification of the Au atoms by Cu NPs [146, 156]. Figure 55b shows that the EB for Cu $2p_{3/2}$ XPS was located at 933.3 eV. Cu2p peak has a significant spin-orbit split components (Δ=19.75eV) which is consistent with Cu^0 and Cu(I) oxide (E_B=933.0 eV). This observation shows that majority of Au and Cu present in the nanoparticles are in their zero valence state [157]. The database used to compare the binding energies are taken from *https://xpssimplified.com/periodictable.php.*

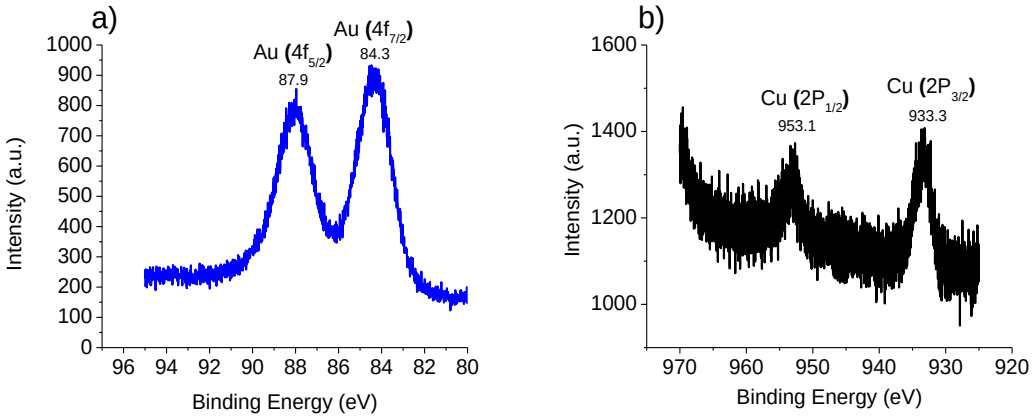

Figure 55. XPS spectra for a) Au 4f, and b) Cu 2p in Cu@Au GNPs

Table 8 represents the ICP result for several samples used in this study. The ratio of Au/Cu is in the range of 7.6- 11.5. In addition, based on the numeric result obtained from ICP, more than 50% of the initial Au and more than 90% of the initial Cu was used in the reaction. This result is solely based on the assumption that Au atoms are all in the shell and by calculating the approximate number of Au atoms on the surface from the average particle size and the atomic radius of gold.

Table 8. ICP results of variety of samples used in this study

Material	Au (ppm)	Cu (ppm)	Au (µg/ml)	Cu (µg/ml)	Au/Cu ratio
GNP before passing through size-exclusion column	11.60	1.53	116.0	15.3	7.6
Colored GNP after passing through size-exclusion column	3.76	0.42	37.6	4.2	9.0
GNP used for PK studies, 5X concentration	4.06	0.38	13.5	1.3	10.8
GNP used for PK studies, 3X concentration	8.27	0.82	82.7	8.2	10.1
GNP used for cytotoxicity	11.96	1.04	1495.1	129.5	11.5
GNP evaporated and filtered for targeting	14.18	1.49	1418.0	148.7	9.5

In vitro studies

The result of ICP for digested cells after 1 h and 4 h incubation with functionalized GNPs did not show any significant trace of Au and Cu that is the indicator that no uptake was taken place. This can be due to several factors ruling the cell uptake. Among all reasons, the most trivial ones are peptides not binding to the GNPs, and c-Met expression not being well defined on the A549 cells. However, due to the lack of time and the expertise of the author in the field, we decided to continue

the rest of the studies with unfunctionalized GNPs. Targeting the cells with radiolabeled GNPs did not give us any meaningful result as for the cell uptake either.

Cytotoxicity

Figure 56 shows the effect of Cu@Au GNPs on A-549 cell viability. IC_{50} is the concentration at which viability equals to 50% of maximal viability. The 50% of maximal viability was calculated as maximal viability- 50% (maximal viability- minimal viability) [158]. The IC_{50} of our hybrid Cu@Au GNPs was found to be 807.2 ± 0.05 μg/ml. This result is within the range reported in literature (i.e. 500 - 1,200 μg/ml) based on the NPs size (<15 nm)for different cell types [159, 160]. However the IC_{50} reported in literature for bigger GNPs (50-90 nm) are between 15-20 μg/ml [161]

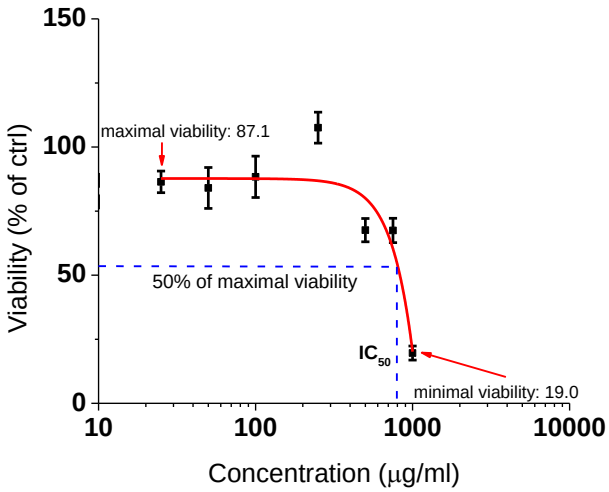

Figure 56. The cell viability was measured by MTT assay. Each point represents the mean viability of 6 wells. The viability was calculated as the percentage of the viable cells compared to the untreated control cells.

Biodistribution

The uptake and the clearance of the ^{64}Cu-labeled Cu@Au GNPs were determined through biodistribution studies. The data for various organs uptake at 1 h, 4 h, 24 h, and 48 h post injection are shown in Figure 57. The highest accumulation of radioactivity at all times were found in the liver and the intestine indicating that the ^{64}Cu@Au GNPs are primarily clearing from the blood

pool via hepatobiliary pathway. The clearance of the ^{64}Cu@Au GNPs through the kidneys in the bladder/urine was found to be low. A negligible uptake of ^{64}Cu@Au GNPs was observed in brain and spleen. With the exception of muscles, bladder and spleen, all organs showed an increase in ^{64}Cu@Au GNPs accumulation between 1- 4 h and the radioactivity accumulation started to decrease 4 h post injection. This observation in some organs (uptake of 1 h is less than of 4 h) is in contrary with the usual uptake of free ^{64}Cu reported in several publications stating a steady decrease in the uptake of ^{64}Cu [93, 162, 163]. To know the reason for this behavior of ^{64}Cu@Au GNPs requires more in vivo studies. The uptake of ^{64}Cu@Au GNPs in the muscle is most likely due to the blood-associated radioactivity. Collectively, this data indicates that our ^{64}Cu@Au GNPs may find potential application in the treatment of the tumors located in the breasts when GNPs are appropriately functionalized to target those tumors.

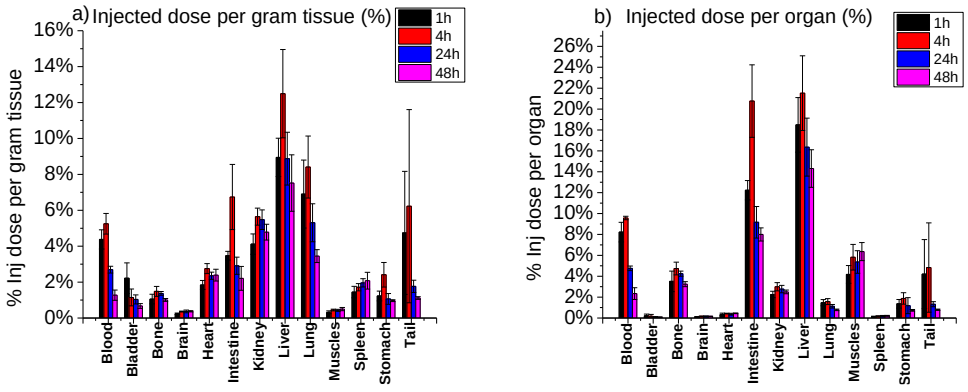

Figure 57. Biodistribution of 64Cu@Au GNPs in mice, n=4 for each time point a) percentage of injected dose per gram tissue b) percentage of injected dose per organ

Pharmacokinetics

The rats were randomly divided into two groups of 3 and 4. Three rats were injected with 5X concentration of ^{64}Cu@Au GNPs and four rats were injected with 3X concentration of ^{64}Cu@Au GNPs. The pharmacokinetics were calculated based on average data for each group. The pharmacokinetic data measured included the area under the concentration–time curves from time

zero to infinity ($AUC_{0-\infty}$), and the area under the first moment curve (AUMC). Maximum GNP concentration (C_{max}) was taken directly from the concentration-time plot. The Mean Residence Time (MRT) is the average time that the GNPs remain in the body and was determined by dividing AUMC by AUC. The Total Clearance (Cl) value was calculated as the dose/$AUC_{0-\infty}$. The average decay-corrected injected dose is 40 μCi. In addition, the volume of distribution at a steady-state (Vss) was calculated as MRT×Cl, and the apparent elimination rate constant ($kel^{'}$) was calculated as 1/MRT. Finally, elimination half-life ($t_{1/2}$) is defined as the amount of time required for the amount of drug in the body to decrease by 50% and was calculated as $t_{1/2}$= 0.693/ $kel^{'}$.

The concentration-time curves are shown in Figure 58.

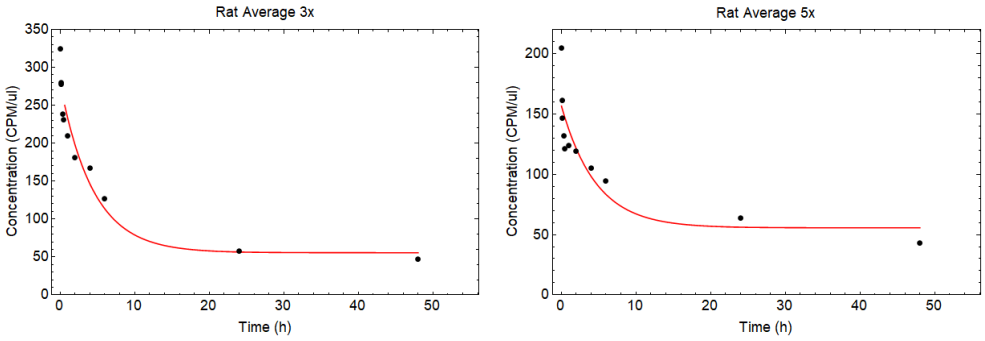

Figure 58. The concentration vs. time curves for the average data for two different concentration of radiolabeled GNPs with constant activity. Red curves show the fitted curves.

The $AUC_{0-\infty}$ was calculated using the AUC_{0-last} and then extrapolating to infinity by the addition of $AUC_{last-\infty}$ as shown in equation below. The graph from which AUC_{0-last} (total AUC) is calculated is presented in Figure 60.

$$\boldsymbol{AUC_{0-\infty} = AUC_{0-last} + \frac{C_{last}}{\lambda}} \qquad \textbf{(0.1)}$$

where λ is the terminal slope from semi-log concentration-time graph as seen in Figure 59.

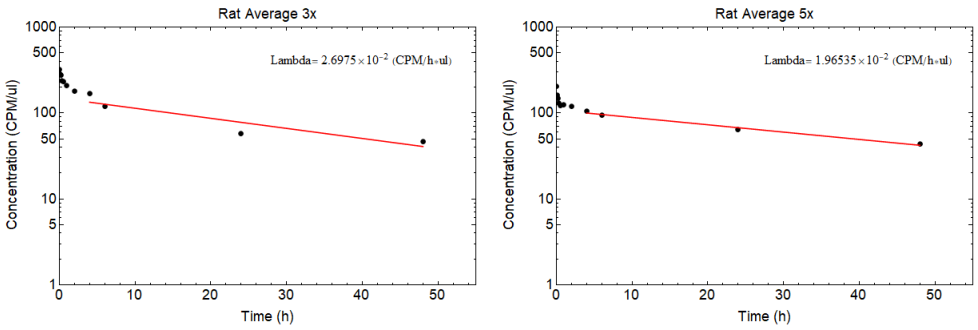

Figure 59. The semi-log plot of concentration-time to find the terminal slope

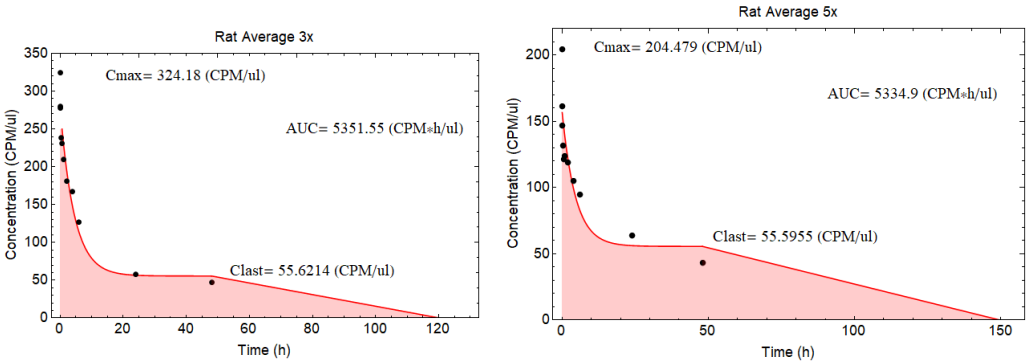

Figure 60. Total AUC (AUC_{0-last}) represented by pink area after the fitted curve was extrapolated to infinity using λ.

Figure 61 represents the first moment of the data, i.e. the area under the "concentration*time- time" curve (AUMC) and the fitted plot. The method to extrapolate the curve is according to the following equation and the representation of it is shown in Figure 62 (pink area).

$$AUMC_{0-\infty} = AUMC_{0-last} + \frac{C_{last} \cdot t_{last}}{\lambda} + \frac{C_{last}}{\lambda^2} \qquad (0.2)$$

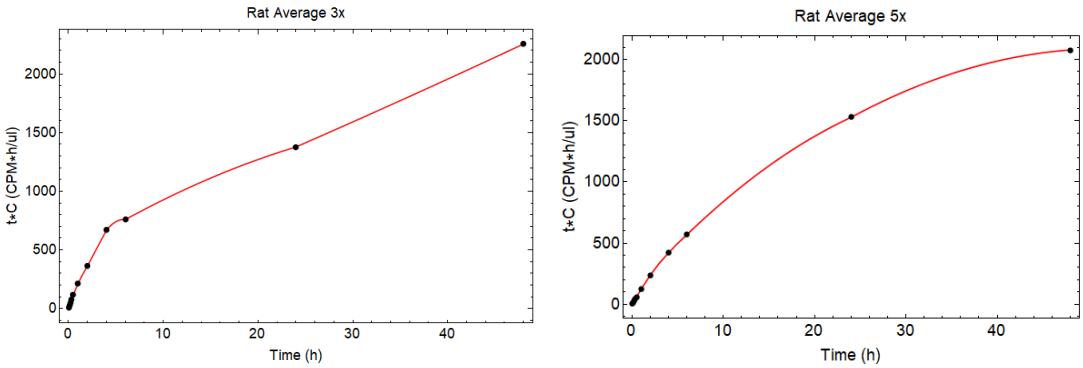

Figure 61. The first moment of the data; the plot of concentration*time vs. time. The data are fitted as shown by red solid line.

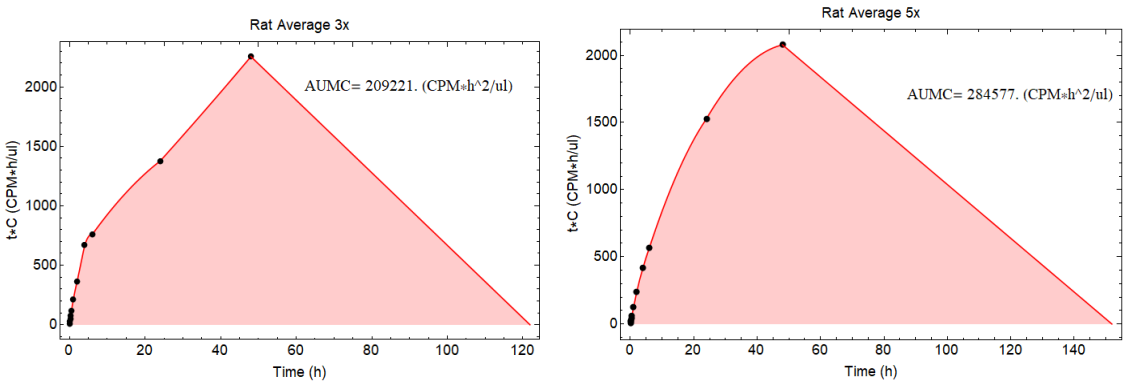

Figure 62. The AUMC extrapolated to infinity using λ. The pink area represents the total area under the curve ($AUMC_{0-\infty}$).

Table 9 summarizes the pharmacokinetic parameters calculated.

Table 9. Average pharmacokinetics parameters calculated for each group

PK Parameters	^{64}Cu@Au GNPs (3X)	^{64}Cu@Au GNPs (5X)
$AUC_{0-\infty}$ (CPM.h/µl)	5,351.6	5,334.9
$AUMC_{0-\infty}$ (CPM.h^2/µl)	209,221	284,577
Cmax (CPM/ µl)	324.2	204.8
MRT (h)	39.1	53.3
Cl (µl/h)	1,862.3	1,868.1
Vss (µl)	72,798.9	99,647.1
Kel' (1/h)	0.03	0.02

$t_{1/2}$ (h)	23.1	34.6

Based on the result provided above, the clearance rate of different concentrations of ^{64}Cu@Au GNPs are similar with a good approximation (~ 1.9 ml/h). The mean volume of distribution at steady state, Vss was higher with the higher concentration of the particles (~99.7 ml) than the 3X concentration (~72.8 ml). The half-life of ^{64}Cu@Au GNPs were also calculated to be ~23 and 35 h for 3X and 5X concentrations, respectively. As expected, the clearance rate of ^{64}Cu@Au GNPs is comparable to the one of 13 nm-sized PEG-coated GNPs [141], ^{64}Cu@CuS NPs [164], and solid lipid NPs [165].

CHAPTER XII

CONCLUSION OF PART TWO

To conclude the second part of this work, we developed and characterized non-radioactive Cu@Au GNPs confirmed by UV-vis spectrophotometer, TEM, TEM/EDS, XPS and ICP. Then we functionalized our hybrid GNPs were with varying amounts of cMBP to target c-Met receptor that is expressed on A549 human lung cancer cells. The result of 1 h and 4 h incubation with functionalized GNPs indicated that no uptake was taken place. In the next step, we radiolabeled the GNPs with ^{64}Cu to produce ^{64}Cu@Au GNPs. Targeting the cells with radiolabeled GNPs did not show any cell uptake either. The toxicity of Cu@Au GNPs in A549 cells was studies and the IC_{50} of our hybrid Cu@Au GNPs was found to be 807.2 ± 0.05 μg/ml. This result together with the result obtained from biodistribution studies in mice and pharmacokinetics studies in rats confirmed that Cu@Au GNPs have same physical and biological properties as that of similar sized traditional GNPs.

REFERENCES

[1] S. W. S. McKeever, *Thermoluminescence of solids* (no. Book, Whole). Cambridge [Cambridgeshire]; New York: Cambridge University Press, 1985.

[2] F. Placido, "THERMO-LUMINESCENCE TEST FOR FIRE-DAMAGED CONCRETE," *Magazine of Concrete Research,* vol. 32, no. 111, pp. 112-116, 1980.

[3] P. H. Benoit, D. W. G. Sears, and S. W. S. McKeever, "THE NATURAL THERMOLUMINESCENCE OF METEORITES .2. METEORITE ORBITS AND ORBITAL EVOLUTION," *Icarus,* vol. 94, no. 2, pp. 311-325, Dec 1991.

[4] C. L. Melcher, "THERMO-LUMINESCENCE OF METEORITES AND THEIR ORBITS," *Earth and Planetary Science Letters,* vol. 52, no. 1, pp. 39-54, 1981.

[5] D. W. G. Sears, "THERMO-LUMINESCENCE OF METEORITES - SHEDDING LIGHT ON THE COSMOS," *Nuclear Tracks and Radiation Measurements,* vol. 14, no. 1-2, pp. 5-17, 1988.

[6] J. Q. Spencer and D. C. W. Sanderson, "MAPPING THERMAL EXPOSURE BY LUMINESCENCE THERMOMETRY," (in English), *Radiat. Meas.,* Article vol. 23, no. 2-3, pp. 465-468, Apr-Jul 1994.

[7] R. Gunawidjaja, T. Myint, and H. Eilers, "Correlation of optical properties and temperature-induced irreversible phase transitions in europium-doped yttrium carbonate nanoparticles," *Journal of Solid State Chemistry,* vol. 184, no. 12, pp. 3280-3288, Dec 2011.

[8] R. Gunawidjaja, T. Myint, and H. Eilers, "Stabilization of tetragonal phase in ZrO2:Eu by rapid thermal heating," *Chemical Physics Letters,* vol. 515, no. 1-3, pp. 122-126, Oct 2011.

[9] T. Myint, R. Gunawidjaja, and H. Eilers, "Spectroscopic Properties of Nanophase Eu-Doped ZrO2 and Its Potential Application for Fast Temperature Sensing Under Extreme Conditions," *Journal of Physical Chemistry C,* vol. 116, no. 40, pp. 21629-21634, Oct 2012.

[10] T. Myint, R. Gunawidjaja, and H. Eilers, "Fast Pyroprobe-Heating-Induced Structural Changes of Y2O3:Eu Precursors and Their Optical Signatures," *Journal of Physical Chemistry C,* vol. 116, no. 2, pp. 1687-1693, Jan 2012.

[11] H. T. Sun, M. P. Yu, X. Sun, G. K. Wang, and J. Lian, "Effective Temperature Sensing by Irreversible Morphology Evolution of Ultrathin Gold Island Films," *Journal of Physical Chemistry C*, vol. 117, no. 7, pp. 3366-3373, Feb 2013.

[12] Y. Wang, N. Can, and P. D. Townsend, "Influence of Li dopants on thermoluminescence spectra of CaSO4 doped with Dy or Tm," (in English), *Journal of Luminescence*, Article vol. 131, no. 9, pp. 1864-1868, Sep 2011.

[13] B. A. Doull, L. C. Oliveira, D. Y. Wang, E. D. Milliken, and E. G. Yukihara, "Thermoluminescent properties of lithium borate, magnesium borate and calcium sulfate developed for temperature sensing," *Journal of Luminescence*, vol. 146, pp. 408-417, Feb 2014.

[14] M. L. Mah, P. R. Armstrong, S. S. Kim, J. R. Carney, J. M. Lightstone, and J. J. Talghader, "Sensing the Thermal History of High-Explosive Detonations Using Thermoluminescent Microparticles," *Ieee Sensors Journal*, vol. 13, no. 5, pp. 1742-1747, May 2013.

[15] M. L. Mah, M. E. Manfred, S. S. Kim, M. Prokic, E. G. Yukihara, and J. J. Talghader, "Measurement of Rapid Temperature Profiles Using Thermoluminescent Microparticles," *Ieee Sensors Journal*, vol. 10, no. 2, pp. 311-315, Feb 2010.

[16] E. G. Yukihara, A. C. Coleman, and B. A. Doull, "Passive temperature sensing using thermoluminescence: Laboratory tests using Li2B4O7:Cu,Ag, MgB4O7:Dy,Li and CaSO4:Ce,Tb," *Journal of Luminescence*, vol. 146, pp. 515-526, Feb 2014.

[17] B. A. Doull, L. C. Oliveira, and E. G. Yukihara, "Effect of annealing and fuel type on the thermoluminescent properties of Li2B4O7 Synthesized by Solution Combustion Synthesis," *Radiat. Meas.*, vol. 56, pp. 167-170, Sep 2013.

[18] E. G. Yukihara *et al.*, "Particle temperature measurements in closed chamber detonations using thermoluminescence from $Li_2B_4O_7$:Ag,Cu, MgB_4O_7:Dy,Li and $CaSO_4$:Ce,Tb," *J. Lumin.*, vol. 165, no. 0, pp. 145-152, 9// 2015.

[19] Yamashit.T, N. Nada, H. Onishi, and S. Kitamura, "CALCIUM SULFATE ACTIVATED BY THULIUM OR DYSPROSIUM FOR THERMOLUMINESCENCE DOSIMETRY," *Health Physics*, vol. 21, no. 2, pp. 295-+, 1971.

[20] C. E. May and J. A. Partridge, "THERMOLUMINESCENT KINETICS OF ALPHA-IRRADIATED ALKALI HALIDES," *Journal of Chemical Physics*, vol. 40, no. 5, pp. 1401-&, 1964 1964.

[21] C. Reuven and M. S. WS, *Theory of thermoluminescence and related phenomena*. World Scientific, 1997.

[22] P. W. Levy, "Recent developments in thermoluminescence kinetics," *Nuclear Tracks and Radiation Measurements (1982)*, vol. 10, no. 1-2, pp. 21-32, 1985.

[23] J. T. Randall and M. H. F. Wilkins, "Phosphorescence and electron traps-I. The study of trap distributions," *Proceedings of the Royal Society of London. Series A. Mathematical and Physical Sciences*, vol. 184, no. 999, pp. 365-389, 1945.

[24] J. T. Randall and M. H. F. Wilkins, "Phosphorescence and electron traps II. The interpretation of long-period phosphorescence," *Proceedings of the Royal Society of London. Series A. Mathematical and Physical Sciences,* vol. 184, no. 999, pp. 390-407, 1945.

[25] S. W. S. McKeever, M. Moscovitch, and P. D. Townsend, *Thermoluminescence dosimetry materials: properties and uses* (no. Book, Whole). Ashford, Kent, England: Nuclear Technology Pub, 1995.

[26] S. Das, A. A. Reddy, and G. V. Prakash, "Near white light emission from K+ ion compensated CaSO4:Dy3+,Eu3+ phosphors," *Ceramics International,* vol. 38, no. 7, pp. 5769-5773, Sep 2012.

[27] S. M. Dhopte, P. L. Muthal, V. K. Kondawar, and S. V. Moharil, "MECHANISM OF THERMOLUMINESCENCE IN CASO4-DY," *Radiation Effects and Defects in Solids,* vol. 117, no. 4, pp. 337-342, 1991.

[28] N. B. Ingle *et al.*, "Synthesis of CaSO4: Dy, CaSO4: Eu3+ and CaSO4: Eu2+ phosphors," *Radiat. Meas.,* vol. 43, no. 7, pp. 1191-1197, Aug 2008.

[29] R. L. Calvert and R. J. Danby, "THERMO-LUMINESCENCE AND RADIOPHOTOLUMINESCENCE FROM EU-DOPED AND SM-DOPED CASO4," *Physica Status Solidi a-Applied Research,* vol. 83, no. 2, pp. 597-604, 1984.

[30] M. T. Jose, U. Madhusoodanan, and A. R. Lakshmanan, "Influence of (group IIB) codopants on the thermostimulated luminescence sensitivity of CaSO4 : Dy/Tm," *Journal of Physics D-Applied Physics,* vol. 34, no. 5, pp. 717-721, Mar 2001.

[31] D. Lapraz, H. Prevost, P. Iacconi, C. Guigues, M. Benabdesselam, and D. Briand, "On the luminescence properties of CaSO4 : Ce," *Radiation Protection Dosimetry,* vol. 100, no. 1-4, pp. 365-368, 2002.

[32] A. M. Muke, P. L. Muthal, S. M. Dhopte, and S. V. Moharil, "Solid state metathesis of CaSO4:Eu2+ phosphor," *Journal of Luminescence,* vol. 132, no. 2, pp. 342-344, Feb 2012.

[33] K. S. V. Nambi, V. N. Bapat, and A. K. Ganguly, "THERMOLUMINESCENCE OF CASO4 DOPED WITH RARE-EARTHS," *Journal of Physics C-Solid State Physics,* vol. 7, no. 23, pp. 4403-4415, 1974.

[34] A. R. Lakshmanan, "A new high sensitive CaSO4 : Dy thermostimulated luminescence phosphor," *Physica Status Solidi a-Applied Research,* vol. 186, no. 1, pp. 153-166, Jul 2001.

[35] R. J. Matthews and T. G. Stoebe, "THERMOLUMINESCENT SPECTRA AND OPTICAL-ABSORPTION IN CASO4-DY," *Journal of Physics C-Solid State Physics,* vol. 15, no. 30, pp. 6271-6280, 1982.

[36] W. L. Medlin, "THERMOLUMINESCENCE IN ANHYDRITE," *Journal of Physics and Chemistry of Solids,* vol. 18, no. 2-3, pp. 238-252, 1961 1961.

[37] A. J. J. Bos, P. Dorenbos, A. Bessiere, and B. Viana, "Lanthanide energy levels in YPO4," *Radiat. Meas.,* vol. 43, no. 2-6, pp. 222-226, Feb-Jun 2008.

[38] S. Bastani, L. Oliveira, and E. Yukihara, "Development and characterization of lanthanide-doped CaSO4 for temperature sensing applications," *Optical Materials,* vol. 92, pp. 273-283, 2019.

[39] M. D. Morgan and T. G. Stoebe, "OPTICAL-ABSORPTION AND LUMINESCENT PROCESSES IN THERMOLUMINESCENT CASO4 DY," *Journal of Physics-Condensed Matter,* vol. 1, no. 33, pp. 5773-5781, Aug 1989.

[40] M. D. Morgan and T. G. Stoebe, "AN ELECTRON-SPIN RESONANCE STUDY OF THERMOLUMINESCENCE MECHANISMS IN CASO4-DY," *Journal of Physics-Condensed Matter,* vol. 2, no. 6, pp. 1619-1634, Feb 1990.

[41] A. Lewandowski and S. McKeever, "Generalized description of thermally stimulated processes without the quasiequilibrium approximation," *Physical Review B,* vol. 43, no. 10, p. 8163, 1991.

[42] S. W. S. McKeever, *Thermoluminescence of solids*. Cambridge [Cambridgeshire]

New York: Cambridge Cambridgeshire

New York : Cambridge University Press, 1985.

[43] V. R. Orante-Barrón *et al.,* "Luminescence properties of MgO produced by Solution Combustion Synthesis and doped with lanthanides and Li," *J. Lumin.,* vol. 131, pp. 1058-1065, 2011.

[44] W. Medlin, "The nature of traps and emission centers in thermoluminescent rock materials," *Thermoluminescence of geological materials,* pp. 193-223, 1968.

[45] V. R. Orante-Barron *et al.,* "Luminescence properties of MgO produced by solution combustion synthesis and doped with lanthanides and Li," *Journal of Luminescence,* vol. 131, no. 5, pp. 1058-1065, May 2011.

[46] E. Milliken, L. Oliveira, G. Denis, and E. Yukihara, "Testing a model-guided approach to the development of new thermoluminescent materials using YAG: Ln produced by solution combustion synthesis," *Journal of Luminescence,* vol. 132, no. 9, pp. 2495-2504, 2012.

[47] W. Chen, D. P. Cormode, Z. A. Fayad, and W. J. Mulder, "Nanoparticles as magnetic resonance imaging contrast agents for vascular and cardiac diseases," *Wiley Interdisciplinary Reviews: Nanomedicine and Nanobiotechnology,* vol. 3, no. 2, pp. 146-161, 2011.

[48] A. Jakhmola, N. Anton, and T. F. Vandamme, "Inorganic nanoparticles based contrast agents for X-ray computed tomography," *Advanced healthcare materials,* vol. 1, no. 4, pp. 413-431, 2012.

[49] J. B. Haun, N. K. Devaraj, S. A. Hilderbrand, H. Lee, and R. Weissleder, "Bioorthogonal chemistry amplifies nanoparticle binding and enhances the sensitivity of cell detection," *Nature nanotechnology,* vol. 5, no. 9, p. 660, 2010.

[50] A. Nasrolahi Shirazi, D. Mandal, R. K. Tiwari, L. Guo, W. Lu, and K. Parang, "Cyclic peptide-capped gold nanoparticles as drug delivery systems," *Molecular pharmaceutics,* vol. 10, no. 2, pp. 500-511, 2012.

[51] J. Song, J. Zhou, and H. Duan, "Self-assembled plasmonic vesicles of SERS-encoded amphiphilic gold nanoparticles for cancer cell targeting and traceable intracellular drug delivery," *Journal of the American Chemical Society,* vol. 134, no. 32, pp. 13458-13469, 2012.

[52] B. Jeremic, A. R. Aguerri, and N. Filipovic, "Radiosensitization by gold nanoparticles," *Clinical and Translational Oncology,* vol. 15, no. 8, pp. 593-601, 2013.

[53] H. Maeda, H. Nakamura, and J. Fang, "The EPR effect for macromolecular drug delivery to solid tumors: Improvement of tumor uptake, lowering of systemic toxicity, and distinct tumor imaging in vivo," *Advanced drug delivery reviews,* vol. 65, no. 1, pp. 71-79, 2013.

[54] H. B. Stone, C. N. Coleman, M. S. Anscher, and W. H. McBride, "Effects of radiation on normal tissue: consequences and mechanisms," *The lancet oncology,* vol. 4, no. 9, pp. 529-536, 2003.

[55] S. L. Liauw, P. P. Connell, and R. R. Weichselbaum, "New paradigms and future challenges in radiation oncology: an update of biological targets and technology," *Science translational medicine,* vol. 5, no. 173, pp. 173sr2-173sr2, 2013.

[56] I. Freestone, N. Meeks, M. Sax, and C. Higgitt, "The Lycurgus cup—a roman nanotechnology," *Gold bulletin,* vol. 40, no. 4, pp. 270-277, 2007.

[57] M.-C. Daniel and D. Astruc, "Gold nanoparticles: assembly, supramolecular chemistry, quantum-size-related properties, and applications toward biology, catalysis, and nanotechnology," *Chemical reviews,* vol. 104, no. 1, pp. 293-346, 2004.

[58] M. Faraday, "X. The Bakerian Lecture.—Experimental relations of gold (and other metals) to light," *Philosophical Transactions of the Royal Society of London,* no. 147, pp. 145-181, 1857.

[59] L. Fass, "Imaging and cancer: a review," *Molecular oncology,* vol. 2, no. 2, pp. 115-152, 2008.

[60] W. Cai, T. Gao, H. Hong, and J. Sun, "Applications of gold nanoparticles in cancer nanotechnology," *Nanotechnology, science and applications,* vol. 1, p. 17, 2008.

[61] F. F. A. C. Silva, "Gallium compounds forthe design of (nano) radiophamarceuticals," 2014.

[62] T. K. Sau, A. L. Rogach, F. Jäckel, T. A. Klar, and J. Feldmann, "Properties and applications of colloidal nonspherical noble metal nanoparticles," *Advanced Materials,* vol. 22, no. 16, pp. 1805-1825, 2010.

[63] F. Dumur, A. Guerlin, E. Dumas, D. Bertin, D. Gigmes, and C. R. Mayer, "Controlled spontaneous generation of gold nanoparticles assisted by dual reducing and capping agents," *Gold bulletin*, vol. 44, no. 2, pp. 119-137, 2011.

[64] P. S. Ghosh, C.-K. Kim, G. Han, N. S. Forbes, and V. M. Rotello, "Efficient gene delivery vectors by tuning the surface charge density of amino acid-functionalized gold nanoparticles," *ACS nano*, vol. 2, no. 11, pp. 2213-2218, 2008.

[65] Z. Wang, R. Lévy, D. G. Fernig, and M. Brust, "The peptide route to multifunctional gold nanoparticles," *Bioconjugate chemistry*, vol. 16, no. 3, pp. 497-500, 2005.

[66] C. P. Shaw, D. A. Middleton, M. Volk, and R. Lévy, "Amyloid-derived peptide forms self-assembled monolayers on gold nanoparticle with a curvature-dependent β-sheet structure," *ACS nano*, vol. 6, no. 2, pp. 1416-1426, 2012.

[67] Z. e. Krpetić, S. Saleemi, I. A. Prior, V. Sée, R. Qureshi, and M. Brust, "Negotiation of intracellular membrane barriers by TAT-modified gold nanoparticles," *ACS nano*, vol. 5, no. 6, pp. 5195-5201, 2011.

[68] T. Liu and B. Thierry, "A solution to the PEG dilemma: efficient bioconjugation of large gold nanoparticles for biodiagnostic applications using mixed layers," *Langmuir*, vol. 28, no. 44, pp. 15634-15642, 2012.

[69] N. B. Shah, G. M. Vercellotti, J. G. White, A. Fegan, C. R. Wagner, and J. C. Bischof, "Blood–nanoparticle interactions and in vivo biodistribution: impact of surface PEG and ligand properties," *Molecular pharmaceutics*, vol. 9, no. 8, pp. 2146-2155, 2012.

[70] J. Zhu, C. Waengler, R. B. Lennox, and R. Schirrmacher, "Preparation of water-soluble maleimide-functionalized 3 nm gold nanoparticles: a new bioconjugation template," *Langmuir*, vol. 28, no. 13, pp. 5508-5512, 2012.

[71] J. Gao, X. Huang, H. Liu, F. Zan, and J. Ren, "Colloidal stability of gold nanoparticles modified with thiol compounds: bioconjugation and application in cancer cell imaging," *Langmuir*, vol. 28, no. 9, pp. 4464-4471, 2012.

[72] D.-H. Tsai *et al.*, "Adsorption and conformation of serum albumin protein on gold nanoparticles investigated using dimensional measurements and in situ spectroscopic methods," *Langmuir*, vol. 27, no. 6, pp. 2464-2477, 2011.

[73] A. M. Reed and S. J. Metallo, "Oriented protein adsorption to gold nanoparticles through a genetically encodable binding motif," *Langmuir*, vol. 26, no. 24, pp. 18945-18950, 2010.

[74] I. Lee, H. Kwon, and D. Kim, "Colorimetric determination of copper (II) using a polyamine-functionalized gold nanoparticle probe," *Angew. Chem. Int. Ed*, vol. 124, pp. 8930-8935, 2012.

[75] J. Turkevich, P. C. Stevenson, and J. Hillier, "A study of the nucleation and growth processes in the synthesis of colloidal gold," *Discussions of the Faraday Society*, vol. 11, pp. 55-75, 1951.

[76] J. Turkevich, P. C. Stevenson, and J. Hillier, "The formation of colloidal gold," *The Journal of Physical Chemistry,* vol. 57, no. 7, pp. 670-673, 1953.

[77] G. Frens, "Controlled nucleation for the regulation of the particle size in monodisperse gold suspensions," *Nature physical science,* vol. 241, no. 105, p. 20, 1973.

[78] R. D. Ross and R. K. Roeder, "Binding affinity of surface functionalized gold nanoparticles to hydroxyapatite," *Journal of Biomedical Materials Research Part A,* vol. 99, no. 1, pp. 58-66, 2011.

[79] M. Brust, M. Walker, D. Bethell, D. J. Schiffrin, and R. Whyman, "Synthesis of thiol-derivatised gold nanoparticles in a two-phase liquid–liquid system," *Journal of the Chemical Society, Chemical Communications,* no. 7, pp. 801-802, 1994.

[80] A. G. Kanaras, F. S. Kamounah, K. Schaumburg, C. J. Kiely, and M. Brust, "Thioalkylated tetraethylene glycol: a new ligand for water soluble monolayer protected gold clusters," *Chemical communications,* no. 20, pp. 2294-2295, 2002.

[81] G. Scarì *et al.*, "Gold nanoparticles capped by a GC-containing peptide functionalized with an RGD motif for integrin targeting," *Bioconjugate chemistry,* vol. 23, no. 3, pp. 340-349, 2012.

[82] M. Colombo *et al.*, "Protein-Assisted One-Pot Synthesis and Biofunctionalization of Spherical Gold Nanoparticles for Selective Targeting of Cancer Cells," *Angewandte Chemie International Edition,* vol. 51, no. 37, pp. 9272-9275, 2012.

[83] A. S. Goustin, E. B. Leof, G. D. Shipley, and H. L. Moses, "Growth factors and cancer," *Cancer research,* vol. 46, no. 3, pp. 1015-1029, 1986.

[84] L. Cui, S. Her, G. R. Borst, R. G. Bristow, D. A. Jaffray, and C. Allen, "Radiosensitization by gold nanoparticles: will they ever make it to the clinic?," *Radiotherapy and Oncology,* vol. 124, no. 3, pp. 344-356, 2017.

[85] M. Fani and H. R. Maecke, "Radiopharmaceutical development of radiolabelled peptides," *European journal of nuclear medicine and molecular imaging,* vol. 39, no. 1, pp. 11-30, 2012.

[86] R. A. Dumont *et al.*, "Targeted radiotherapy of prostate cancer with a gastrin-releasing peptide receptor antagonist is effective as monotherapy and in combination with rapamycin," *Journal of nuclear medicine,* vol. 54, no. 5, pp. 762-769, 2013.

[87] T. Win *et al.*, "Areas of normal pulmonary parenchyma on HRCT exhibit increased FDG PET signal in IPF patients," *European journal of nuclear medicine and molecular imaging,* vol. 41, no. 2, pp. 337-342, 2014.

[88] G. B. Saha and G. B. Saha, *Fundamentals of nuclear pharmacy*. Springer, 2004.

[89] S. Juergens, W. A. Herrmann, and F. E. Kuehn, "Rhenium and technetium based radiopharmaceuticals: Development and recent advances," *Journal of Organometallic Chemistry,* vol. 751, pp. 83-89, 2014.

[90] G. R. Morais, A. Paulo, and I. Santos, "Organometallic complexes for SPECT imaging and/or radionuclide therapy," *Organometallics*, vol. 31, no. 16, pp. 5693-5714, 2012.

[91] J. S. Welsh, "Beta radiation," *The oncologist*, vol. 11, no. 2, pp. 181-183, 2006.

[92] J. T. Bushberg, *The essential physics of medical imaging*, 3rd ed.. ed. Philadelphia: Philadelphia : Wolters Kluwer Health/Lippincott Williams & Wilkins, 2012.

[93] C. L. Ferreira *et al.*, "Evaluation of novel bifunctional chelates for the development of Cu-64-based radiopharmaceuticals," *Nuclear medicine and biology*, vol. 35, no. 8, pp. 875-882, 2008.

[94] K. C. L. Black, W. J. Akers, G. Sudlow, B. G. Xu, R. Laforest, and S. Achilefu, "Dual-radiolabeled nanoparticle SPECT probes for bioimaging," (in English), *Nanoscale*, vol. 7, no. 2, pp. 440-444, 2015.

[95] P. M. Peiris *et al.*, "Vascular Targeting of a Gold Nanoparticle to Breast Cancer Metastasis," (in English), *J Pharm Sci-Us*, vol. 104, no. 8, pp. 2600-2610, Aug 2015.

[96] S. Goel, F. Chen, E. B. Ehlerding, and W. B. Cai, "Intrinsically Radiolabeled Nanoparticles: An Emerging Paradigm," (in English), *Small*, vol. 10, no. 19, pp. 3825-3830, Oct 15 2014.

[97] J. Llop *et al.*, "Visualisation of dual radiolabelled poly(lactide-co-glycolide) nanoparticle degradation in vivo using energy-discriminant SPECT," (in English), *J Mater Chem B*, vol. 3, no. 30, pp. 6293-6300, 2015.

[98] D. W. Grainger and D. G. Castner, "Nanobiomaterials and nanoanalysis: opportunities for improving the science to benefit biomedical technologies," *Advanced Materials*, vol. 20, no. 5, pp. 867-877, 2008.

[99] A. P. Alivisatos, "Semiconductor clusters, nanocrystals, and quantum dots," *science*, vol. 271, no. 5251, pp. 933-937, 1996.

[100] V. V. Mody, R. Siwale, A. Singh, and H. R. Mody, "Introduction to metallic nanoparticles," *Journal of Pharmacy and Bioallied Sciences*, vol. 2, no. 4, p. 282, 2010.

[101] A. H. Faraji and P. Wipf, "Nanoparticles in cellular drug delivery," *Bioorganic & medicinal chemistry*, vol. 17, no. 8, pp. 2950-2962, 2009.

[102] F. Re, R. Moresco, and M. Masserini, "Nanoparticles for neuroimaging," *Journal of Physics D: Applied Physics*, vol. 45, no. 7, p. 073001, 2012.

[103] P. Boisseau and B. Loubaton, "Nanomedicine, nanotechnology in medicine," *Comptes Rendus Physique*, vol. 12, no. 7, pp. 620-636, 2011.

[104] H. Boulaiz *et al.*, "Nanomedicine: application areas and development prospects," *International journal of molecular sciences*, vol. 12, no. 5, pp. 3303-3321, 2011.

[105] S. Sahoo, S. Parveen, and J. Panda, "The present and future of nanotechnology in human health care," *Nanomedicine: Nanotechnology, Biology and Medicine,* vol. 3, no. 1, pp. 20-31, 2007.

[106] S. K. Sahoo, R. Misra, and S. Parveen, "Nanoparticles: a boon to drug delivery, therapeutics, diagnostics and imaging," in *Nanomedicine in Cancer*: Pan Stanford, 2017, pp. 73-124.

[107] E. Morales-Avila, G. Ferro-Flores, B. E. Ocampo-García, and F. de María Ramírez, "Radiolabeled nanoparticles for molecular imaging," in *Molecular imaging*: IntechOpen, 2012.

[108] N. K. Devaraj, E. J. Keliher, G. M. Thurber, M. Nahrendorf, and R. Weissleder, "18F labeled nanoparticles for in vivo PET-CT imaging," *Bioconjugate chemistry,* vol. 20, no. 2, pp. 397-401, 2009.

[109] F. Ducongé *et al.*, "Fluorine-18-labeled phospholipid quantum dot micelles for in vivo multimodal imaging from whole body to cellular scales," *Bioconjugate chemistry,* vol. 19, no. 9, pp. 1921-1926, 2008.

[110] W. Cai, K. Chen, Z.-B. Li, S. S. Gambhir, and X. Chen, "Dual-function probe for PET and near-infrared fluorescence imaging of tumor vasculature," *Journal of Nuclear Medicine,* vol. 48, no. 11, pp. 1862-1870, 2007.

[111] K. Chen, Z.-B. Li, H. Wang, W. Cai, and X. Chen, "Dual-modality optical and positron emission tomography imaging of vascular endothelial growth factor receptor on tumor vasculature using quantum dots," *European journal of nuclear medicine and molecular imaging,* vol. 35, no. 12, pp. 2235-2244, 2008.

[112] M. R. McDevitt *et al.*, "Tumor targeting with antibody-functionalized, radiolabeled carbon nanotubes," *Journal of Nuclear Medicine,* vol. 48, no. 7, pp. 1180-1189, 2007.

[113] S. Bamrungsap *et al.*, "Nanotechnology in therapeutics: a focus on nanoparticles as a drug delivery system," *Nanomedicine,* vol. 7, no. 8, pp. 1253-1271, 2012.

[114] P. Ghosh, G. Han, M. De, C. K. Kim, and V. M. Rotello, "Gold nanoparticles in delivery applications," *Advanced drug delivery reviews,* vol. 60, no. 11, pp. 1307-1315, 2008.

[115] J. F. Hainfeld, H. M. Smilowitz, M. J. O'connor, F. A. Dilmanian, and D. N. Slatkin, "Gold nanoparticle imaging and radiotherapy of brain tumors in mice," *Nanomedicine,* vol. 8, no. 10, pp. 1601-1609, 2013.

[116] C. Loo, A. Lowery, N. Halas, J. West, and R. Drezek, "Immunotargeted nanoshells for integrated cancer imaging and therapy," *Nano letters,* vol. 5, no. 4, pp. 709-711, 2005.

[117] X. Huang, P. K. Jain, I. H. El-Sayed, and M. A. El-Sayed, "Determination of the minimum temperature required for selective photothermal destruction of cancer cells with the use of immunotargeted gold nanoparticles," *Photochemistry and photobiology,* vol. 82, no. 2, pp. 412-417, 2006.

[118] S. H. Cho and S. Krishnan, *Cancer nanotechnology: principles and applications in radiation oncology*. CRC press, 2013.

[119] S. J. McMahon *et al.*, "Energy dependence of gold nanoparticle radiosensitization in plasmid DNA," *The Journal of Physical Chemistry C,* vol. 115, no. 41, pp. 20160-20167, 2011.

[120] K. T. Butterworth, S. J. McMahon, F. J. Currell, and K. M. Prise, "Physical basis and biological mechanisms of gold nanoparticle radiosensitization," *Nanoscale,* vol. 4, no. 16, pp. 4830-4838, 2012.

[121] J.-P. Pignol and E. Lechtman, "Reply to Comment on 'Implications on clinical scenario of gold nanoparticle radiosensitization in regards to photon energy, nanoparticle size, concentration and location'," *Physics in Medicine & Biology,* vol. 57, no. 1, p. 291, 2011.

[122] S. H. Cho, "Estimation of tumour dose enhancement due to gold nanoparticles during typical radiation treatments: a preliminary Monte Carlo study," *Physics in Medicine & Biology,* vol. 50, no. 15, p. N163, 2005.

[123] T. Wolfe *et al.*, "Targeted gold nanoparticles enhance sensitization of prostate tumors to megavoltage radiation therapy in vivo," *Nanomedicine: Nanotechnology, Biology and Medicine,* vol. 11, no. 5, pp. 1277-1283, 2015.

[124] F. J. Reynoso, N. Manohar, S. Krishnan, and S. H. Cho, "Design of an Yb-169 source optimized for gold nanoparticle-aided radiation therapy," *Medical physics,* vol. 41, no. 10, 2014.

[125] J.-K. Kim *et al.*, "Therapeutic application of metallic nanoparticles combined with particle-induced x-ray emission effect," *Nanotechnology,* vol. 21, no. 42, p. 425102, 2010.

[126] R. K. Visaria *et al.*, "Enhancement of tumor thermal therapy using gold nanoparticle–assisted tumor necrosis factor-α delivery," *Molecular cancer therapeutics,* vol. 5, no. 4, pp. 1014-1020, 2006.

[127] F. Wang, Y.-C. Wang, S. Dou, M.-H. Xiong, T.-M. Sun, and J. Wang, "Doxorubicin-tethered responsive gold nanoparticles facilitate intracellular drug delivery for overcoming multidrug resistance in cancer cells," *ACS nano,* vol. 5, no. 5, pp. 3679-3692, 2011.

[128] A. Albanese, P. S. Tang, and W. C. Chan, "The effect of nanoparticle size, shape, and surface chemistry on biological systems," *Annual review of biomedical engineering,* vol. 14, pp. 1-16, 2012.

[129] G. Ting, C.-H. Chang, H.-E. Wang, and T.-W. Lee, "Nanotargeted radionuclides for cancer nuclear imaging and internal radiotherapy," *BioMed Research International,* vol. 2010, 2010.

[130] J. Thariat, J.-M. Hannoun-Levi, A. S. Myint, T. Vuong, and J.-P. Gérard, "Past, present, and future of radiotherapy for the benefit of patients," *Nature reviews Clinical oncology,* vol. 10, no. 1, p. 52, 2013.

[131] G. Delaney, S. Jacob, C. Featherstone, and M. Barton, "The role of radiotherapy in cancer treatment: estimating optimal utilization from a review of evidence-based clinical guidelines," *Cancer: Interdisciplinary International Journal of the American Cancer Society,* vol. 104, no. 6, pp. 1129-1137, 2005.

[132] G. G. Steel and M. J. Peckham, "Exploitable mechanisms in combined radiotherapy-chemotherapy: the concept of additivity," *International Journal of Radiation Oncology* Biology* Physics,* vol. 5, no. 1, pp. 85-91, 1979.

[133] P. Wardman, "Chemical radiosensitizers for use in radiotherapy," *Clinical oncology,* vol. 19, no. 6, pp. 397-417, 2007.

[134] I. D. M. Herold, CC Stobbe, RV Iyer, JD Chapman, D, "Gold microspheres: a selective technique for producing biologically effective dose enhancement," *International journal of radiation biology,* vol. 76, no. 10, pp. 1357-1364, 2000.

[135] S. Rosa, C. Connolly, G. Schettino, K. T. Butterworth, and K. M. Prise, "Biological mechanisms of gold nanoparticle radiosensitization," *Cancer nanotechnology,* vol. 8, no. 1, p. 2, 2017.

[136] V. L. Colvin, "The potential environmental impact of engineered nanomaterials," *Nature biotechnology,* vol. 21, no. 10, p. 1166, 2003.

[137] R. Shukla, V. Bansal, M. Chaudhary, A. Basu, R. R. Bhonde, and M. Sastry, "Biocompatibility of gold nanoparticles and their endocytotic fate inside the cellular compartment: a microscopic overview," *Langmuir,* vol. 21, no. 23, pp. 10644-10654, 2005.

[138] C. J. Murphy *et al.*, "Gold nanoparticles in biology: beyond toxicity to cellular imaging," *Accounts of chemical research,* vol. 41, no. 12, pp. 1721-1730, 2008.

[139] E. Boisselier and D. Astruc, "Gold nanoparticles in nanomedicine: preparations, imaging, diagnostics, therapies and toxicity," *Chemical society reviews,* vol. 38, no. 6, pp. 1759-1782, 2009.

[140] Y. Pan *et al.*, "Size-dependent cytotoxicity of gold nanoparticles," *Small,* vol. 3, no. 11, pp. 1941-1949, 2007.

[141] W.-S. Cho *et al.*, "Acute toxicity and pharmacokinetics of 13 nm-sized PEG-coated gold nanoparticles," *Toxicology and applied pharmacology,* vol. 236, no. 1, pp. 16-24, 2009.

[142] T. Mironava, M. Hadjiargyrou, M. Simon, V. Jurukovski, and M. H. Rafailovich, "Gold nanoparticles cellular toxicity and recovery: effect of size, concentration and exposure time," *Nanotoxicology,* vol. 4, no. 1, pp. 120-137, 2010.

[143] X.-D. Zhang *et al.*, "Size-dependent in vivo toxicity of PEG-coated gold nanoparticles," *International journal of nanomedicine,* vol. 6, p. 2071, 2011.

[144] T. S. Hauck, A. A. Ghazani, and W. C. Chan, "Assessing the effect of surface chemistry on gold nanorod uptake, toxicity, and gene expression in mammalian cells," *Small,* vol. 4, no. 1, pp. 153-159, 2008.

[145] D. Andes and W. Craig, "Animal model pharmacokinetics and pharmacodynamics: a critical review," *International journal of antimicrobial agents,* vol. 19, no. 4, pp. 261-268, 2002.

[146] J. Zhang, X. Xu, C. Yang, F. Yang, and X. Yang, "Colorimetric iodide recognition and sensing by citrate-stabilized core/shell Cu@ Au nanoparticles," *Analytical chemistry,* vol. 83, no. 10, pp. 3911-3917, 2011.

[147] J. G. Christensen, J. Burrows, and R. Salgia, "c-Met as a target for human cancer and characterization of inhibitors for therapeutic intervention," *Cancer letters,* vol. 225, no. 1, pp. 1-26, 2005.

[148] C. Birchmeier, W. Birchmeier, E. Gherardi, and G. F. V. Woude, "Met, metastasis, motility and more," *Nature reviews Molecular cell biology,* vol. 4, no. 12, p. 915, 2003.

[149] G. Maulik, A. Shrikhande, T. Kijima, P. C. Ma, P. T. Morrison, and R. Salgia, "Role of the hepatocyte growth factor receptor, c-Met, in oncogenesis and potential for therapeutic inhibition," *Cytokine & growth factor reviews,* vol. 13, no. 1, pp. 41-59, 2002.

[150] Y. Yang *et al.*, "A selective small molecule inhibitor of c-Met, PHA-665752, reverses lung premalignancy induced by mutant K-ras," *Molecular cancer therapeutics,* vol. 7, no. 4, pp. 952-960, 2008.

[151] K. Kim *et al.*, "A neutralizable epitope is induced on HGF upon its interaction with its receptor cMet," *Biochemical and biophysical research communications,* vol. 354, no. 1, pp. 115-121, 2007.

[152] H. Gali, "An open-source automated peptide synthesizer based on Arduino and Python," *SLAS TECHNOLOGY: Translating Life Sciences Innovation,* vol. 22, no. 5, pp. 493-499, 2017.

[153] J. Eccles, U. Bangert, M. Bromfield, P. Christian, A. Harvey, and P. Thomas, "UV-Vis plasmon studies of metal nanoparticles," in *Journal of Physics: Conference Series*, 2010, vol. 241, no. 1: IOP Publishing, p. 012090.

[154] A. Chu, J. Cook, R. J. Heesom, J. L. Hutchison, M. L. Green, and J. Sloan, "Filling of carbon nanotubes with silver, gold, and gold chloride," *Chemistry of Materials,* vol. 8, no. 12, pp. 2751-2754, 1996.

[155] K. Rokosz *et al.*, "SEM, EDS and XPS analysis of the coatings obtained on titanium after plasma electrolytic oxidation in electrolytes containing copper nitrate," *Materials,* vol. 9, no. 5, p. 318, 2016.

[156] B. G. Bravo, S. L. Michelhaugh, M. P. Soriaga, I. Villegas, D. W. Suggs, and J. L. Stickney, "Anodic underpotential deposition and cathodic stripping of iodine at polycrystalline and single-crystal gold: studies by LEED, AES, XPS, and electrochemistry," *The Journal of Physical Chemistry,* vol. 95, no. 13, pp. 5245-5249, 1991.

[157] M. Tominaga, Y. Taema, and I. Taniguchi, "Electrocatalytic glucose oxidation at bimetallic gold–copper nanoparticle-modified carbon electrodes in alkaline solution," *Journal of Electroanalytical Chemistry,* vol. 624, no. 1-2, pp. 1-8, 2008.

[158] M. Stewart and I. Watson, "Standard units for expressing drug concentrations in biological fluids," *British journal of clinical pharmacology,* vol. 16, no. 1, p. 3, 1983.

[159] R. Chakravarty *et al.*, "Industrial-scale synthesis of intrinsically radiolabeled 64cus nanoparticles for use in positron emission tomography (pet) imaging of cancer," *Industrial & Engineering Chemistry Research,* vol. 55, no. 48, pp. 12407-12419, 2016.

[160] S. Vijayakumar and S. Ganesan, "Gold nanoparticles as an HIV entry inhibitor," *Current HIV research,* vol. 10, no. 8, pp. 643-646, 2012.

[161] D. Mateo, P. Morales, A. Ávalos, and A. I. Haza, "Comparative cytotoxicity evaluation of different size gold nanoparticles in human dermal fibroblasts," *Journal of Experimental Nanoscience,* vol. 10, no. 18, pp. 1401-1417, 2015.

[162] T. M. Jones-Wilson *et al.*, "The in vivo behavior of copper-64-labeled azamacrocyclic complexes," *Nuclear medicine and biology,* vol. 25, no. 6, pp. 523-530, 1998.

[163] C. J. Anderson *et al.*, "Preparation, biodistribution and dosimetry of copper-64-labeled anti-colorectal carcinoma monoclonal antibody fragments 1A3-F (ab′) 2," *Journal of nuclear medicine,* vol. 36, no. 5, pp. 850-858, 1995.

[164] M. Zhou *et al.*, "A chelator-free multifunctional [64Cu] CuS nanoparticle platform for simultaneous micro-PET/CT imaging and photothermal ablation therapy," *Journal of the American Chemical Society,* vol. 132, no. 43, pp. 15351-15358, 2010.

[165] H. Dang *et al.*, "Luteolin-loaded solid lipid nanoparticles synthesis, characterization, & improvement of bioavailability, pharmacokinetics in vitro and vivo studies," *Journal of Nanoparticle Research,* vol. 16, no. 4, p. 2347, 2014.

VITA

Solmaz Bastani

Candidate for the Degree of

Doctor of Philosophy

Dissertation: DEVELOPMENT OF LANTHANIDE-DOPED $CaSO_4$ FOR TEMPERATURE SENSING APPLICATIONS & ^{64}Cu-DOPED GOLD NANOPARTICLES FOR RADIOSENSITIZATION

Major Field: Physics

Biographical:

Education:

Completed the requirements for the Doctor of Philosophy in Physics at Oklahoma State University, Stillwater, Oklahoma in July 2019.

Completed the requirements for the Master of Science in Atomic & Molecular Physics at Iran University of Science and Technology, Tehran, Iran in 2009.

Completed the requirements for the Bachelor of Science in Physics at Shahid Beheshti University, Tehran, Iran in 2006.

Experience:
- Material development and characterization, semi-conductor synthesis, Thermoluminescence, temperature sensing, radiation dosimetry techniques, gold nanoparticles synthesis and functionalization, radiolabeling, cell culture, in vivo and in vitro studies, molecular imaging.
- Scientific project management and conducting research.
- Teaching and mentoring students in Physics lectures, labs and research projects.
- Leadership and teamwork background in government organizations.

Professional Memberships: American Association of Physicists in Medicine (AAPM), American Association of Physics Teachers (AAPT), National Association of Graduate-Professional Students (NAGPS).